

NONCOHERENT DIFFERENTIAL DEMODULATION OF CPM SIGNALS WITH
JOINT FREQUENCY OFFSET AND SYMBOL TIMING ESTIMATION

A THESIS SUBMITTED TO
THE GRADUATE SCHOOL OF NATURAL AND APPLIED SCIENCES
OF
MIDDLE EAST TECHNICAL UNIVERSITY

BY

ONUR ÇULHA

IN PARTIAL FULFILLMENT OF THE REQUIREMENTS
FOR
THE DEGREE OF MASTER OF SCIENCE
IN
ELECTRICAL AND ELECTRONICS ENGINEERING

SEPTEMBER 2011

Approval of the thesis:

**NONCOHERENT DIFFERENTIAL DEMODULATION OF CPM SIGNALS WITH
JOINT FREQUENCY OFFSET AND SYMBOL TIMING ESTIMATION**

submitted by **ONUR ÇULHA** in partial fulfillment of the requirements for the degree of **Master of Science in Electrical and Electronics Engineering Department, Middle East Technical University** by,

Prof. Dr. Canan Özgen
Dean, Graduate School of **Natural and Applied Sciences** _____

Prof. Dr. İsmet Erkmek
Head of Department, **Electrical and Electronics Engineering** _____

Prof. Dr. Yalçın Tanık
Supervisor, **Electrical and Electronics Engineering Dept., METU** _____

Examining Committee Members

Prof. Dr. Mete Severcan
Electrical and Electronics Engineering Dept., METU _____

Prof. Dr. Yalçın Tanık
Electrical and Electronics Engineering Dept., METU _____

Assoc. Prof. Dr. Melek Diker Yücel
Electrical and Electronics Engineering Dept., METU _____

Assoc. Prof. Dr. A. Özgür Yılmaz
Electrical and Electronics Engineering Dept., METU _____

Güzin Kurnaz, PhD
ASELSAN HC _____

Date: 16.09.2011

I hereby declare that all information in this document has been obtained and presented in accordance with academic rules and ethical conduct. I also declare that, as required by these rules and conduct, I have fully cited and referenced all material and results that are not original to this work.

Name, Last name: Onur ÇULHA

Signature :

ABSTRACT

NONCOHERENT DIFFERENTIAL DEMODULATION OF CPM SIGNALS WITH JOINT FREQUENCY OFFSET AND SYMBOL TIMING ESTIMATION

Çulha, Onur

M.Sc., Department of Electrical and Electronics Engineering

Supervisor: Prof. Dr. Yalçın Tanık

September 2011, 115 Pages

In this thesis, noncoherent differential demodulation of CPM signals with joint carrier frequency offset and symbol timing estimation is investigated. CPM is very attractive for wireless communications owing to major properties: good spectral efficiency and a constant envelope property. In order to demodulate the received CPM signal differentially, the symbol timing and the carrier frequency offset have to be estimated accurately. There are numerous methods developed for the purpose. However, we have not encountered studies (which are based on auto-correlation estimation and hence suitable for blind synchronization) that give expectable performance for both M -ary and partial response signaling. Thus, in this thesis we analyze a feedforward blind estimation scheme, which recovers the symbol timing and the frequency offset of M -ary CPM signals and partial response CPM signals. In addition, we surveyed low complexity symbol detection methods for CPM signals. Reduced state Viterbi differential detector incorporated to the joint frequency offset and symbol timing estimator is also examined. The performance of the examined demodulator scheme is assessed for the AWGN channel by computer simulations.

Keywords: Frequency Estimation, Symbol Timing Estimation, Differential Demodulation, Continuous Phase Modulation, Reduced State Viterbi Detection

ÖZ

CPM SİNYALLERİNİN FREKANS KAYMASI VE SEMBOL ZAMANI KESTİRİMİ İLE EVRE-UYUMSUZ DEMODÜLASYONU

Çulha, Onur

Yüksek Lisans., Elektrik ve Elektronik Mühendisliği Bölümü

Tez Yöneticisi: Prof. Dr. Yalçın Tanık

Eylül 2011,115 Sayfa

Bu tez çalışmasında, CPM sinyallerinin frekans kayması ve sembol zamanı kestirimi ile evreyumsuz demodülasyonu incelenmiştir. CPM iki önemli özelliğinden dolayı kablosuz haberleşme için caziptir: iyi spektral verimlilik ve sabit zarfa sahip olma. Alınan CPM sinyalini diferansiyel olarak demodüle etmek için önce taşıyıcı frekansı ve sembol zamanı kestirilmelidir. Bu amaç için geliştirilmiş çok sayıda metod mevcuttur. Ancak, M'li ve kısmi yanıt sinyallerinin her ikisi için beklenen sonuçlar veren (özilinti kestirimine dayanan ve kör eşzamanlama için uygun) çalışmalarla karşılaşmadık. Bu nedenle, bu tez çalışmasında M'li CPM sinyalleri ve kısmi yanıt sinyalleri için ileri-beslemeli kör bir kestirim yöntemi analiz edilmektedir. Ayrıca, CPM sinyalleri için düşük karmaşıklıkta sembol tespit yöntemleri incelenmiştir. Birlikte frekans kayması ve sembol zamanı kestirimcisi ile bütünleşik azaltılmış durumlu Viterbi diferansiyel sembol tespit edici incelenmiştir. İncelenen demodulator yapısının AWGN kanalı için performansı bilgisayar benzetimleri ile değerlendirilmiştir.

Anahtar Kelimeler: Frekans Kestirimi, Sembol Zamanı Kestirimi, Diferansiyel Demodülatör, Sürekli Faz Kiplenimi, Azaltılmış Durumlu Viterbi Tespiti

To my love,

ACKNOWLEDGMENTS

I am most thankful to my supervisor Prof. Dr. Yalçın Tanık for sharing his invaluable ideas and experiences on the subject of my thesis.

I am very grateful to TÜBİTAK-SAGE throughout the production of my thesis.

I would like to forward my appreciation to my friends and colleagues especially, Çağdaş EVCİMEN and Hüseyin Caner BECER who contributed to my thesis with their continuous encouragement.

Special thanks to my wife for all her help and showing great patience during the writing process of my thesis. I have always felt her endless support with me.

TABLE OF CONTENTS

ABSTRACT	iv
ÖZ	v
ACKNOWLEDGMENTS	vii
TABLE OF CONTENTS.....	viii
LIST OF TABLES	xi
LIST OF FIGURES.....	xii
LIST OF ABBREVIATIONS	xvi
CHAPTERS	
1 INTRODUCTION.....	1
1.1 Motivation	1
1.2 Organization of the Thesis	3
2 Background information.....	5
2.1 CPFSK.....	5
2.2 Continuous Phase Modulation (CPM)	9
2.2.1 Phase Tree and Trellis Diagram	11
2.2.2 Power Spectral Density (PSD) of MSK	15
3 JOINT CARRIER FREQUENCY OFFSET AND SYMBOL TIME ESTIMATION	17
3.1 Literature survey	18

3.1.1	Carrier Frequency Offset (CFO) Estimation.....	18
3.1.1.1	Auto-Correlation Based Estimators.....	20
3.1.2	Joint Symbol Time and CFO Estimation	23
3.2	Modified Mehlan Chen Meyr (MCM) Algorithm.....	24
3.2.1	Full Response Binary CPM with $h=1/2$	25
3.2.2	Full Response Quaternary CPM with $h=1/4$	29
3.2.3	Partial Response Binary CPM with $h=1/2, L=2$	31
3.2.4	Symbol Time Estimation	33
3.3	Modified Mengali Morelli (M&M) Algorithm.....	33
3.3.1	Full Response Quaternary CPM with $h=1/4$	34
3.3.2	Full Response Octal CPM with $h=1/8$	34
3.4	Comparison of the Modified MCM and the M&M Estimation Method	35
3.5	Simulation Results	37
3.5.1	Simulation Model	37
3.5.2	Criteria for CFO and Symbol Time Estimation	40
3.5.2.1	Cramer-Rao Bound (CRB) and Modified CRB (MCRB).....	40
3.5.2.2	BER or SER Measurement.....	42
3.5.3	Results	43
3.5.3.1	Modified MCM Estimation for Full Response Binary CPM.....	43
3.5.3.2	Modified MCM Estimation for Quaternary CPM.....	51
3.5.3.3	Modified MCM Estimation for Partial Response Binary CPM with $h=1/2, L=2$	56
3.5.3.4	M&M Estimation Method for Full Response Binary CPM	64
3.5.3.5	Modified M&M Estimation Method for Quaternary CPM	69
3.5.3.6	Modified M&M Estimation Method for Octal CPM.....	75
4	SYMBOL DETECTION	79
4.1	Literature Survey.....	79
4.2	Reduced State Viterbi Differential Detection (Adachi's Detection Method) with Joint CFO and Symbol Timing Estimation	90
4.3	Simulation Results.....	96
5	CONCLUSION AND FUTURE WORKS	106

6	REFERENCES.....	109
----------	------------------------	------------

LIST OF TABLES

TABLES

Table 2-1 Definition of the frequency pulse functions $g(t)$	10
--	----

LIST OF FIGURES

FIGURES

Figure 2-1 Rectangular pulse.	5
Figure 2-2 Instantaneous frequency of low-pass equivalent waveform.....	6
Figure 2-3 Instantaneous phase of low-pass equivalent waveform.....	6
Figure 2-4 Integration of rectangular pulse.....	9
Figure 2-5 Phase trajectory for binary CPFSK.	11
Figure 2-6 The phase trellis of binary CPFSK in case of CFO.	12
Figure 2-7 Trellis diagram for binary CPFSK with $h=1/2$	14
Figure 2-8 MSK power spectral density.....	16
Figure 3-1 Mehlan Chen Meyr [12] CFO estimation algorithm.	22
Figure 3-2 Received signal model.	25
Figure 3-3 The phase trellis of binary CPFSK in case of CFO for $h=1/2$	28
Figure 3-5 Flowchart to remove ambiguity.	29
Figure 3-4 Block diagram to produce auto-correlations.....	29
Figure 3-6 Phase trellis for Quaternary CPM with $h=1/4$	31
Figure 3-7 Phase tree for partial response ($L=2$) binary CPM signals with $h=1/2$ in the absence of CFO.	32
Figure 3-8 General Simulation Model.....	37
Figure 3-9 Impulse response of the RC filter for different values of the roll-off factor.	38
Figure 3-10 Frequency response of the RC filter for different values of the roll-off factor.	39
Figure 3-11 BER versus E_b/N_0 plot for MSK signals with different oversampling ratios.....	44
Figure 3-12 BER versus E_b/N_0 plot comparison of RC, REC and BPSK.	45
Figure 3-13 BER versus E_b/N_0 plot comparison of RC with CFO.	46
Figure 3-14 BER versus E_b/N_0 plot comparison with theoretical curves.....	47
Figure 3-15 Estimated versus Actual CFO for RC pulse with $N=16$, $L=64$	48

Figure 3-16 Actual versus Estimated CFO for modified MCM with D=1 and D=2 at $E_b/N_0=10\text{dB}$.	48
Figure 3-17 BER vs CFO for modified MCM with D=1.	49
Figure 3-18 Standard deviation of CFO estimates versus different CFO values for modified MCM with D=1, 2 and 4.	49
Figure 3-19 Standard deviation of CFO estimates versus E_b/N_0 for different D values.	51
Figure 3-20 Mean of CFO estimates versus E_s/N_0 for CFO=0.	52
Figure 3-21 Standard deviation of CFO estimates versus E_s/N_0 for CFO=0.	52
Figure 3-22 Mean of CFO estimates versus E_s/N_0 for CFO=0.05.	54
Figure 3-23 Standard deviation of CFO estimates versus E_s/N_0 for CFO=0.05.	54
Figure 3-24 Mean of CFO estimates versus E_s/N_0 for CFO=0.10.	55
Figure 3-25 Standard deviation of CFO estimates versus E_s/N_0 for CFO=0.10.	55
Figure 3-26 Mean of CFO estimates versus E_s/N_0 for CFO=0.15.	56
Figure 3-27 Mean of CFO estimates versus E_b/N_0 for CFO=0.	57
Figure 3-28 Standard deviation of CFO estimates versus E_b/N_0 for CFO=0.	57
Figure 3-29 Mean of CFO estimates versus E_b/N_0 for CFO=0.05.	58
Figure 3-30 Standard deviation of CFO estimates versus E_b/N_0 for CFO=0.05.	59
Figure 3-31 Mean of CFO estimates versus E_b/N_0 for CFO=0.10.	59
Figure 3-32 Standard deviation of CFO estimates versus E_b/N_0 for CFO=0.10.	60
Figure 3-33 Mean of CFO estimates versus E_b/N_0 for CFO=0.15.	61
Figure 3-34 Standard deviation of CFO estimates versus E_b/N_0 E_b/N_0 for CFO=0.15.	61
Figure 3-35 Standard deviation of CFO estimates versus E_b/N_0 for partial response CPM signals with CFO=0.	63
Figure 3-36 MSE of timing estimates for partial response binary CPM signals.	63
Figure 3-37 Mean of CFO estimates vs actual CFO for binary RC, $h=0.5$.	65
Figure 3-38 Standard deviation of CFO estimates versus E_b/N_0 for CFO=0.	65
Figure 3-39 Comparison of the M&M and the modified MCM method for CFO=0.	66
Figure 3-40 Comparison of the M&M and the modified MCM method for CFO=0.10.	66
Figure 3-41 Mean square error of symbol timing estimates for binary RC signal.	67

Figure 3-42 BER versus E_b/N_0 with uniformly distributed timing offset over $[-T/2, T/2]$.	69
Figure 3-43 Mean value of CFO estimates for quaternary CPM signals.	70
Figure 3-44 Standard deviation of CFO estimates for quaternary CPM signals.	71
Figure 3-45 Standard deviation of CFO estimates versus E_s/N_0 for quaternary CPM signals with CFO=0.	71
Figure 3-46 Mean value of CFO estimates versus E_s/N_0 for quaternary CPM signals with CFO=0.05.	72
Figure 3-47 Standard deviation of CFO estimates versus E_s/N_0 for quaternary CPM signals with CFO=0.05.	72
Figure 3-48 MSE of timing estimates versus E_s/N_0 for quaternary CPM signals with CFO=0.	74
Figure 3-49 Symbol error rate versus SNR for quaternary CPM signals with $h=1/4$.	75
Figure 3-50 Mean value of CFO estimates versus E_s/N_0 for octal CPM signals with CFO=0.05.	76
Figure 3-51 Standard deviation of CFO estimates versus E_s/N_0 for octal CPM signals with CFO=0.05.	76
Figure 3-52 MSE of symbol-timing estimates versus E_s/N_0 for octal CPM signals with CFO=0.	78
Figure 3-53 Symbol error rate versus E_s/N_0 for 8-ary CPM signals.	78
Figure 4-1 Block diagram of Adachi's RSV DD Algorithm.	88
Figure 4-2 Trellis diagram for 4DPSK (solid lines show surviving paths).	89
Figure 4-3 Block diagram of Adachi's DF DD Algorithm.	90
Figure 4-4 Trellis diagram for binary CPM (solid lines show surviving paths).	92
Figure 4-5 Block diagram of RSV DD algorithm coupled with estimation block.	93
Figure 4-6 Trellis diagram for quaternary CPM (solid lines show surviving paths).	96
Figure 4-7 BER vs SNR for RSV DD of binary CPM signals	98
Figure 4-8 BER vs SNR for CDD and RSV DD of binary CPM signals.	98
Figure 4-9 BER vs SNR for CDD and RSV DD of binary CPM signals.	99
Figure 4-10 BER vs SNR for RSV DD of binary CPM signals.	100
Figure 4-11 BER vs SNR for RSV DD of binary CPM signals with $\Delta fT=0.01$.	101
Figure 4-12 BER vs SNR for RSV DD of binary CPM signals with $\Delta fT=0.05$.	101

Figure 4-13 BER vs SNR for RSV DD of binary CPM signals with $\Delta fT=0.10$ 102
Figure 4-14 BER vs SNR for RSV DD of binary CPM signals with $\Delta fT=0.1875$. 103
Figure 4-15 SER vs SNR for RSV DD of quaternary CPM signals with $\Delta fT=0$. . 104
Figure 4-16 BER vs SNR for RSV DD of partial response CPM signals with $\Delta fT=0$.
..... 105

LIST OF ABBREVIATIONS

AWGN: Additive White Gaussian Noise
BER: Bit Error Rate
BPSK: Binary Phase Shift Keying
CDD: Conventional Differential Detection
CFO: Carrier Frequency Offset
CDPD: Cellular Digital Packet Data
CPM: Continuous Phase Modulation
CPFSK: Continuous Phase Shift Keying
CRB: Cramer Rao Bound
DCS: Digital Communication System
DD: Differential Detection
DECT: Digital Enhanced Cordless Telephone
DFSE: Decision Feedback Sequence Estimation
DF DD: Decision Feedback Differential Detection
DPSK: Differential Phase Shift Keying
FFT: Fast Fourier Transform
GMSK: Gaussian Minimum Shift Keying
GSM: Global Systems Mobile Communications
IF: Intermediate Frequency
ISI: Inter Symbol Interference
MAP: Maximum A posteriori
MCM: Mehlan Chen Meyr
M&M: Mengali and Morelli
MSE: Mean Square Error
ML: Maximum Likelihood
MLSD: Maximum Likelihood Sequence Detection
MSK: Minimum Shift Keying

MCRB: Modified CRB
PSD: Power Spectrum Density
PSP: Per Survivor Processing
QPSK: Quaternary Phase Shift Keying
RSSD: Reduced State Sequence Detection
RSSE: Reduced State Sequence Estimation
RSV DD: Reduced State Viterbi Differential Detection
SER: Symbol Error Rate
SNR: Signal to Noise Ratio
8PSK: 8-ary Phase Shift Keying

CHAPTER 1

INTRODUCTION

1.1 Motivation

Spectral efficiency is a precious resource and an important design consideration for wireless communications systems. Low-power and energy efficiency is also an important characteristic requirement of current and future communication systems. It is important both from a mobile terminal perspective, when especially the lifetime on a single battery charge is an important figure of merit, as well as for a base station, where electricity costs and thermal problems are major reasons to look for low power solutions [1].

Continuous phase modulation (CPM) is a digital modulation scheme in which the memory is added while phase-modulating to provide continuity of phase over time which yields high spectral efficiency. CPM is very attractive for wireless communications when considering limited frequency spectrum and power environments of wireless communications because of two major properties: good spectral efficiency and a constant envelope property. Constant envelope property of CPM allows to use power-efficient nonlinear amplifiers. Among CPM, GMSK (Gaussian minimum shift keying) is an important scheme for its spectral properties being used in Bluetooth, DECT, GSM, DCS, CDPD, and Mobitex as well as some military applications.

The carrier phase, the correct symbol timing, and the frequency offset due to channel, distance between receiver and transmitter, oscillator inaccuracy or Doppler effects have to be recovered in order to demodulate the received signal. In order to save bandwidth, all the information needed for synchronization must

be extracted from the modulated received signal. Optimal solutions like maximum-likelihood (ML) or maximum-a-posteriori (MAP) often cost large algorithmic complexity in order to estimate the carrier phase, the correct symbol timing, and the frequency offset jointly [2]. In practice, suboptimal solutions can be preferred if satisfactory performance is obtained from simpler receivers.

CPM schemes require an accurate phase reference for coherent demodulation, owing to sensitivity to phase jitter. It can be difficult to extract the carrier accurately enough in some cases. Differential demodulation is a structure that eliminates the need for a phase reference with high accuracy, where the current symbol is demodulated using the previous symbol. Differential detection is very attractive for applications where low receiver complexity is needed, because accurate carrier phase recovery is not necessary [3]. In order to demodulate the received signal, symbol clock and carrier frequency offset (CFO) still have to be recovered.

CPM signals can be optimally demodulated using maximum likelihood sequence detection (MLSD), main drawback of which is complexity to implement as it consists of a high number of matched filters followed by a Viterbi algorithm [2] [4]. The complexity of MLSD increases exponentially with the length of the memory and the size of the alphabet [4]. In the literature, several approaches have been introduced for reducing the receiver complexity [5]- [11].

In [6] and [7], the primary idea behind reduced state sequence detection (RSSD) is to construct a trellis with a reduced number of states and to use this trellis in the Viterbi detector. [8] and [9] proposed a method for reduced complexity demodulation of CPM signals, which is based upon the extended Laurent representation of the non-linear CPM modulation as a sum of time-offset pulse amplitude modulations. [10] described a highly structured reduced state sequence estimator for inter symbol interference (ISI) channels using set partitioning concepts combined with decision feedback. The reduced-state Viterbi algorithm (VA), with feedback incorporated into the structure of path metric computations is

presented in [11] for the differential detection of M-ary differential phase shift keying (DPSK) signals.

The objective of this thesis study is to examine low complexity symbol detection as well as joint estimation of CFO and symbol timing for a feedforward differential CPM demodulation. In [12], a noncoherent feedforward differential minimum shift keying (MSK) demodulator with joint frequency offset and symbol timing estimation using 1-symbol differential phase information was proposed. We have modified this demodulator in the case when raised cosine frequency pulse is used. Frequency estimation of this demodulator has also been improved using multiple symbol phase differences. Joint frequency and timing recovery algorithm described in [13], which is applicable to the entire class of MSK-type signals using 1-to-M symbol differential phase with $M \geq 1$, has also been implemented embedding in this modified [12] demodulator. Both algorithms described in [12] and [13] were proposed for only binary MSK or MSK-type signals. Both algorithms have been adapted to operate properly for quaternary and octal signaling. Additionally, we have considered modulation indices of $h=0.25$ and $h=0.125$ for narrower bandwidth occupancy [4]. Furthermore, the demodulators using both algorithms have been modified for partial response signals. Estimation performances of all these implemented algorithms in additive white Gaussian noise (AWGN) channel have been presented.

Finally, the BER (bit error rate) or SER (symbol error rate) performances of these demodulators were enhanced by applying reduced state Viterbi differential detection. Performance results of all demodulators in AWGN channel have been presented.

1.2 Organization of the Thesis

The presentation of this thesis is organized into the following chapters.

In Chapter 2, basic information about CPM is reviewed.

Chapter 3 summarizes CFO and symbol timing estimation methods found in the literature. Then, improvements on some of these methods are proposed. In addition, simulation results on the AWGN channel are presented.

Chapter 4 provides some symbol detection methods that have appeared in the literature, and describes Reduced State Viterbi Differential Detection algorithm combined with joint CFO and symbol timing estimation. At the end of the chapter, simulation results on the AWGN channel are given.

Finally, Chapter 5 provides a summary and conclusions of this thesis along with suggestions for further research.

CHAPTER 2

BACKGROUND INFORMATION

In this chapter, introductory information about CPM, continuous phase shift keying (CPFSK) and related concepts are presented. More detailed information about these subjects can be found in [4], [2], [14].

2.1 CPFSK

In order to generate a CPFSK signal, a pulse amplitude modulation (PAM) signal $d(t)$ is used to frequency-modulate the carrier

$$d(t) = \sum_n I_n g(t - nT), \quad (2.1)$$

where the sequence of amplitudes obtained by mapping k -bit blocks of binary digits from the information sequence into the amplitude levels $I_n = \{\pm 1, \pm 3, \dots, \pm(M-1)\}$ and $g(t)$ is a rectangular pulse of amplitude $1/2T$ and duration T seconds shown in Figure 2-1.

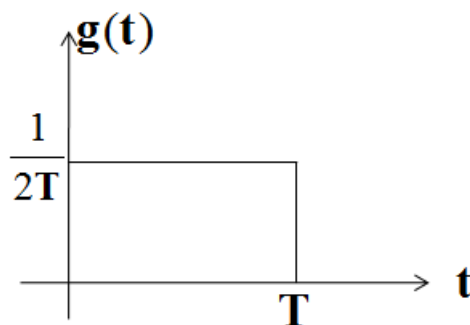


Figure 2-1 Rectangular pulse.

Since the signal $d(t)$ is used to frequency-modulate the carrier, the equivalent low-pass waveform $v(t)$ is expressed as

$$v(t) = \sqrt{\frac{2\varepsilon}{T}} \exp \left\{ j \left[4\pi T f_d \int_{-\infty}^t d(\tau) d\tau + \phi_0 \right] \right\}, \quad (2.2)$$

where

- f_d : the peak frequency deviation
- ϕ_0 : the initial phase of the carrier.

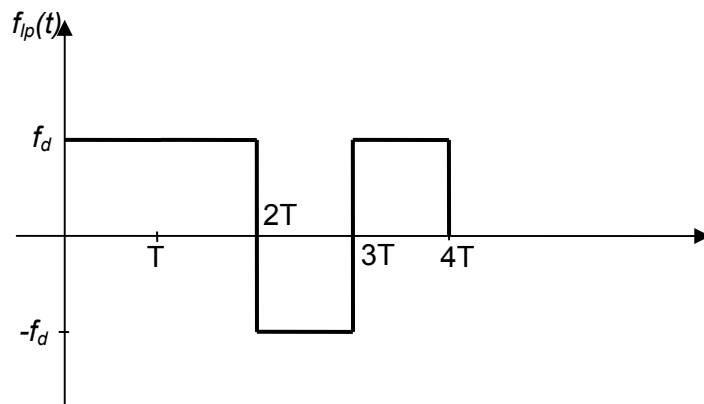


Figure 2-2 Instantaneous frequency of low-pass equivalent waveform.

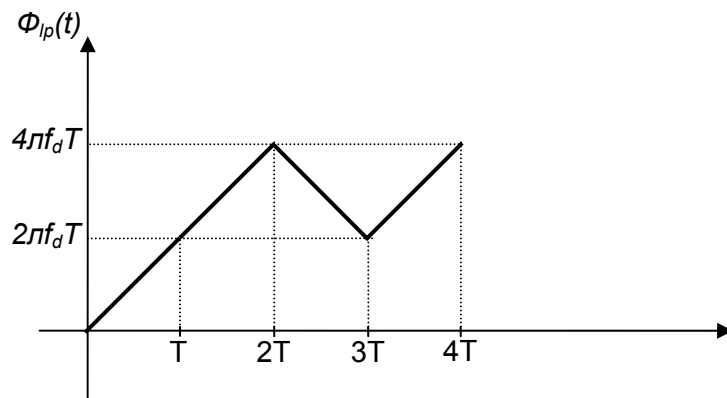


Figure 2-3 Instantaneous phase of low-pass equivalent waveform.

The instantaneous frequency (in Hz) of low-pass equivalent waveform becomes

$$f_{lp}(t) = f_d \sum_n I_n g(t - nT). \quad (2.3)$$

The instantaneous phase of low-pass equivalent waveform is given by

$$\begin{aligned} \phi_p(t) &= 2\pi \int_{-\infty}^t f_{lp}(\tau) d\tau \\ &= 4\pi T f_d \int_{-\infty}^t \left[\sum_n I_n g(\tau - nT) \right] d\tau \end{aligned} \quad (2.4)$$

The carrier-modulated signal with a carrier frequency of f_c corresponding to $v(t)$ may be expressed as

$$\begin{aligned} s(t) &= \sqrt{2} \operatorname{Re} \left[\underbrace{\sqrt{\frac{2\varepsilon}{T}} e^{j\phi_p(t)}}_{v(t)} e^{j2\pi f_c t} \right] \\ &= \sqrt{\frac{2\varepsilon}{T}} \cos[2\pi f_c t + \phi(t; \mathbf{I}) + \phi_0], \end{aligned} \quad (2.5)$$

where $\phi(t; \mathbf{I})$ represents the time-varying phase of the carrier, which is defined as follows

$$\begin{aligned} \phi(t; \mathbf{I}) &= 4\pi T f_d \int_{-\infty}^t d(\tau) d\tau \\ &= 4\pi T f_d \int_{-\infty}^t \left[\sum_n I_n g(\tau - nT) \right] d\tau \end{aligned} \quad (2.6)$$

Note that, although $d(t)$ contains discontinuities, the integral of $d(t)$ is continuous. Hence, we have a continuous phase signal.

Also note that

$$\int_{-\infty}^t \sum_n I_n g(\tau - nT) d\tau = \sum_n \left\{ I_n \left[\int_{-\infty}^t g(\tau - nT) d\tau \right] \right\} \quad (2.7)$$

and

$$\int_{-\infty}^t g(\tau - nT) d\tau = \int_{nT}^t \frac{1}{2T} d\tau = \frac{1}{2T} (t - nT) \quad nT \leq t \leq (n+1)T \quad (2.8)$$

$$\int_{-\infty}^t g(\tau - nT) d\tau = \frac{1}{2} \quad t \geq (n+1)T \quad (2.9)$$

$$\int_{-\infty}^t g(\tau - nT) d\tau = 0 \quad t \leq nT \quad (2.10)$$

The phase of the carrier in the interval $nT \leq t \leq (n+1)T$ can be determined by integrating $\phi(t; \mathbf{I})$.

$$\begin{aligned} \phi(t; \mathbf{I}) &= 2\pi f_d T \sum_{k=-\infty}^{n-1} I_k + 2\pi f_d (t - nT) I_n \\ &= \theta_n + 2\pi h I_n q(t - nT), \end{aligned} \quad (2.11)$$

where h , θ_n , and $q(t)$ are defined as follows

$$h = 2\pi f_d T, \quad (2.12)$$

$$\theta_n = \pi h \sum_{k=-\infty}^{n-1} I_k, \quad (2.13)$$

$$\begin{aligned} q(t) &= \int_0^t g(\tau) d\tau \\ &= \begin{cases} 0 & t < 0 \\ t/2T & 0 \leq t \leq T \\ \frac{1}{2} & t > T \end{cases} \end{aligned} \quad (2.14)$$

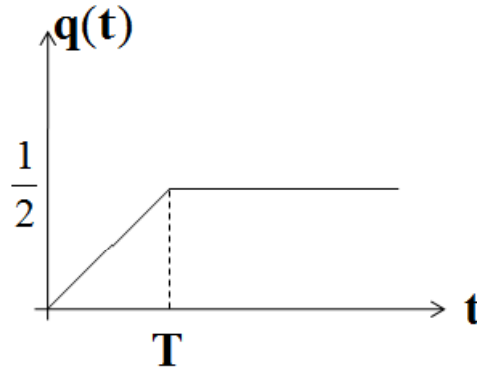


Figure 2-4 Integration of rectangular pulse.

θ_n represents the accumulation (memory) of all symbols up to time $(n-1)T$. The parameter h is called the modulation index.

The time-varying frequency of the carrier-modulated signal is

$$f(t) = f_c + f_d \sum_n I_n g(t - nT). \quad (2.15)$$

2.2 Continuous Phase Modulation (CPM)

CPM is a generalized class of CPFSK by allowing:

- non-rectangular frequency pulses
- different modulation indices per symbol
- frequency pulses with duration $LT, L > 1$

The carrier phase of the signal is given by

$$\phi(t; \mathbf{I}) = 2\pi \sum_{k=-\infty}^n I_k h_k q(t - kT), \quad nT \leq t \leq (n+1)T \quad (2.16)$$

where

$\{h_k\}$: sequence of modulation indices

$\{I_k\}$: sequence of M-ary information symbols with $I_k \in \{\pm 1, \pm 3, \dots, \pm(M-1)\}$

$q(t)$: normalized waveform shape.

CPFSK is a special form of CPM where $h_k = h$ for all k , and $q(t)$ is given by equation (2.14). When h_k varies from one symbol to another, it is called "multi-h" CPM.

Recall that the waveform $q(t)$ is defined as follows

$$q(t) = \int_0^t g(\tau) d\tau. \quad (2.17)$$

- If $g(t) = 0$ for $t > T$, the modulated signal is called “full response CPM”.
- If $g(t) \neq 0$ for $t > T$, the modulated signal is called “partial response CPM”.

An infinite variety of CPM signals can be generated by choosing different pulse shapes $g(t)$, modulation index h and the alphabet size M . Some of the more popular pulse shapes are listed in Table 2-1. In Table 2-1 the notation LRC is used for a raised cosine pulse of length L symbol intervals. Thus, 3RC is a raised cosine pulse of length $3T$. This notation will be used through the thesis. The rectangular pulse of length L is denoted LREC. The pulse of length $1T$, that is 1REC, is referred to as CPFSK in the literature. The 2REC pulse with length $2T$ is also called duobinary.

Table 2-1 Definition of the frequency pulse functions $g(t)$.

LRC	$g(t) = \begin{cases} \frac{1}{2LT} [1 - \cos(\frac{2\pi t}{LT})] & ; 0 \leq t \leq LT \\ 0 & ; \text{otherwise} \end{cases}$ <p>L is the pulse length, e.g. 3RC has $L=3$.</p>
LREC	$g(t) = \begin{cases} \frac{1}{2LT} & ; 0 \leq t \leq LT \\ 0 & ; \text{otherwise} \end{cases}$ <p>$L=1$ yields 1REC which is referred to as CPFSK.</p>
GMSK	$g(t) = \left\{ Q \left[\frac{2\pi B(t - T/2)}{\sqrt{\ln(2)}} \right] - Q \left[\frac{2\pi B(t + T/2)}{\sqrt{\ln(2)}} \right] \right\}$ <p>where $Q(t) = \int_{-t}^{\infty} \frac{1}{\sqrt{2\pi}} e^{-x^2/2} dx, 0 \leq BT < \infty$.</p>

2.2.1 Phase Tree and Trellis Diagram

In the case of CPFSK with binary symbols $I_n = \pm 1$, the variation of phase $\phi(t, I)$ with time t follows a path consisting of a sequence of straight lines, the slopes of which represent frequency changes. Figure 2-5 shows all possible paths starting from time $t = 0$. A plot like that shown in Figure 2-5 is called a *phase tree*. The tree graph clearly shows the transitions of phase across interval boundaries of the incoming sequence of data symbols. The phase tree shown in Figure 2-5 is a clear depiction of phase continuity, which is an inherent characteristic of a CPFSK signal.

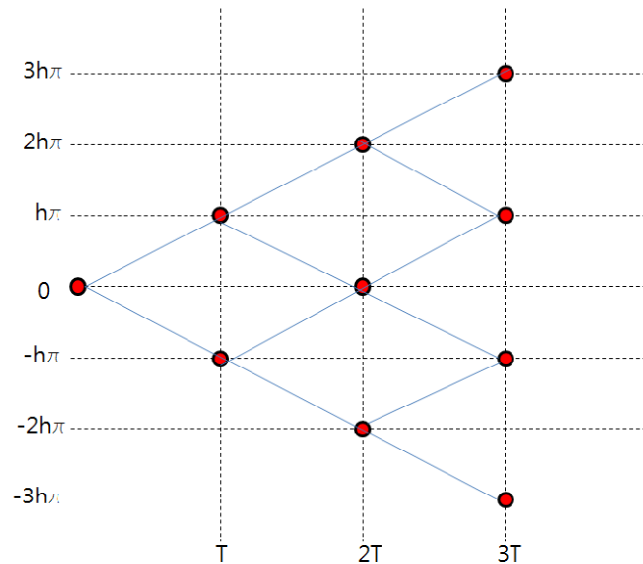


Figure 2-5 Phase trajectory for binary CPFSK.

In the presence of CFO, Δf is introduced, the time-varying phase of low-pass equivalent waveform becomes

$$\phi_p(t) = 2\pi\Delta f t + 4\pi T f_d \int_{-\infty}^t \left[\sum_n I_n g(\tau - nT) \right] d\tau. \quad (2.18)$$

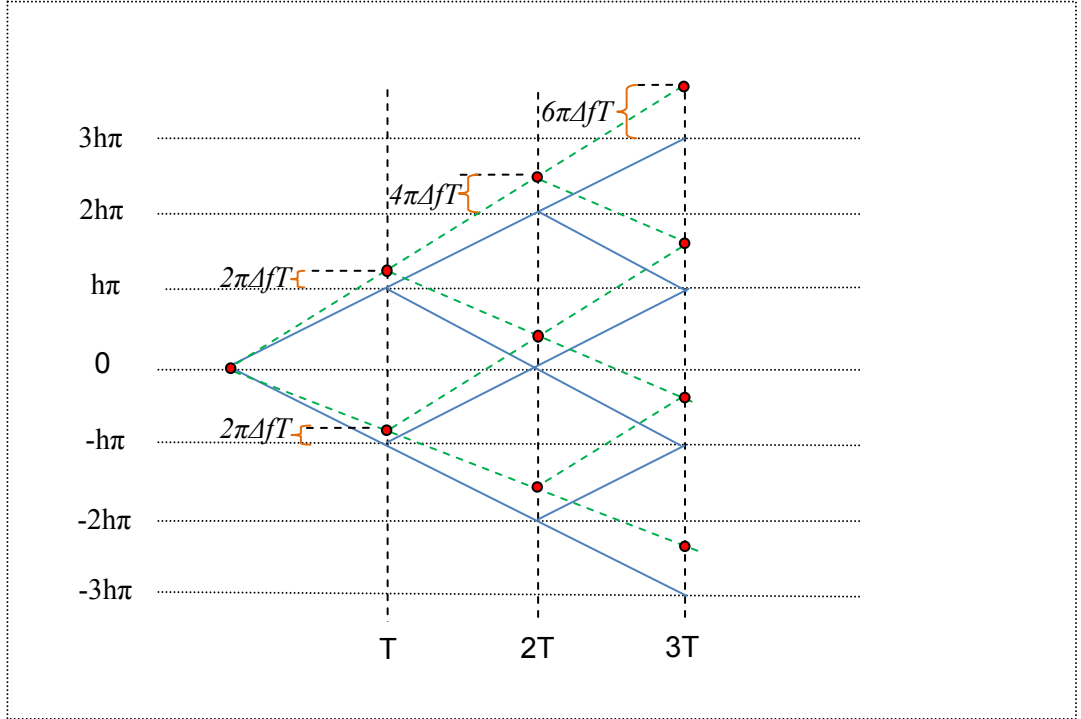


Figure 2-6 The phase trellis of binary CPFSK in case of CFO.

The phase trellis of the binary CPFSK signal with CFO is shown in Figure 2-6.

MSK is a special form of binary CPM where the modulation index $h = \frac{1}{2}$, and the pulse is 1REC. The phase of the carrier is

$$\begin{aligned} \phi(t; I) &= \frac{1}{2} \pi \sum_{k=-\infty}^{n-1} I_k + \pi I_n q(t - nT), \quad nT \leq t \leq (n+1)T \\ &= \theta_n + \frac{1}{2} \pi I_n \left(\frac{t - nT}{T} \right), \quad nT \leq t \leq (n+1)T \end{aligned} \quad (2.19)$$

and the modulated carrier signal is

$$\begin{aligned} s(t) &= \sqrt{\frac{2\mathcal{E}}{T}} \cos \left[2\pi f_c T + \theta_n + \frac{1}{2} \pi I_n \left(\frac{t - nT}{T} \right) \right] \\ &= \sqrt{\frac{2\mathcal{E}}{T}} \cos \left[2\pi \left(f_c + \frac{1}{4T} I_n \right) t - \frac{1}{2} n\pi I_n + \theta_n \right], \quad nT \leq t \leq (n+1)T \end{aligned} \quad (2.20)$$

The binary CPFSK signal can be represented as a sinusoid with one of two possible frequencies for $nT \leq t \leq (n+1)T$. These frequencies are

$$\begin{aligned}
f_1 &= f_c - \frac{1}{4T}, \\
f_2 &= f_c + \frac{1}{4T}.
\end{aligned} \tag{2.21}$$

So the signal can be written in the form

$$s_i(t) = \sqrt{\frac{2\varepsilon}{T}} \cos \left[2\pi f_i t + \theta_n + \frac{1}{2} n\pi (-1)^{i-1} \right], \quad i = 1, 2 \tag{2.22}$$

The frequency separation $\Delta f = f_2 - f_1 = 1/2T$ is the minimum frequency separation that is necessary to ensure the orthogonality of the signals $s_1(t)$ and $s_2(t)$ over a signaling interval of T . This is why this type of modulation is called minimum-shift keying (MSK) [4], [2].

Showing only the values of the signal phase at the time instants $t = nT$, we obtain simpler representations than phase trees. Rewriting the carrier phase of the signal

$$\phi(t; \mathbf{I}) = 2\pi \sum_{k=n-L+1}^{n-1} I_k h_k q(t-kT) + 2\pi h_n I_n q(t-nT) + \pi \sum_{k=-\infty}^{n-L} I_k h_k, \quad nT \leq t \leq (n+1)T \tag{2.23}$$

since $q(t) = 0$ for $t < 0$ and $q(t) = 1/2$ for $t > LT$, the phase is unique for any symbol interval n , given $\{h_k\}$ and $g(t)$. The first term on the right-hand side of equation (2.23) depends on the information symbols $(I_{n-1}, I_{n-2}, \dots, I_{n-L+1})$, which is called the *correlative state vector*, and represents the phase term corresponding to signal pulses that have not reached their final value. The unique phase is defined by the present symbol I_n , the correlative state vector $(I_{n-1}, I_{n-2}, \dots, I_{n-L+1})$, and the phase state θ_n , where

$$\theta_n = \left[\pi \sum_{k=-\infty}^{n-L} I_k h_k \right] \text{ modulo } 2\pi. \tag{2.24}$$

The number of correlative states is M^{L-1} , since each element of the correlative state vector $(I_{n-1}, I_{n-2}, \dots, I_{n-L+1})$ may have M possible values.. Let us assume $h = m/p$, for relatively prime integers m and p . At time instants $t = nT$, we obtain the terminal phase states

$$\theta_n \in \left\{ 0, \frac{\pi m}{p}, \frac{2\pi m}{p}, \dots, \frac{(p-1)\pi m}{p} \right\} \quad (2.25)$$

if m is even and

$$\theta_n \in \left\{ 0, \frac{\pi m}{p}, \frac{2\pi m}{p}, \dots, \frac{(2p-1)\pi m}{p} \right\} \quad (2.26)$$

if m is odd.

We have p phase states if m is even and 2p phase states if m is odd. Hence, L-tuple total states of the phase is

$$\sigma_n = \left(\underbrace{\theta_n}_{\text{phase state}}, \underbrace{I_{n-1}, I_{n-2}, \dots, I_{n-L+1}}_{\text{correlative states}} \right) \quad (2.27)$$

and there are pM^{L-1} phase states for even m, $2pM^{L-1}$ phase states for odd m.

For instance, there are total 4 phase states in the case of binary CPFSK signal with $h = 1/2$. The trellis diagram for this example is given in Figure 2-7. We observe that there are always two branches coming in and going out at a state. In general, there are always M branches in and out at a state. Also, the lines connecting states are not trajectories of the signal phases. They show the transitions from one state to the next.

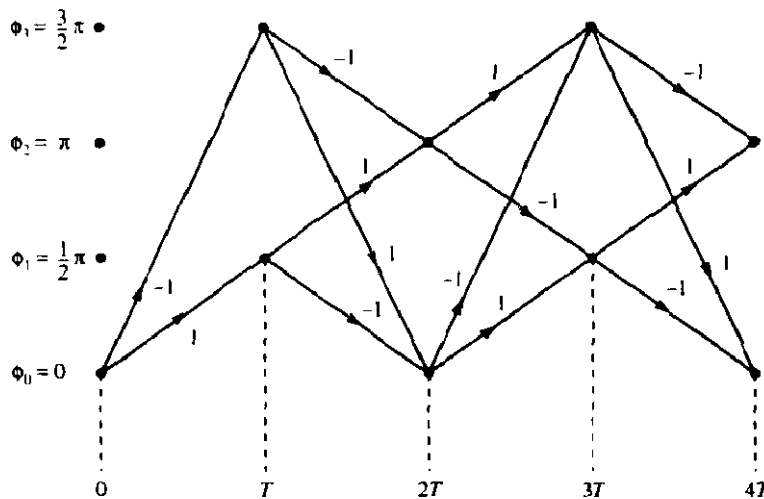


Figure 2-7 Trellis diagram for binary CPFSK with h=1/2.

2.2.2 Power Spectral Density (PSD) of MSK

The MSK signal consists of the in-phase component and the quadrature component, which are independent from each other. The PSD of the complex envelope is the sum of the PSDs of these two components. The PSD of a binary, bipolar (± 1), equiprobable, stationary, and uncorrelated digital waveform is equal to the energy spectral density of the symbol shaping pulse divided by the symbol duration [14]. In MSK, the symbol shaping pulses are

$$p_I(t) = \begin{cases} A \cos\left(\frac{\pi t}{2T}\right), & -T \leq t \leq T \\ 0, & \text{otherwise} \end{cases} \quad (2.28)$$

for in-phase channel and

$$p_Q(t) = \begin{cases} A \sin\left(\frac{\pi t}{2T}\right), & 0 \leq t \leq 2T \\ 0, & \text{otherwise} \end{cases} \quad (2.29)$$

for quadrature channel. Note their durations are $2T$, not T . Since there is only a phase factor between their Fourier transforms, their energy spectral densities are the same. By taking a Fourier transform of either function, and square the magnitude, divide by $2T$, we obtain PSDs of in-phase and quadrature components. Hence, the PSD of MSK signal is

$$\Phi_{ss}(f) = \frac{16A^2T}{\pi^2} \left[\frac{\cos(2\pi Tf)}{1-(4Tf)^2} \right]^2. \quad (2.30)$$

Figure 2-8 shows the PSD of MSK along with those of binary phase shift keying (BPSK), quaternary PSK (QPSK), and offset QPSK (OQPSK). They are plotted as a function of f normalized to the data rate $R_b = 1/T$. The MSK spectrum falls off at a rate proportional to $(f/R_b)^{-4}$ for large values of f/R_b . In contrast, the QPSK or OQPSK spectrum falls off at a rate proportional to only $(f/R_b)^{-2}$. The BPSK

spectrum also falls off at a rate proportional to $(f / R_b)^{-2}$ even though its spectral lobe widths are double that of QPSK or OQPSK. The main lobe of the MSK spectrum is narrower than that of BPSK spectrum and wider than that of the QPSK or OQPSK spectrum. The first nulls of BPSK, MSK, and QPSK or OQPSK spectrum fall at $f / R_b = 1.0, 0.75,$ and $0.5,$ respectively. Therefore, the null-to-null bandwidth is $2.0R_b$ for BPSK, $1.5R_b$ for MSK, and $1.0R_b$ for QPSK or OQPSK.

An algorithm for numerical calculation of CPM spectra is given in [4] and [2].

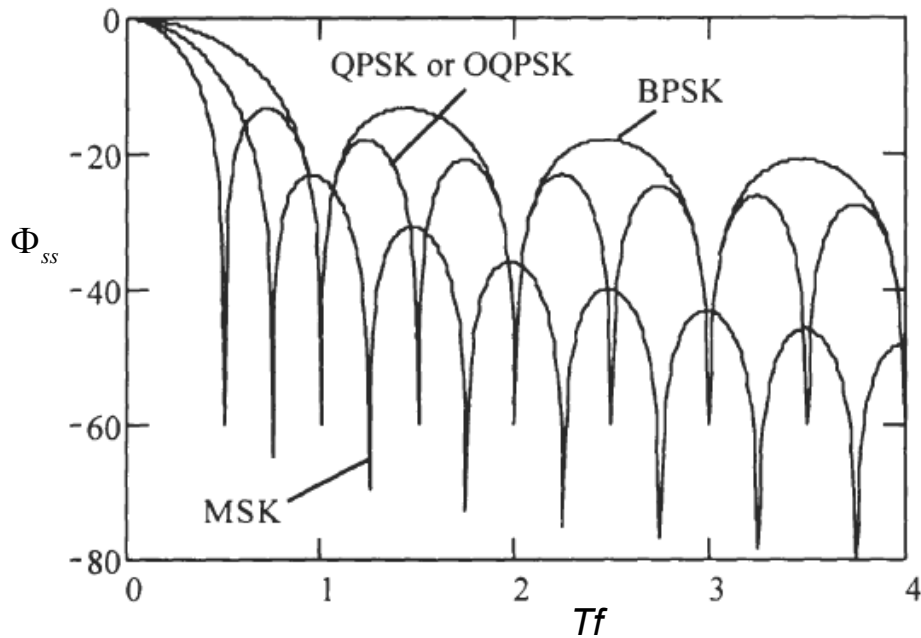


Figure 2-8 MSK power spectral density.

CHAPTER 3

JOINT CARRIER FREQUENCY OFFSET AND SYMBOL TIME ESTIMATION

In a typical communication system, there is frequency offset, carrier phase error and symbol timing error between a receiver and a transmitter. These differences mainly result from channel, distance between the receiver and the transmitter, oscillator inaccuracy or Doppler effects. The carrier phase, correct symbol timing, and the frequency offset have to be recovered in order to demodulate the received signal.

An accurate phase reference is required for coherent demodulation of CPM signals because of sensitivity to phase jitter. In some cases, it may not be easy to extract the carrier phase accurately. Differential demodulation does not need a highly accurate phase reference, since the current symbol is demodulated using the previous symbol. However, using differential demodulation we still have to recover symbol timing and CFO.

Some symbol timing and CFO estimators proposed in the literature are training sequence based estimators (e.g., [15]- [17]) in which a sequence of symbols known by the receiver is used. However, the use of training data lowers the achievable data rate. Therefore, alternative methods that do not make use of pilot symbols or training sequences are desirable. Hence, we are interested in blind estimation methods in which the parameters are determined from the received signal only.

3.1 Literature survey

3.1.1 Carrier Frequency Offset (CFO) Estimation

We concentrate on blind carrier frequency estimation methods in burst-mode digital transmission with MSK-type signaling. In the literature there are different methods based on different concepts, such as algorithms derived from maximum likelihood criteria [18] [19], least-squares-based estimators [20], [21] and auto-correlation-based estimators [12] [13]. Except for the auto-correlation-based estimators [12], [13], the following methods are not capable to estimate symbol timing jointly with the CFO. Hence, the algorithms described in [12], [13] will be described in more detail.

If $x(t)$ represents the transmitted signal, the received signal corrupted by AWGN and CFO is given by

$$z(t) = x(t)e^{j2\pi\Delta f t} + w(t) \quad (3.1)$$

where $w(t)$ is complex additive white Gaussian noise whose real and imaginary parts are independent and identically distributed. Sampling the received signal $z(t)$ with a sampling frequency of T_s , we obtain received sequence z_n .

Rife and Boorstyn [18] have shown that the maximum likelihood (ML) estimate of Δf is the location where the magnitude of

$$A(f) = \frac{1}{L} \sum_{n=0}^{L-1} z_n e^{-j2\pi f n T} \quad (3.2)$$

achieves a maximum, L is the observation length in symbol intervals, and T is the symbol interval.

As there may exist many local maxima, the algorithm in [18] uses a two-part search process in order to find the global maximum of the function $|A(f)|$ using properties of maximum likelihood estimates. Using fast Fourier transform (FFT) techniques, the first part (coarse search) calculates $|A(f)|$ over a discrete set of f -

values covering the uncertainty range of Δf and determines that f which maximizes $|A(f)|$. The second part (fine search) interpolates between samples of $|A(f)|$. and computes the local maximum nearest to the f -value determined in the coarse search. This estimator can be used in low signal-to-noise ratio (SNR) values by adequately increasing the symbol observation length.

In [19], the method described in [18] was applied for MSK type modulations. The accuracy of method in [19] is close to the modified Cramer-Rao bound (MCRB) at high SNR values, but its computational complexity is high as the complexity of the method presented in [18].

In [21], Tretter proposed to convert the additive Gaussian noise to an equivalent additive Gaussian phase noise for large SNR. For example, assuming the received sequence has the form

$$z_n = e^{j2\pi\tilde{f}nT} + w_n, \quad (3.3)$$

where \tilde{f} is the unknown frequency to be estimated and w_n is complex additive white Gaussian noise sequence, the received sequence can be approximated for high SNR values as

$$z_n \cong e^{j(2\pi\tilde{f}nT + \eta_n)}, \quad (3.4)$$

where η_n is also a white Gaussian noise sequence. The principle value of $\arg(z_n)$ may be viewed as noisy samples of a straight line with slope $2\pi\tilde{f}T$. The estimate of the unknown frequency \tilde{f} can be found by estimating the slope of this line. However, the frequency estimate needs to be unwrapped, since there may be jumps by 2π in the trajectory of $\arg(z_n)$. The unwrapping algorithm leads to an additional computational complexity.

In [20], Kay proposed to modify Tretter's estimator [21] by using $\arg(z_n z_{n-1}^*)$ instead of $\arg(z_n)$. In this way, unwrapping can be avoided.

The least-square-based estimators [20], [21] do not perform as well as the algorithm in [18], but performance of the least-square-based estimators, which have less complexity, does not depend on the length of the symbol observation length so much [22].

3.1.1.1 Auto-Correlation Based Estimators

In addition to the algorithms derived from the maximum likelihood criteria and least-squares-based estimators, there are alternative methods based on the sample auto-correlation of square of the received sequence. In following paragraphs, auto-correlation-based estimators [12], [13] will be studied in detail.

In practice, the algorithm proposed in [12] uses twice of 1-symbol phase difference in order to estimate the CFO. Examining Figure 2-6, twice of 1-symbol phase difference takes value $\pi + \Delta\omega T$ for $h=1/2$. Multiplying 1-symbol phase difference by two is done by squaring the product of signal and complex conjugate of 1-symbol delayed signal. For a sampled signal of x_n ,

$$\arg\{(x_n x_{n-1}^*)^2\} = 2[\arg\{x_n\} - \arg\{x_{n-1}\}] \quad (3.5)$$

Actually, this operation is fulfilled by the help of the auto-correlation function of the square of the signal.

In the algorithm in [12], (See Figure 3-1), 1-lag auto-correlation function of $x^2(t)$, where $x(t)$ is the transmitted signal and T is the symbol duration,

$$R(t) = E\left\{\left[x(t)x^*(t-T)\right]^2\right\} \quad (3.6)$$

is to be estimated. This function will be denoted by 2-AC¹ (auto-correlation) function through the thesis. Unfortunately, the transmitted signal is not available and must be estimated from the samples of the received sequence $z_{k,i}$, which

¹ M-AC is used to mean an average value of the M^{th} power of the product $z_{k,i} z_{k-m,i}^*$ for m -lag auto correlation functions of the sequence $z_{k,i}$.

denotes the sample of $z(t)$ taken at time $t=kT+iT_s$, and where T_s is the sampling period letting $N=T/T_s$, we have

$$z_{k,i} = z(t = (k + i / N)T) \text{ with } 0 \leq i \leq N - 1. \quad (3.7)$$

In a digital implementation, the estimation of the expectation is performed by an averaging filter of length L , where L is the number of symbols observed:

$$\hat{R}_{k,i} = \frac{1}{L} \sum_{j=0}^{L-1} [z_{k-j,i} z_{k-j-1,i}^*]^2 \quad (3.8)$$

Hence, estimated frequency offset is equal to

$$\Delta\hat{\omega}T = \frac{\arg\{-\hat{R}_{k,\hat{i}}\}}{2} \quad (3.9)$$

where \hat{i} is the index which gives minimum timing error.

In the algorithm described in [13], besides 1-lag 2-AC functions, $\{2, \dots, m\}$ -lag 2-AC functions are used. m -lag auto-correlation function of $x^2(t)$ is

$$R^m(t) = E \left\{ [x(t)x^*(t-mT)]^2 \right\}. \quad (3.10)$$

The estimate of the 2-AC function is

$$\hat{R}_m(i) = \frac{1}{L-m} \sum_{k=m}^{L-1} [z_{k,i} z_{k-m,i}^*]^2, \quad 0 \leq i \leq N-1, \quad 1 \leq m \leq D. \quad (3.11)$$

$$\Delta\hat{\omega}T = \frac{1}{2D} \sum_{m=1}^D \arg\{-\hat{R}_m(\hat{i}_m) \hat{R}_{m-1}^*(\hat{i}_{m-1})\} \quad (3.12)$$

where \hat{i} is the index which gives minimum timing error.

Examining Figure 2-6, we can represent phase of $\hat{R}_m(\hat{i}_m)$ ideally (without noise) as

$$\arg(\hat{R}_m(\hat{i}_m)) = \begin{cases} \pi + 2m\Delta\omega T, & \text{odd } m \\ 2m\Delta\omega T, & \text{even } m \end{cases} \quad (3.13)$$

which means that

$$\arg(\hat{R}_m(\hat{i}_m)\hat{R}_{m-1}^*(\hat{i}_{m-1})) = \pi + 2\Delta\omega T. \quad (3.14)$$

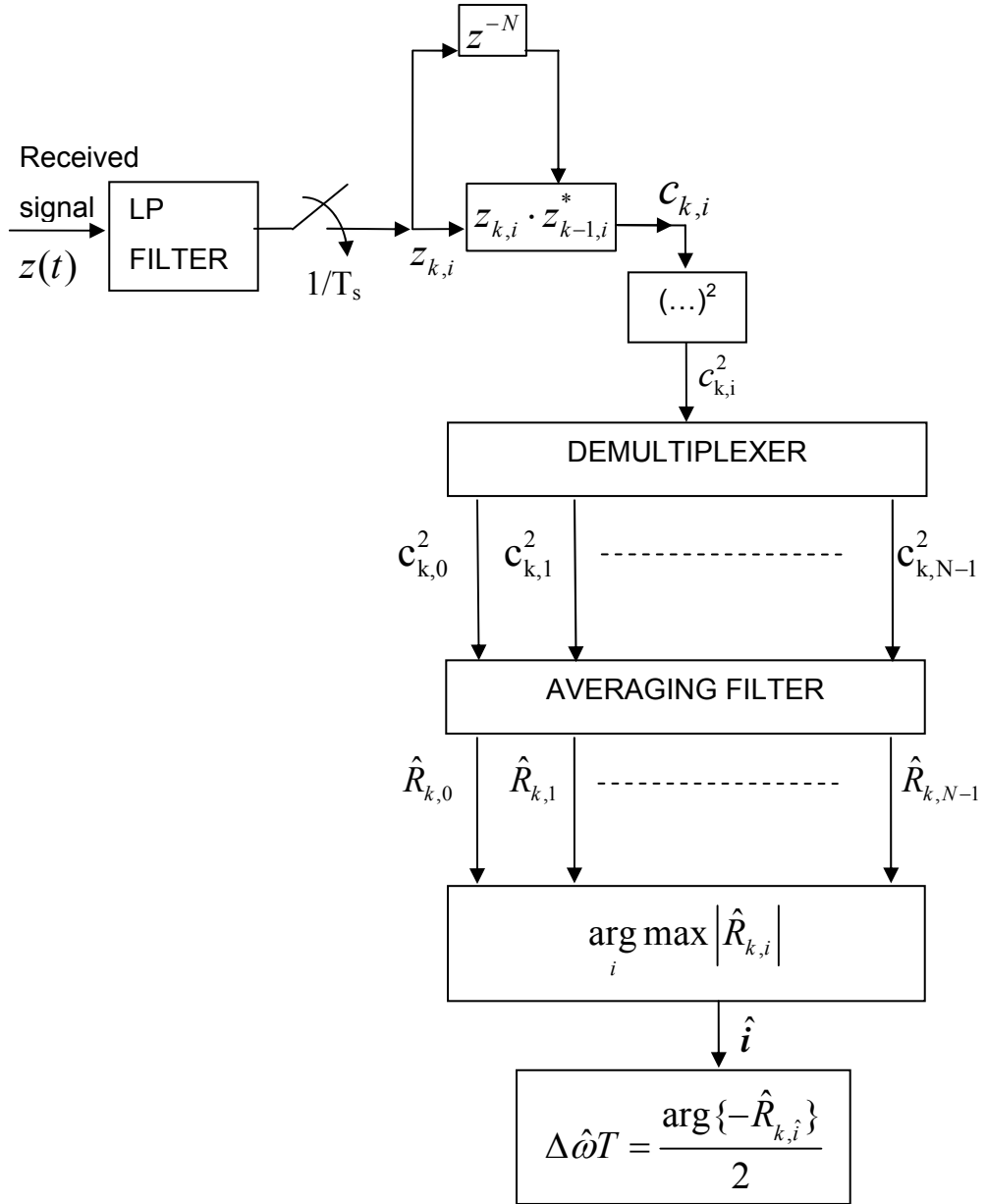


Figure 3-1 Mehlan Chen Meyr [12] CFO estimation algorithm.

Therefore, we have CFO estimates

$$\Delta\hat{\omega}_m T = \frac{1}{2} \arg\{-\hat{R}_m(\hat{i}_m)\hat{R}_{m-1}^*(\hat{i}_{m-1})\} \quad 1 \leq m \leq D. \quad (3.15)$$

Actually, equation (3.11) gives average value of the estimates $\Delta\hat{\omega}_m T$.

As a special case, for $D=1$ frequency estimates are the same as proposed by [12]. So, the method in [13] is an extension of the algorithm in [12] including indexes $m>1$. Furthermore, the algorithm in [13] can be used with any MSK-type signals, whereas the algorithm in [12] is proposed for just MSK.

Both algorithms in [12] and in [13] propose frequency estimation jointly with symbol timing estimation. Hence, an additional symbol-timing algorithm is not necessary if one of these two algorithms is used. Again, both algorithms can manage frequency offsets up to 25% of the symbol rate for binary full response signals. As compared to the algorithm in [12], the algorithm in [13] can be used even with narrow-band modulations.

In [23], D'Andrea et al. proposed a *delay-and-multiply* type frequency estimation algorithm. Denoting by z_n the received sequence obtained by sampling the received signal $z(t)$ with sampling period T_s , the estimate of the CFO is given by

$$\Delta\hat{\omega} = \frac{1}{\Delta T} \arg \left\{ \sum_{n=1}^{NL} z_n z_{n-D}^* \right\} \quad (3.16)$$

where the integer D corresponds to the delay $\Delta T = DT_s$ (T_s is sampling period, and ΔT is time delay). This algorithm operates with multilevel partial response signaling unlike algorithms in [12] and [13], its estimation range is larger (on the order of the symbol rate) than algorithms in [12] and [13]. However, its performance is worse than the performances of algorithms in [12] and [13].

3.1.2 Joint Symbol Time and CFO Estimation

To demodulate the received signal correctly in the receiver, knowledge of carrier phase, symbol timing and frequency offset are required. The optimal synchronization approach, which is known as the ML based joint timing and frequency offset estimation, is described in [2] and [24]. However, it is not very practical due to its computation complexity. Consequently, several suboptimal

approaches, which make tradeoff between synchronization performance and implementation complexity, have been proposed [12], [13], [15]- [17].

In [15]- [17], a training sequence is used for synchronization. However, in our work we concentrate on blind methods, thus algorithms proposed in [12] and [13] will be examined here.

In the algorithm proposed by [12], there are two different strategies to estimate the timing error:

1. \hat{i} found in Figure 3-1 gives the position i with the minimum timing error,
2. estimate of 1-lag 2-AC function in equation (3.8) is used as in the case of CFO estimation:

$$\hat{\tau} = \frac{T}{2\pi} \arg \left\{ \sum_{k=0}^{\bar{M}-1} \sum_{i=0}^{N-1} \left| \hat{R}_{k,i} \right| e^{-j2\pi i/N} \right\} \quad (3.17)$$

where \bar{M} is the length of a filter which smoothes the DFT of $\left| \hat{R}_{k,i} \right|$ taken at $f=1/T$.

If strategy 1 is used for symbol timing estimation, the maximum symbol-timing error will be

$$\left| \tau - \hat{\tau} \right|_{\max} = \frac{T}{2N}. \quad (3.18)$$

In the algorithm proposed by [13], besides 1-lag 2-AC function, $\{1,2,\dots,m\}$ -lag 2-AC functions are used. The estimate of m -lag 2-AC function in equation (3.11) is used in order to find timing error estimate

$$\hat{\tau} = -\frac{T}{2\pi} \arg \left\{ \sum_{i=0}^{N-1} \left[\sum_{m=1}^D \left| \hat{R}_m(i) \right| \right] e^{-j2\pi i/N} \right\}. \quad (3.19)$$

3.2 Modified Mehlan Chen Meyr (MCM) Algorithm

We will assume that the received signal is corrupted with CFO of Δf and white Gaussian noise (See Figure 3-2). In [12], modulation is MSK, so the frequency

pulse is rectangular shape as shown in Figure 2-1. Raised cosine pulse in CPM can be used as an improvement in order to have better spectral properties and prevent ISI. Therefore, we need to extend the MCM algorithm to RC pulsed MSK-type signals for better spectral density and ISI prevention.

CFO and symbol timing problems were investigated for only full response binary signals in the MCM algorithm. As stated in [25], if full response CPM systems are to be used, a more attractive tradeoff between error probability performance and spectrum is achieved by using more levels than two. Again in [26], it was stated that the use of partial response CPM systems yields a more attractive tradeoff between error probability and spectrum than does the full response systems. Hence, we propose to modify the MCM algorithm such that CFO and symbol timing can be estimated for both multi-level and partial response RC pulsed CPM signals.

In addition, 1-symbol phase differences were used to estimate the CFO in the MCM algorithm. We propose to use phase differences over D -symbol interval in the algorithm, where $D \geq 1$. In this way, we can get D times the actual CFO to estimate, which intuitively means CFO can be estimated more accurately for $D > 1$.

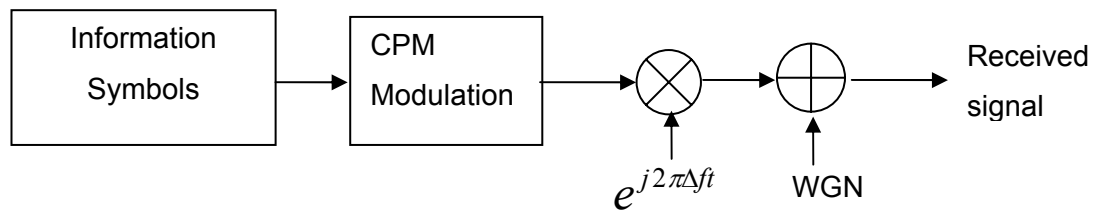


Figure 3-2 Received signal model.

3.2.1 Full Response Binary CPM with $h=1/2$

One of the important modifications on [12] is using D -lag 2-AC functions where D is an integer, $D \geq 1$.

In the case when $D=1$, 1-symbol phase difference can have one of two possible values (See Figure 3-3):

- $\pi/2 + \Delta\omega T$
- $-\pi/2 + \Delta\omega T$

where $\Delta\omega = 2\pi f$.

By the help of 2-AC operation, we obtain twice of 1-symbol phase difference whose value is $\pi + 2\Delta\omega T$ in the interval $[-\pi, \pi]$.

$$\begin{aligned} -\pi &\leq \arg\{-\hat{R}_1(\hat{i}_1)\} \leq \pi \\ -\pi &\leq 2\Delta\omega T \leq \pi \end{aligned} \quad (3.20)$$

That is, $\Delta\omega T$ can be estimated in the interval $[-\pi/2, \pi/2]$.

$$-\pi/2 \leq \Delta\omega T \leq \pi/2 \quad (3.21)$$

When $|\Delta f T| > 0.25$, an ambiguity problem emerges. This is why the MCM algorithm can manage CFO's up to 25% of the symbol rate.

Examining phase trellis of binary CPFSK for modulation index $h=1/2$ given in Figure 3-3, the frequency offset is $2\Delta\omega T$ at time $t=2T$. This means that frequency offset can be determined with a better accuracy with respect to the case of 1-symbol phase difference. However, there is an ambiguity problem to be solved. In the figure, twice of 2-symbol phase difference is $4\Delta\omega T$ at time $t=2T$.

$$-\pi \leq 4\Delta\omega T \leq \pi \quad (3.22)$$

$$-\pi/4 \leq \Delta\omega T \leq \pi/4 \quad (3.23)$$

By using 2-symbol phase differences, we can estimate the CFO in the interval $[-\pi/4, \pi/4]$.

This ambiguity problem can be solved using information of 1-symbol phase differences.

1-lag 2-AC function is

$$\hat{R}_1(i) = \frac{1}{L-1} \sum_{k=1}^{L-1} [z_{k,i} z_{k-1,i}^*]^2, \quad 0 \leq i \leq N-1. \quad (3.24)$$

And 2-lag 2-AC function is

$$\hat{R}_2(i) = \frac{1}{L-2} \sum_{k=2}^{L-1} [z_{k,i} z_{k-2,i}^*]^2, \quad 0 \leq i \leq N-1. \quad (3.25)$$

The block diagram in Figure 3-4 displays how to produce 2-AC functions. The received signal is passed through a low-pass filter, which limits the noise bandwidth. Noting that there are N samples per symbol, signal sampling rate is N/T, where T is symbol period.

Using 1-lag 2-AC functions, the CFO estimate in the principle interval (unambiguous case) is given by

$$\Delta \hat{\omega}_1 T = \frac{1}{2} \arg \{-\hat{R}_1(\hat{i}_1)\}, \quad -\pi/2 \leq \Delta \hat{\omega}_1 T \leq \pi/2. \quad (3.26)$$

Using 2-lag 2-AC functions, the CFO estimate in the principle interval is given by

$$\Delta \hat{\omega}_2 T = \frac{1}{4} \arg \{\hat{R}_2(\hat{i}_2)\}, \quad -\pi/4 \leq \Delta \hat{\omega}_2 T \leq \pi/4. \quad (3.27)$$

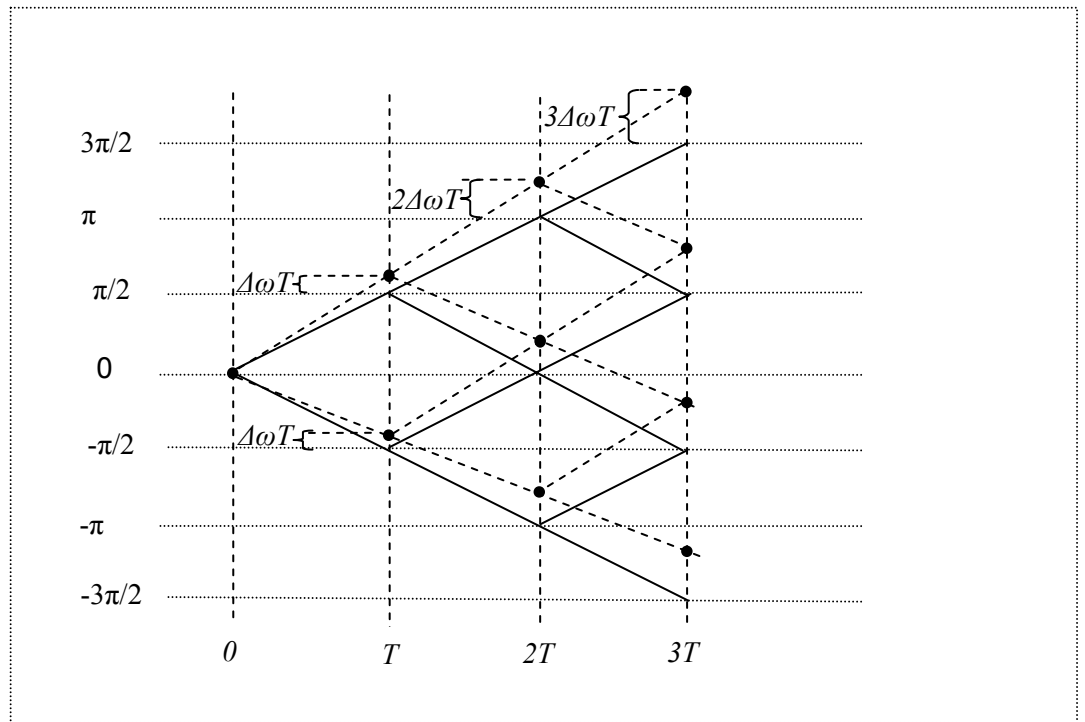


Figure 3-3 The phase trellis of binary CPFSK in case of CFO for $h=1/2$.

The ambiguity of the CFO estimate can be removed using the flowchart shown in Figure 3-5.

More enhancement on CFO estimation can be obtained using D -lag 2-AC functions in the same way as described for 2-symbol phase differences, where D is integer and $D > 2$. Again, there is an ambiguity problem to be solved. In order to remove ambiguity, the CFO estimation found using $D/2$ -lag 2-AC function is employed recursively as in the case $D=2$.

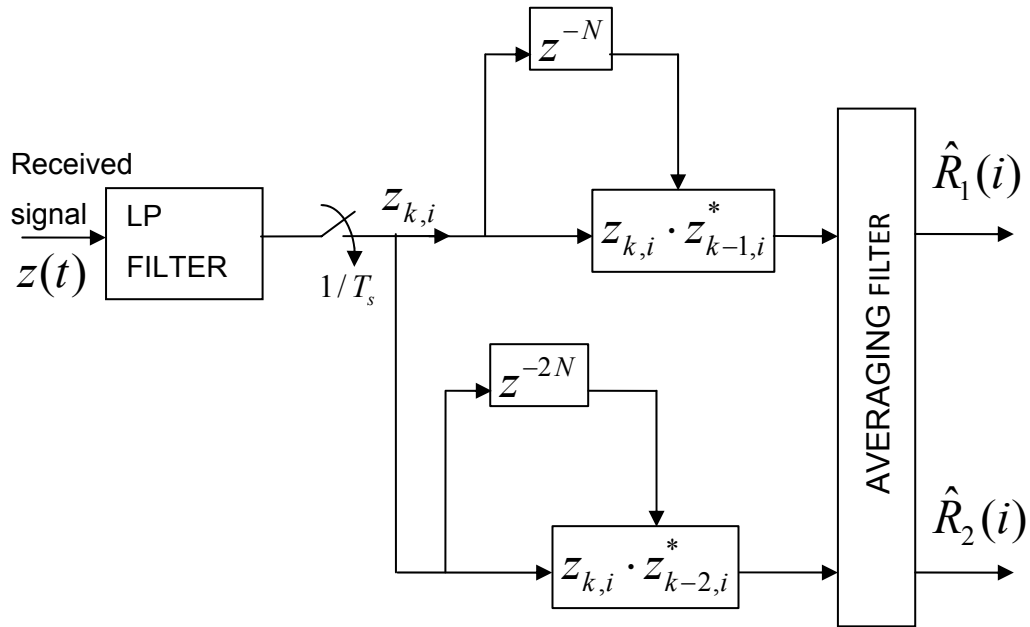


Figure 3-4 Block diagram to produce auto-correlations.

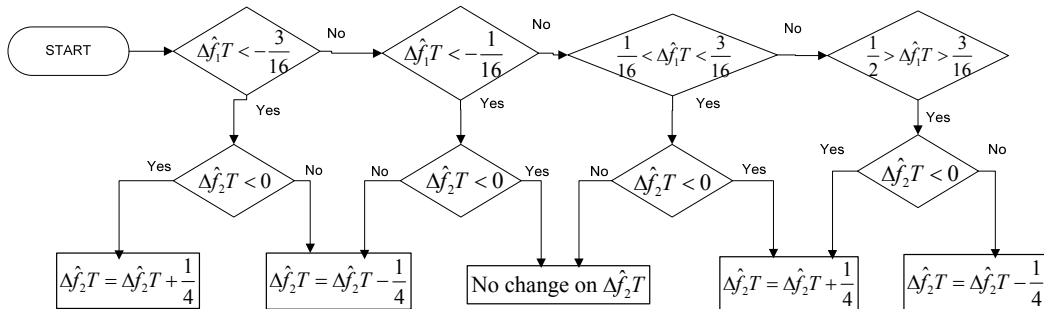


Figure 3-5 Flowchart to remove ambiguity.

3.2.2 Full Response Quaternary CPM with h=1/4

The CFO estimation algorithm in [12] was investigated only for binary case. In this section, we develop an extension of the MCM estimation algorithm, which is applicable to M-ary CPM signals as well.

The phase trellis for quaternary CPM with h=1/4 in the absence of CFO, is shown in Figure 3-6. Examining Figure 3-6, twice of 1-symbol phase differences may

have two different possible values $\{-\pi/2, \pi/2\}$ in $(-\pi, \pi]$ which means that the CFO estimation algorithm in [12] cannot be applied directly for this case. Instead of twice, four times of 1-symbol phase differences have only one value $\pi+4\Delta\omega T$ if there is CFO. Using $\pi+4\Delta\omega T$ value, the CFO can be estimated as proposed in [12].

Instead of the 2-AC² functions that yield the mean value of the square of the product $z_{k,i}z_{k-1,i}^*$, 4-AC functions which yield the mean value of the 4th power of the product $z_{k,i}z_{k-1,i}^*$.given in equation (3.28) can be used.

$$\hat{R}_1(i) = \frac{1}{L-1} \sum_{k=1}^{L-1} [z_{k,i}z_{k-1,i}^*]^4, \quad 0 \leq i \leq N-1 \quad (3.28)$$

Then, the principal value of the CFO can be estimated by

$$\Delta\hat{\omega}_1 T = \frac{1}{4} \arg\{-\hat{R}_1(\hat{i}_1)\}, \quad -\pi/4 \leq \Delta\hat{\omega}_1 T \leq \pi/4. \quad (3.29)$$

In this way, we can estimate $4\Delta\omega T$ in $(-\pi, \pi]$, so we can estimate the CFO in the interval $(-\pi/4, \pi/4]$.

As in the previous case, the CFO at time $2T$ is $2\Delta\omega T$. Hence, 2-lag 4-AC function of the sequence $z_{k,i}$ can be employed to get improved CFO estimations

$$\hat{R}_2(i) = \frac{1}{L-2} \sum_{k=2}^{L-1} [z_{k,i}z_{k-2,i}^*]^4, \quad 0 \leq i \leq N-1 \quad (3.30)$$

$$\Delta\hat{\omega}_2 T = \frac{1}{8} \arg\{\hat{R}_2(\hat{i}_2)\}, \quad -\pi/8 \leq \Delta\hat{\omega}_2 T \leq \pi/8. \quad (3.31)$$

Since four times of 2-symbol phase differences may have only one value in $(-\pi, \pi]$ which equals to $8\Delta\omega T$, an ambiguity problem may not be expected in equation

² M -AC is used to mean an average value of the M^{th} power of the product $z_{k,i}z_{k-m,i}^*$ for m -lag auto correlation functions of the sequence $z_{k,i}$.

(3.30). However, we can only estimate $8\Delta\omega T$ offset in the interval $(-\pi, \pi]$, so we can find CFO's in $(-\pi/8, \pi/8]$. Therefore, an ambiguity problem emerges again. The ambiguity can be removed by using the algorithm shown in Figure 3-5. In this way, we can extend the interval in which CFO can be sensed to $(-\pi/4, \pi/4]$.

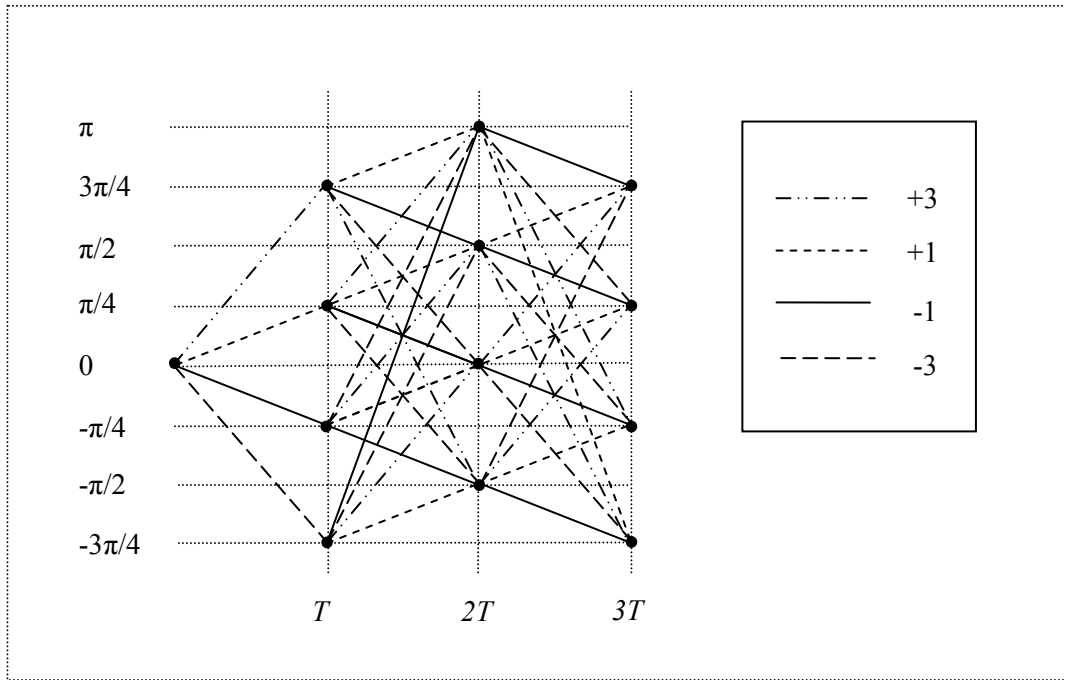


Figure 3-6 Phase trellis for Quaternary CPM with $h=1/4$.

3.2.3 Partial Response Binary CPM with $h=1/2, L=2$

We have extended the algorithm in [12] to partial response CPM signals. As an example, consider the phase tree for partial response ($L=2$) binary CPM with $h=1/2$ in the absence of CFO, shown in Figure 3-7 (assuming the initial symbol is $(+1)$). It can be seen from Figure 3-7 that twice of 1-symbol phase differences may have two different possible values $\{-\pi, 0\}$ in the interval $[-\pi, \pi]$. Hence, it seems that the CFO estimation algorithm in [12] cannot be applied directly for the partial response case. As in full response quaternary CPM case, four times of 1-

symbol phase differences have only one value equal to $4\Delta\omega T$ in the interval $[-\pi, \pi]$. Thus, the 4-AC function in equation (3.28) can be employed instead of the 2-AC function in equation (3.8). CFO estimation can be found using equation (3.28) in

$$\Delta\hat{\omega}_1 T = \frac{1}{4} \arg\{\hat{R}_1(\hat{i}_1)\}, \quad -\pi/4 \leq \Delta\hat{\omega}_1 T \leq \pi/4. \quad (3.32)$$

We can estimate $4\Delta\omega T$ in the interval $(-\pi, \pi]$, so the CFO in the interval $(-\pi/4, \pi/4]$ can be estimated.

2-lag 4-AC functions can be employed to get improved CFO estimations using equations (3.30) and (3.31). We estimate $8\Delta\omega T$ offset in the interval $(-\pi, \pi]$, so we can sense CFO's in $(-\pi/8, \pi/8]$. Consequently, an ambiguity problem appears again. The ambiguity can be eliminated by using the algorithm in Figure 3-5. Then the interval in which CFO can be estimated can be enlarged to $(-\pi/4, \pi/4]$.

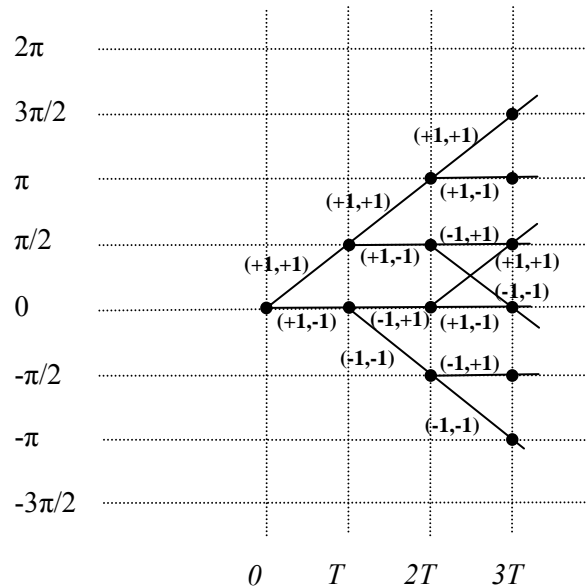


Figure 3-7 Phase tree for partial response (L=2) binary CPM signals with $h=1/2$ in the absence of CFO.

3.2.4 Symbol Time Estimation

Symbol timing estimation for all cases described in section 3.2, can be performed by using

$$\hat{i} = \arg \max_i |\hat{R}_1(i)|. \quad (3.33)$$

Since signal sampling rate is N/T , the symbol phase estimate is

$$\hat{\tau} = \begin{cases} \hat{i} \frac{T}{N} & , \hat{i} < 8 \\ (\hat{i} - 16) \frac{T}{N} & , \hat{i} \geq 8 \end{cases} \quad (3.34)$$

Each $\hat{\tau}$ value can be expressed as an integer multiple of the sampling period T/N . Hence, there exists a quantization error while estimating symbol timing. The maximum symbol-timing error will be

$$|\tau - \hat{\tau}|_{\max} = \frac{T}{2N}. \quad (3.35)$$

Moreover, more accurate symbol timing estimation can be achieved by

$$\hat{\tau} = \frac{T}{2\pi} \arg \left\{ \sum_{i=0}^{N-1} |\hat{R}_1(i)| e^{-j2\pi i/N} \right\} \quad (3.36)$$

as suggested in [19].

3.3 Modified Mengali Morelli (M&M) Algorithm

Mengali and Morelli [13] proposed to use $\{1, 2, \dots, m\}$ -lag 2-AC functions in order to estimate CFO and symbol timing jointly for MSK-type signals, i.e. CPM subclass with binary alphabet and modulation index equal to 0.5. Estimation of 2-AC functions and CFO can be performed as given in equations (3.11) and (3.12), respectively. The MCM estimation algorithm can be regarded as a special case of the M&M algorithm where only 1-lag 2-AC function is used for estimation. In section 3.2.2, we have shown that the MCM algorithm cannot be applied directly for M-ary CPM signals with modulation indices $h=1/M$ for $M>2$, since twice of 1-symbol phase difference (phase of 1-lag 2-AC function corresponds to twice of 1-symbol phase difference) may have more than one value in the interval $(-\pi, \pi]$. Due

to the same reason, we cannot estimate CFO by applying the M&M algorithm directly to M-ary CPM signals with modulation indices $h=1/M$. Therefore, we need to extend the M&M estimation algorithm to multi-level CPM signals.

We have modified the algorithm presented in [13] to be applied for quaternary alphabet with $h=1/4$ and octal alphabet with $h=1/8$. The modification approach is similar to the one applied for adapting the algorithm proposed in [12] to quaternary CPM signals with $h=0.25$ and octal CPM signals with 0.125 . Namely, the approach is based on changing 2-AC function in equation (3.11) to M -AC functions for M-ary signals with $h=1/M$.

3.3.1 Full Response Quaternary CPM with $h=1/4$

The 4-AC function to estimate the CFO for quaternary CPM signals with $h=0.25$ is

$$\hat{R}_m(i) = \frac{1}{L-m} \sum_{k=m}^{L-1} [z_{k,i} z_{k-m,i}^*]^4, \quad 0 \leq i \leq N-1, \quad 1 \leq m \leq D. \quad (3.37)$$

And the CFO estimate can be expressed as

$$\Delta \hat{\omega} T = \frac{1}{4D} \sum_{m=1}^D \arg \{ -\hat{R}_m(\hat{i}_m) \hat{R}_{m-1}^*(\hat{i}_{m-1}) \}. \quad (3.38)$$

The symbol timing estimate can be computed by substituting the 4-AC function computed by equation (3.37) into equation (3.19).

3.3.2 Full Response Octal CPM with $h=1/8$

The 8-AC (auto-correlation) function to estimate the CFO for octal CPM signals with $h=0.125$ is

$$\hat{R}_m(i) = \frac{1}{L-m} \sum_{k=m}^{L-1} [z_{k,i} z_{k-m,i}^*]^8, \quad 0 \leq i \leq N-1, \quad 1 \leq m \leq D. \quad (3.39)$$

And the CFO estimate can be expressed as

$$\Delta\hat{\omega}T = \frac{1}{8D} \sum_{m=1}^D \arg\{-\hat{R}_m(\hat{i}_m)\hat{R}_{m-1}^*(\hat{i}_{m-1})\}. \quad (3.40)$$

The symbol timing estimate can be computed by substituting the 8-AC function computed by equation (3.39) into equation (3.19)

3.4 Comparison of the Modified MCM and the M&M Estimation Method

In the modified MCM algorithm, more than 1-symbol phase differences are employed in order to find CFO more accurately. However, an ambiguity problem emerges by using D-symbol phase differences for integers $D>1$. This ambiguity can be eliminated by using $\lceil D/2 \rceil$ -symbol phase differences. For example, the ambiguity can be eliminated using 1-symbol, 2-symbol, and 4-symbol phase differences (i.e. 1-lag, 2-lag, and 4-lag 2-AC functions) for $D=4$ and binary signals. The CFO estimates are

$$\Delta\hat{\omega}_1T = \frac{1}{2} \arg\{-\hat{R}_1(\hat{i}_1)\}, \quad -\pi/2 \leq \Delta\hat{\omega}_1T \leq \pi/2. \quad (3.41)$$

$$\Delta\hat{\omega}_2T = \frac{1}{4} \arg\{\hat{R}_2(\hat{i}_2)\}, \quad -\pi/4 \leq \Delta\hat{\omega}_2T \leq \pi/4. \quad (3.42)$$

$$\Delta\hat{\omega}_4T = \frac{1}{8} \arg\{\hat{R}_4(\hat{i}_4)\}, \quad -\pi/8 \leq \Delta\hat{\omega}_4T \leq \pi/8. \quad (3.43)$$

where \hat{R}_m is m-lag 2-AC function. The ambiguity can be eliminated by making some comparisons of $\Delta\hat{\omega}_1T$, $\Delta\hat{\omega}_2T$, and $\Delta\hat{\omega}_4T$ as shown in Figure 3-5.

In the M&M algorithm, CFO is estimated by using again properties of auto-correlation (M-AC) functions. For $1 \leq m \leq D$, we have CFO estimates

$$\Delta\hat{\omega}_mT = \frac{1}{2} \arg\{-\hat{R}_m(\hat{i}_m)\hat{R}_{m-1}^*(\hat{i}_{m-1})\}, \quad -\pi/2 \leq \Delta\hat{\omega}_mT \leq \pi/2. \quad (3.44)$$

In this way, the CFO ambiguity is eliminated inherently without needing additional ambiguity elimination process. Averaging D CFO estimates, we can estimate the CFO more accurately.

$$\Delta\hat{\omega}T = \frac{1}{2D} \sum_{m=1}^D \arg\{-\hat{R}_m(\hat{i}_m)\hat{R}_{m-1}^*(\hat{i}_{m-1})\} \quad (3.45)$$

Assuming unambiguous case,

$$\arg\{-\hat{R}_m(\hat{i}_m)\hat{R}_{m-1}^*(\hat{i}_{m-1})\} = \pi + \arg\{\hat{R}_m(\hat{i}_m)\} - \arg\{\hat{R}_{m-1}(\hat{i}_{m-1})\}, \quad (3.46)$$

$$\begin{aligned} \sum_{m=1}^D \arg\{-\hat{R}_m(\hat{i}_m)\hat{R}_{m-1}^*(\hat{i}_{m-1})\} &= \pi + \arg\{\hat{R}_D(\hat{i}_D)\} - \arg\{\hat{R}_{D-1}(\hat{i}_{D-1})\} \\ &\quad + \pi + \arg\{\hat{R}_{D-1}(\hat{i}_{D-1})\} - \arg\{\hat{R}_{D-2}(\hat{i}_{D-2})\} \\ &\quad + \dots \\ &\quad + \pi + \arg\{\hat{R}_1(\hat{i}_1)\} - \arg\{\hat{R}_0(\hat{i}_0)\} \end{aligned} \quad (3.47)$$

$$\begin{aligned} \sum_{m=1}^D \arg\{-\hat{R}_m(\hat{i}_m)\hat{R}_{m-1}^*(\hat{i}_{m-1})\} &= D\pi + \arg\{\hat{R}_D(\hat{i}_D)\} \\ &= \begin{cases} \pi + \arg\{\hat{R}_D(\hat{i}_D)\}, & \text{if } D \text{ is odd} \\ \arg\{\hat{R}_D(\hat{i}_D)\}, & \text{if } D \text{ is even} \end{cases} \end{aligned} \quad (3.48)$$

$$\Delta\hat{\omega}T = \frac{1}{2D} \arg\{(-1)^D \hat{R}_D(\hat{i}_D)\} \quad (3.49)$$

The previous expression is the same as the one we have derived for even D values in the modified MCM algorithm. Thus, we have shown that both the M&M and the modified MCM methods would yield to the same result if there were no ambiguity.

In the modified MCM method, we need comparison operations for the ambiguity elimination process if $D > 1$ and D is integer power of 2. On the other hand, we do not need an ambiguity elimination process in the M&M method, since the ambiguity is eliminated inherently by this method. However, we may have additional computations of 2-AC and $\arg()$ functions in the M&M method. For example for $D=8$, we need to compute 8 2-AC functions and 8 $\arg()$ functions in

order to find CFO estimates in the M&M method, while we need to compute 4 2-AC functions and 4 arg() functions in the modified MCM method.

3.5 Simulation Results

3.5.1 Simulation Model

A general block diagram of the simulation model for the works described in this chapter is shown in Figure 3-8.

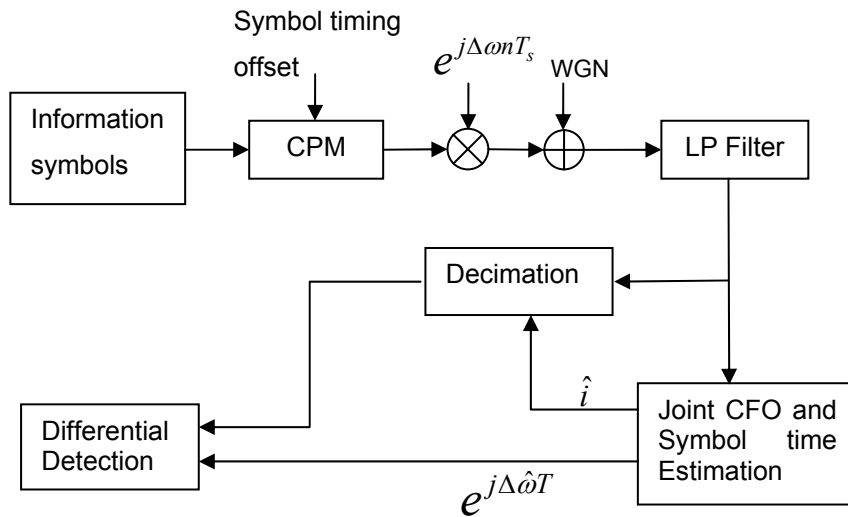


Figure 3-8 General Simulation Model.

Firstly, a sequence of M-ary information symbols with length L $I_k \in \{\pm 1, \pm 3, \dots, \pm(M-1)\}$ is generated randomly. Then a CPM modulated signal is produced taking symbol timing delay and oversampling ratio $N=T/T_s$ into consideration where T is the symbol period and T_s is the sampling period. Symbol timing is simulated by time-delaying the waveform $q(t)$ given in equation (2.17). The modulated signal is realized in the baseband form. The frequency offset is included by multiplying the modulated signal with $e^{j\Delta\omega nT_s}$. Complex additive white

Gaussian noise samples whose real and imaginary parts are independent with two-sided power spectral density $N_0/2$ Watts/Hz each are added.

The resultant waveform is fed to a low-pass filter to reject the out-of-band noise. In simulations, a raised cosine filter is employed [27]. The impulse response of that filter is given by

$$h(t) = \text{sinc}\left(\frac{t}{T}\right) \frac{\cos\left(\frac{\pi}{T}\right)}{1 - \frac{4\beta^2 t^2}{T^2}} \quad (3.50)$$

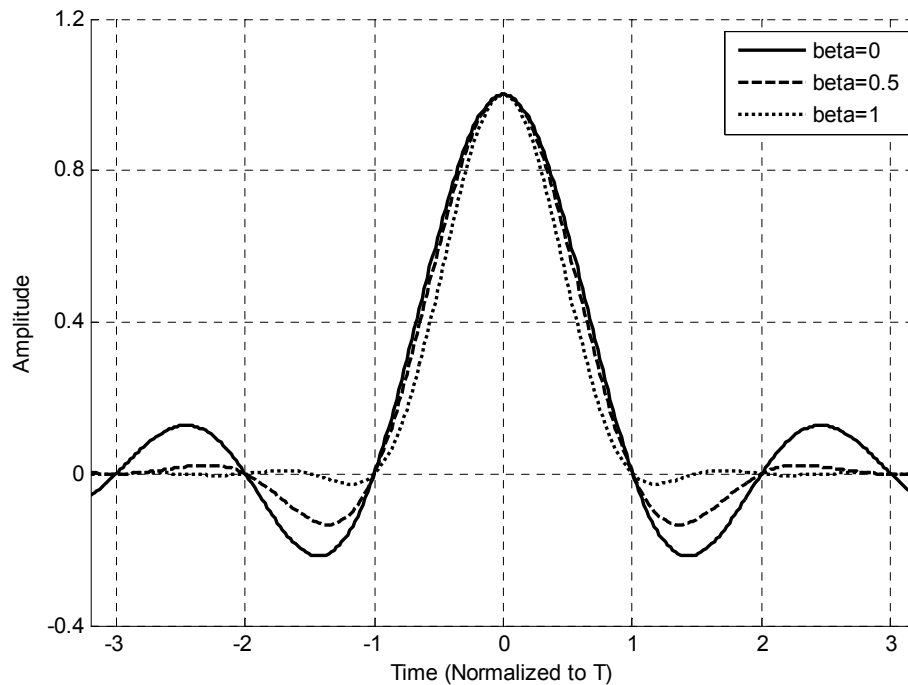


Figure 3-9 Impulse response of the RC filter for different values of the roll-off factor.

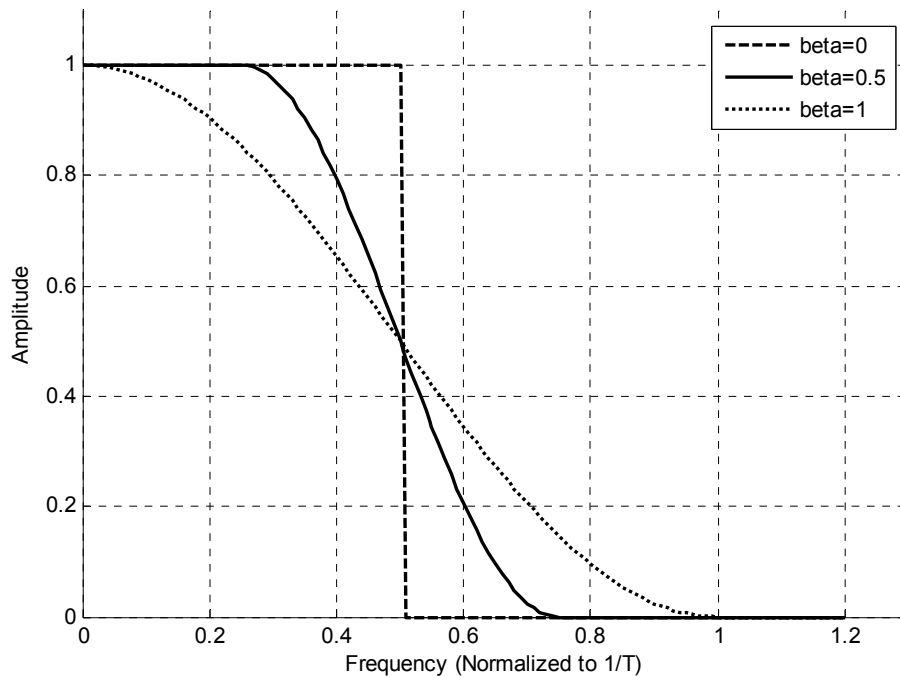


Figure 3-10 Frequency response of the RC filter for different values of the roll-off factor.

where β is the roll-off factor, which determines the filter bandwidth and takes values in the range $0 \leq \beta \leq 1$. and T is the reciprocal of the symbol-rate. For different values of the roll-off factor β , the impulse response and the frequency response of the RC filter is illustrated in Figure 3-9 and Figure 3-10.

Since the roll-off factor and filter bandwidth are two important parameters that affect the performance of the demodulator, we have optimized these filter parameters in order to obtain optimum BER (or SER) performance or estimation performance. The optimal values of the parameters are given together with the corresponding simulation results in section 3.5.3.

Finally, the joint estimation of CFO and symbol timing is carried out. The symbol timing and CFO estimates are used in order to compensate the frequency shifts and decimate the signal to the symbol rate at a proper phase. This operation is

performed by selecting the index, which correspond to the one with minimum timing error, out of N samples. Hence the sampling frequency is decimated to the symbol rate. Due to its simplicity, a decimator is chosen for handling the timing error. As long as over sampling rate is high enough (E.g. ≥ 8), the losses due to quantization of the symbol timing estimate are negligible.

Note that, ideal frame synchronization is assumed in the simulations associated with symbol timing estimation.

Eventually, information symbols are detected by differentially processing the synchronized signal. Unless otherwise specified, symbol-by-symbol differential detection is operated in simulations. The phase difference between the present symbol and the previous symbol gives the present symbol phase difference. For example, positive symbol phase difference implies (+1) information symbol in the binary alphabet case. The symbol detection of partial response signals is done by using the reduced state Viterbi algorithm, which will be described in section 4.2.

3.5.2 Criteria for CFO and Symbol Time Estimation

Before evaluating the estimation methods, we first focus on the tools used to measure the performance of methods

3.5.2.1 Cramer-Rao Bound (CRB) and Modified CRB (MCRB)

In order to evaluate the maximum accuracy that can be obtained in estimation, The Cramer-Rao inequality provides a bound on the variance of any unbiased estimate.

If $\hat{\tau}(\mathbf{r})$ is any unbiased estimate of τ depending on the observation vector \mathbf{r} , then a lower bound can be found [28]

$$\begin{aligned}
\text{Var}(\hat{\tau}(\mathbf{r}) - \tau) &\geq \text{CRB}(\tau) \\
\text{CRB}(\tau) &= \frac{1}{E_r \left\{ \left[\frac{\partial \ln p(\mathbf{r} | \tau)}{\partial \tau} \right]^2 \right\}} \\
&= \frac{1}{E_r \left\{ \frac{\partial^2 \ln p(\mathbf{r} | \tau)}{\partial \tau^2} \right\}}
\end{aligned} \tag{3.51}$$

where $p(\mathbf{r} | \tau)$ the probability density function of \mathbf{r} for a given τ .

To compute $\text{CRB}(\tau)$ we need $p(\mathbf{r} | \tau)$ which can be obtained from the integral in equation (3.52) by averaging out the unwanted parameters from $p(\mathbf{r} | \mathbf{u}, \tau)$, where the vector \mathbf{u} of unwanted parameters contains data symbols plus other parameters to be estimated.

$$p(\mathbf{r} | \tau) = \int_{-\infty}^{\infty} p(\mathbf{r} | \mathbf{u}, \tau) p(\mathbf{u}) d\mathbf{u} \tag{3.52}$$

where $p(\mathbf{u})$ is known probability density function of \mathbf{u} . $p(\mathbf{r} | \mathbf{u}, \tau)$, the conditional probability density function of \mathbf{r} given \mathbf{u} and τ , is easily available, at least for additive Gaussian channels.

Unfortunately, in many practical cases, the computation of CRB is impossible because either the integration in equation (3.52) cannot be carried out analytically or the expectation in equation (3.51) is impossible to overcome.

Calculation of the modified CRB is easier. However, MCRBs are generally looser than CRBs [29]. Generally, the relation between CRB and MCRB is

$$\text{CRB}(\tau) \geq \text{MCRB}(\tau). \tag{3.53}$$

MCRBs are computed for frequency and time estimation of CPM signals in [30]. MCRB for time estimation of CPM signals with LREC and LRC pulses have been found in [30]:

$$\text{MCRB}(\tau) = \frac{T^2 L}{2\pi^2 h^2 L_0} \frac{1}{E_s / N_0}, \text{ with LREC} \tag{3.54}$$

$$MCRB(\tau) = \frac{T^2 L}{3\pi^2 h^2 L_0} \frac{1}{E_s / N_0}, \text{ with LRC} \quad (3.55)$$

MCRB for CFO estimation of CPM signals is

$$MCRB(f) = \frac{3}{2\pi^2 T^2 L_0^3} \frac{1}{E_s / N_0}. \quad (3.56)$$

where L_0 is the number of symbols in the observation interval.

3.5.2.2 BER or SER Measurement

To specify system performance practically, the BER or SER is often evaluated. BER (or SER) can be defined as the number of bit (or symbol) errors divided by the total number of number of bits (or symbols) sent.

To estimate BER with Monte Carlo method, a large number of symbols are processed by the system and errors are counted. If N bits are passed through the system out of which N_e errors occur, then the estimate of error probability is

$$P_e = \frac{N_e}{N}. \quad (3.57)$$

Due to the parameter estimation errors, a BER degradation, which is called *detection loss* [31], emerges as compared to perfect synchronization.

While comparing BER (or SER) performance of digital communication systems, BER (or SER) vs E_b/N_0 (or E_s/N_0) plots are useful. E_b/N_0 denotes for ratio of bit energy to noise power spectral density. The relation between sample SNR and E_b/N_0 can be expressed as

$$\text{sample SNR} = \frac{E \left\{ |v_k|^2 \right\}}{E \left\{ |z_k|^2 \right\}} = \frac{R_b}{f_s} \frac{E_b}{N_0} \quad (3.58)$$

where R_b is bit rate, f_s is sampling frequency, v_k is low-pass equivalent of transmitted signal, z_k is a sequence of complex noise samples whose imaginary and real parts have PSD of N_0 each.

The relationship between E_s/N_0 and E_b/N_0 , both expressed in dB, is as follows:

$$\left(\frac{E_s}{N_0}\right)_{dB} = \left(\frac{E_b}{N_0}\right)_{dB} + 10 \log_{10}(k) \quad (3.59)$$

where k is the number of information bits per symbol.

3.5.3 Results

3.5.3.1 Modified MCM Estimation for Full Response Binary CPM

Firstly, the MCM demodulator is implemented for MSK signals without any CFO and time delay. The symbol length of information sequence is taken as $L=64$. The low-pass filter used in this implementation has a bandwidth of $BT=1.46$ and a roll-off factor $\beta=0.60$.

In order to test the simulator, BER vs E_b/N_0 plot for BPSK signals with oversampling ratios 4, 8, 16, 32 is illustrated in Figure 3-11. In addition, BER vs E_b/N_0 plot for MSK signals with different oversampling ratios is shown in the figure to determine a proper value for oversampling ratio N , As a comparison basis, BER vs E_b/N_0 plots for ideal BPSK are also depicted in the same plot; theoretical BER performance of BPSK in AWGN is expressed as

$$P_b = Q\left(\frac{2\epsilon_b}{N_0}\right) \quad (3.60)$$

where

$$Q(x) = \int_x^{\infty} \frac{1}{\sqrt{2\pi}} e^{-t^2/2} dt \quad (3.61)$$

BER performance of experimental BPSK is consistent with theoretical BPSK performance, i.e. the simulator has been verified. There is about 3dB degradation of BER for MSK compared to BPSK, due to noncoherent detection. Note that, as oversampling ratio increases, BER performance of MSK improves slightly. This is due to better decimation results as N increases. Examining the figure, BER vs E_b/N_0 plots for MSK signals do not improve much for $N \geq 16$. Then it is sufficient to take $N=16$.

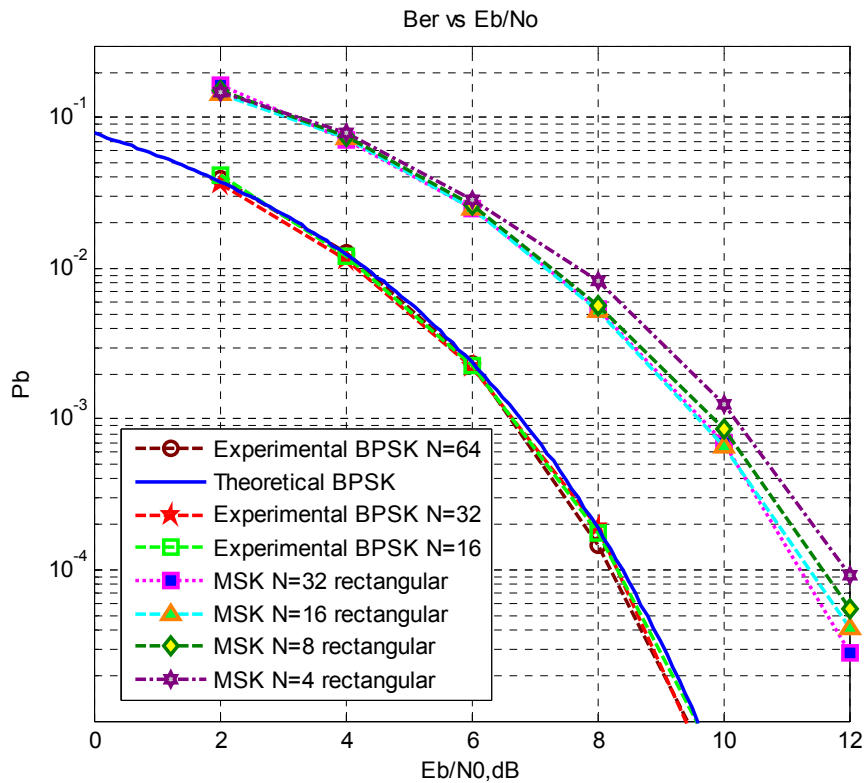


Figure 3-11 BER versus E_b/N_0 plot for MSK signals with different oversampling ratios.

CPM signal with pulse of 1RC, modulation index $h=0.5$ and $N=16$ is also simulated using an RC type IF filter with a bandwidth of $BT=1.43$, a roll-off factor $\beta=0.70$. These are the optimal values of the filter parameters determined by optimizing the filter for BER performance when CFO is $\Delta fT = 0.1875$, and $E_b/N_0=10\text{dB}$. In order to see the effect of pulse shaping on BER performance, BER vs E_b/N_0 plots for 1REC and 1RC shaped signals are shown in Figure 3-12. IF filters have been optimized separately for both signals. We can observe that

changing the pulse from 1REC to 1RC (see Table 2-1) improves BER about 0.8dB. These improvements can be achieved because 1RC pulse shaped signals are less affected by ISI than 1REC pulsed signals due to their smooth phase variations at symbol transitions.

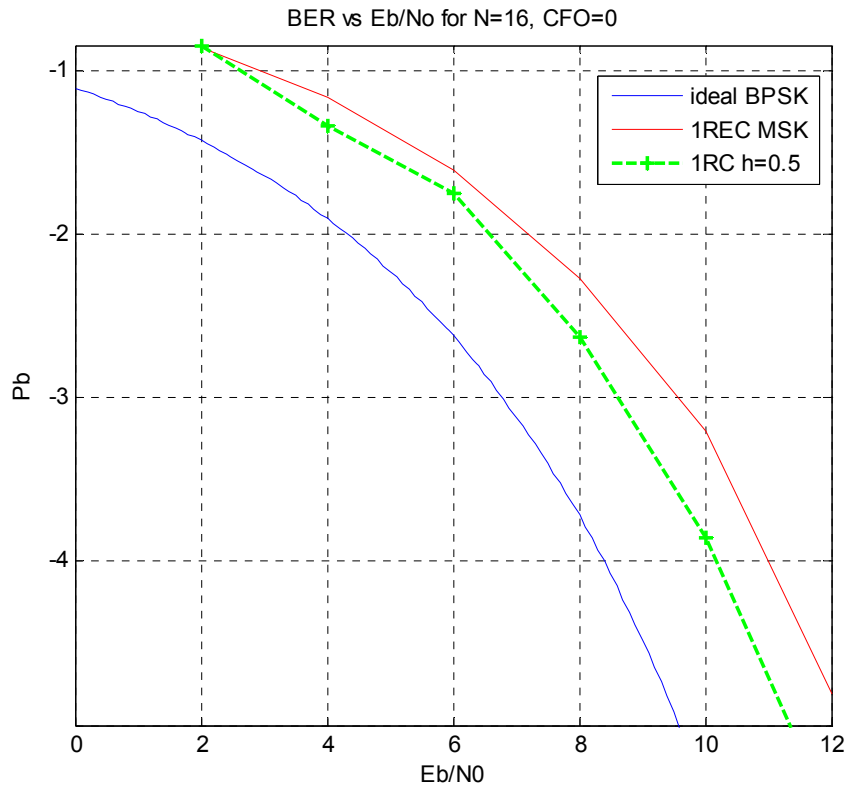


Figure 3-12 BER versus E_b/N_0 plot comparison of RC, REC and BPSK.

In order to see how BER performance of the MCM demodulator behaves under CFO, BER vs E_b/N_0 plots for RC pulse MSK-type signal with different CFO values are generated taking $N=16$. The filter parameters are determined by optimizing the filter for BER performance when CFO is $\Delta f T = 0.1875$, and this filter is used for all CFO values. As seen in Figure 3-13, CFO values above 15% of symbol frequency cause BER performance to degrade.

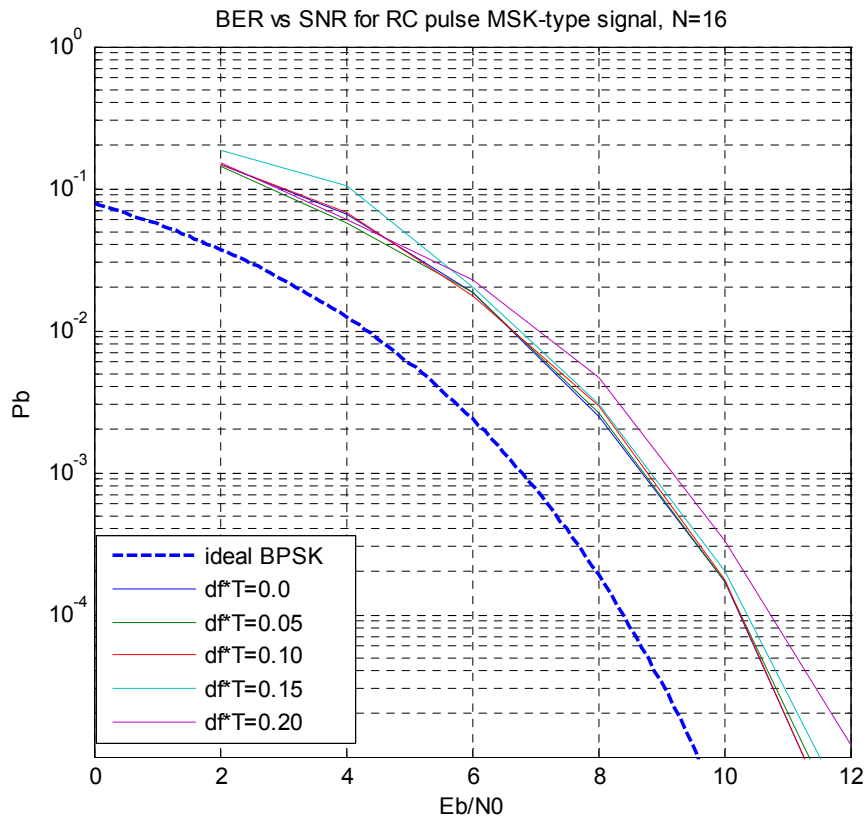


Figure 3-13 BER versus E_b/N_0 plot comparison of RC with CFO.

In addition, BER performances of MSK and RC pulsed MSK-type signals are compared with BER performance of DPSK signals. BER expression of DPSK is derived in [4]

$$P_b = \frac{1}{2} \exp\left\{-\frac{\varepsilon_b}{N_0}\right\} \quad (3.62)$$

Examining Figure 3-14, we note that BER performance of RC pulsed signal is closer to the performance of ideal DPSK than performance of MSK signal.

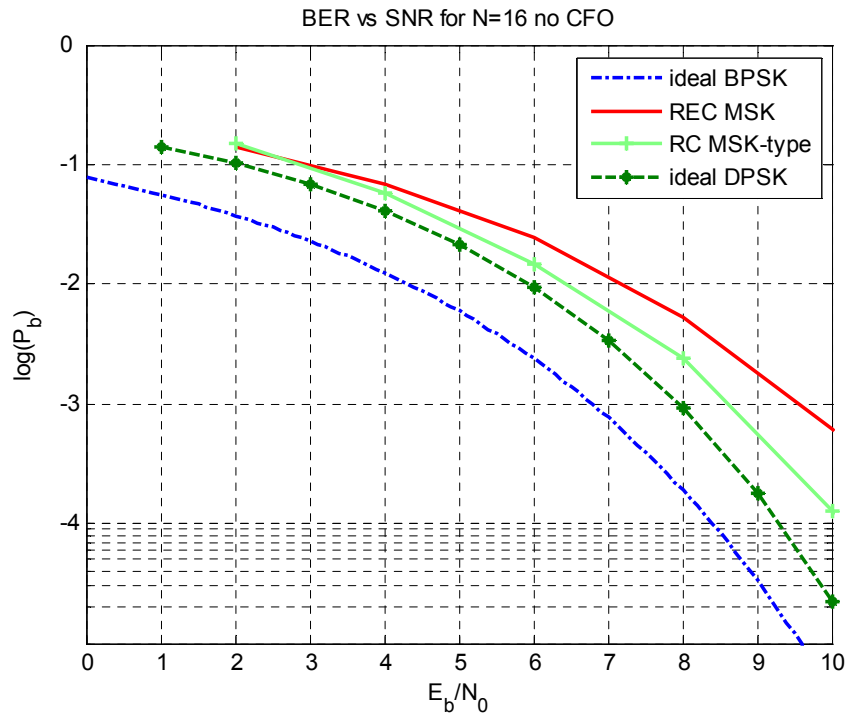


Figure 3-14 BER versus E_b/N_0 plot comparison with theoretical curves.

We also note that the performance curves are about 2 dB worse than the ideal BPSK performance. The difference is attributed to 1) noncoherent detection 2) degradation of the signal by the IF filter.

Using the MCM algorithm, CFO estimation is also performed in the absence of symbol timing delay with $L=64$, $N=16$, $E_b/N_0=6$ dB and 20dB (see Figure 3-15). At $E_b/N_0=6$ dB estimated CFO values deviate from actual CFO values. Whereas estimated CFO values are very close to the actual values at $E_b/N_0=20$ dB.

At $E_b/N_0=10$ dB, a similar simulation is carried out to compare the MCM and modified MCM estimators with $D=2$. As seen in Figure 3-16, there is no significant deviation from actual values for $\Delta fT \in (-0.20, 0.20)$.

Moreover, BER performance of the modified MCM algorithm with $D=1$ for different CFO values is simulated at $E_b/N_0=10$ dB and 12dB. The BER versus CFO plot is shown in Figure 3-17. For $|\Delta fT| < 0.22$, we can obtain the same performance as the case when there is no CFO.

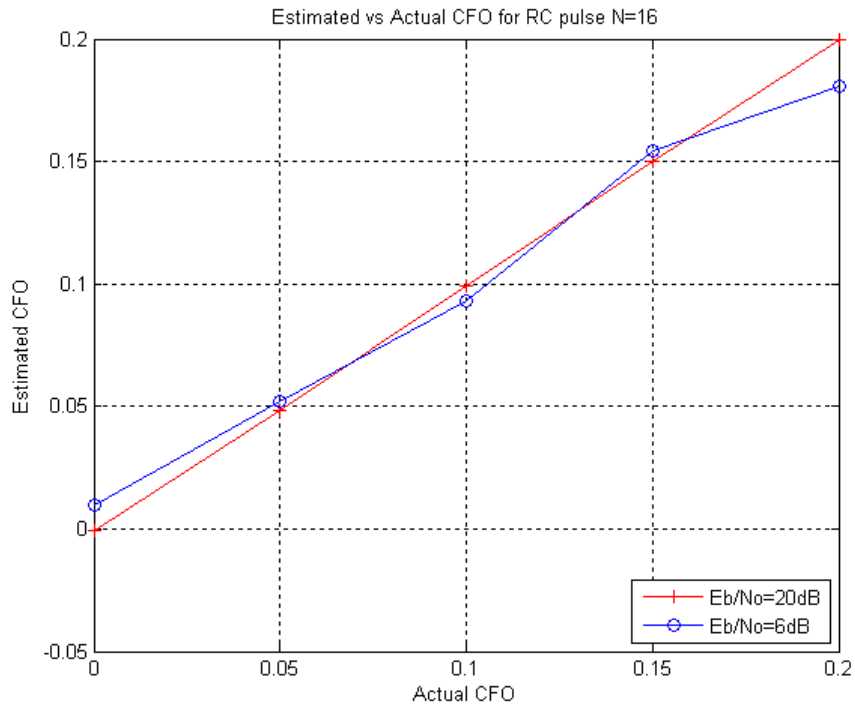


Figure 3-15 Estimated versus Actual CFO for RC pulse with N=16, L=64.

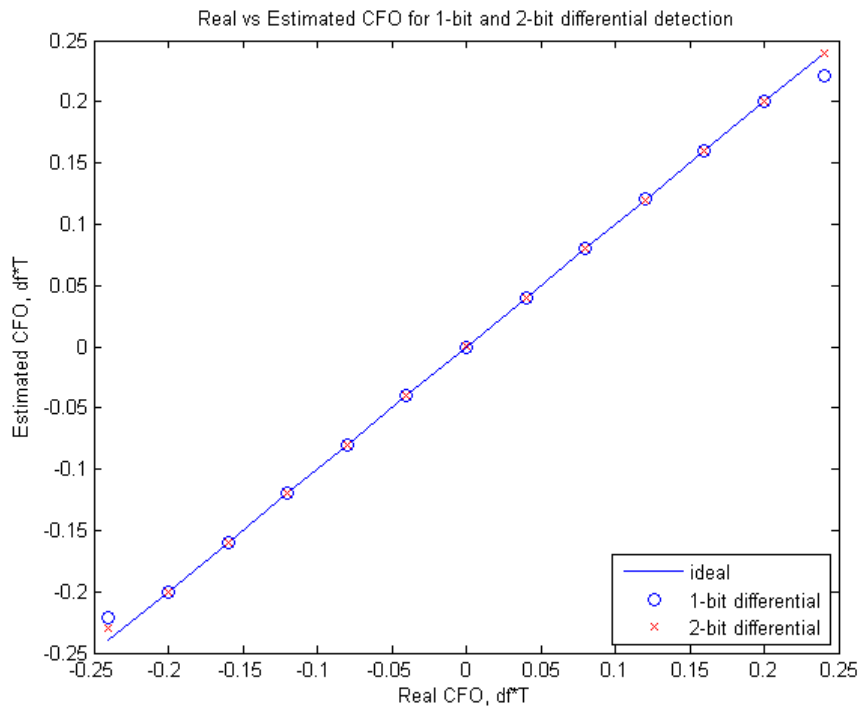


Figure 3-16 Actual versus Estimated CFO for modified MCM with D=1 and D=2 at $E_b/N_0=10\text{dB}$.

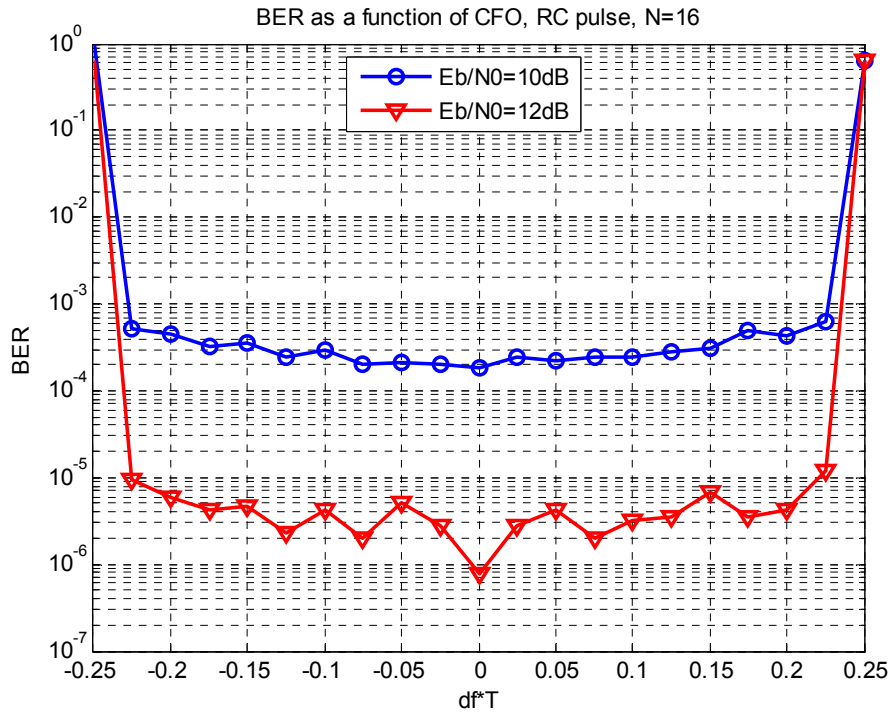


Figure 3-17 BER vs CFO for modified MCM with D=1.

Standard deviation of 1-bit, 2-bit & 4-bit diff CFO estimates, N=16 RC pulse MSK, $E_b/N_0=10\text{dB}$

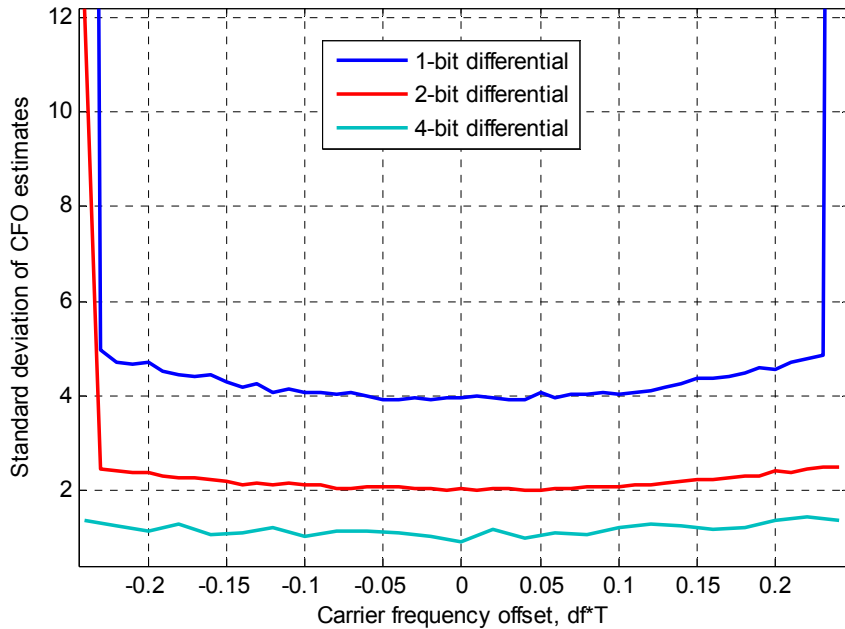


Figure 3-18 Standard deviation of CFO estimates versus different CFO values for modified MCM with D=1, 2 and 4.

In Figure 3-18, standard deviation of CFO estimates obtained from the modified MCM algorithm with $D=1, 2,$ and 4 are illustrated for the simulation at $E_b/N_0=10\text{dB}$ $N=16,$ $L=64$. Note that, standard deviation of the estimates does not change significantly for $|\Delta f T| < 0.23$. It is also observed that standard deviation of estimates is halved while doubling the number of symbols for phase difference.

Standard deviation of CFO estimates as a function of E_b/N_0 obtained from the modified MCM algorithm with $D=\{1, 2, 4, 8, 16, 32\}$ are compared by the square root of MCRB in Figure 3-19. The CFO ambiguity is removed by using the algorithm shown in Figure 3-5 for $D=2$. In order to remove ambiguity for $D=4$, the CFO estimation found using 2-lag 2-AC is employed in an ambiguity elimination process similar to the algorithm shown in Figure 3-5. We have not applied the ambiguity elimination algorithm for $D=\{8, 16, 32\}$, because computational complexity is higher for larger D values. Actually, we do not need to remove ambiguity to examine only the standard deviation of the CFO estimates. Note that, in low SNR region the ambiguity elimination process does not work well, since the ambiguity elimination process is based on the estimation with $D=1$ which has very high standard deviation at low SNR region. We can observe that standard deviation of CFO approaches to the lower bound, as D increases. However, the complexity to remove the ambiguity gets higher. We obtain significant improvements by doubling D value up to $D=16$. When D is 32 , phase differences during the interval of first 32 symbols are not taken into account. Thus, we cannot get an important improvement by changing $D=16$ to $D=32$. For $D=32$, the lower bound can almost be attained.

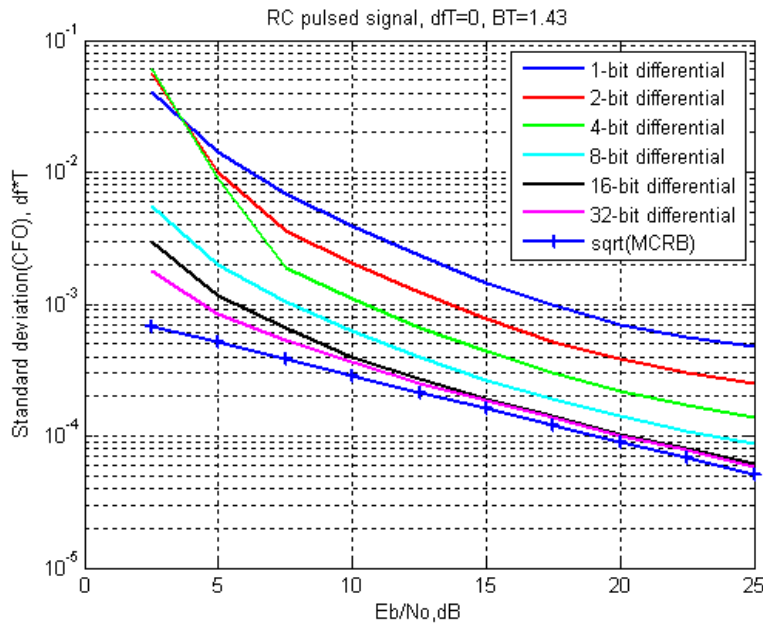


Figure 3-19 Standard deviation of CFO estimates versus E_b/N_0 for different D values.

3.5.3.2 Modified MCM Estimation for Quaternary CPM

In these simulations, a low-pass RC filter with a roll-off factor of $\beta=0.25$ and a bandwidth of $BT=2$ is used. These are the optimal values of the filter parameters determined by optimizing the filter for CFO mean square error (MSE).

We have extended the MCM algorithm to RC pulsed quaternary CPM signals with $h=0.25$.

In the case of no CFO at the input, mean and standard deviation of CFO estimates versus E_s/N_0 are plotted for $D=\{1, 2, 4\}$ in Figure 3-20 and Figure 3-21. Examining Figure 3-20, the bias on the estimates is seen to be quite low even at low SNR values. However, the standard deviations of the estimates at low SNR are not satisfactory. Above 15dB, satisfactory values of standard deviation may be obtained especially for $D=4$ compared to the lower bound. Employing phase differences during longer intervals (i.e. higher D values) in the algorithm, improves the performance of the estimator. In addition, we note that standard deviation

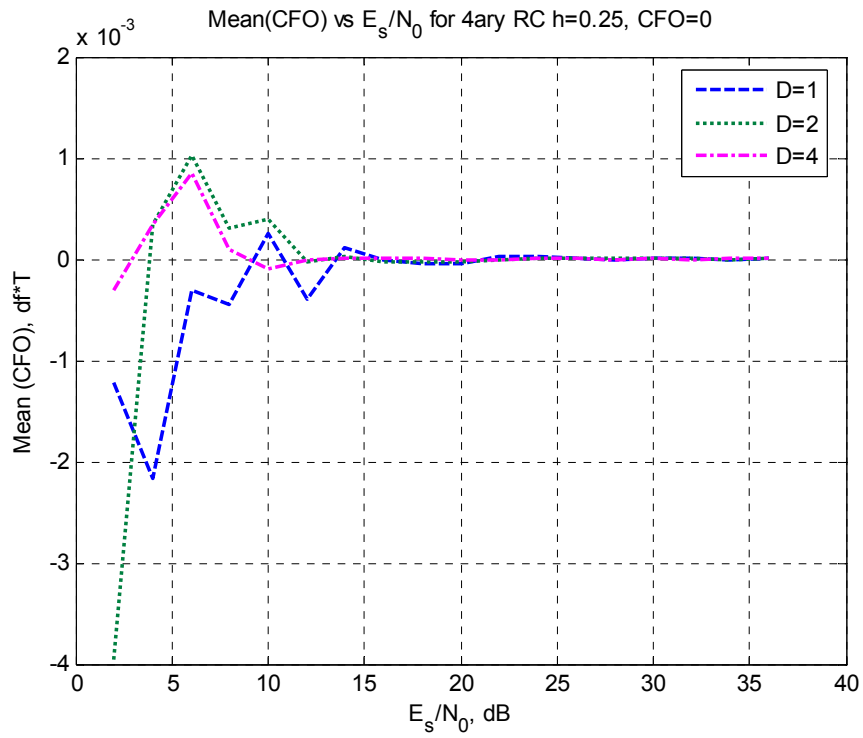


Figure 3-20 Mean of CFO estimates versus E_s/N_0 for CFO=0.

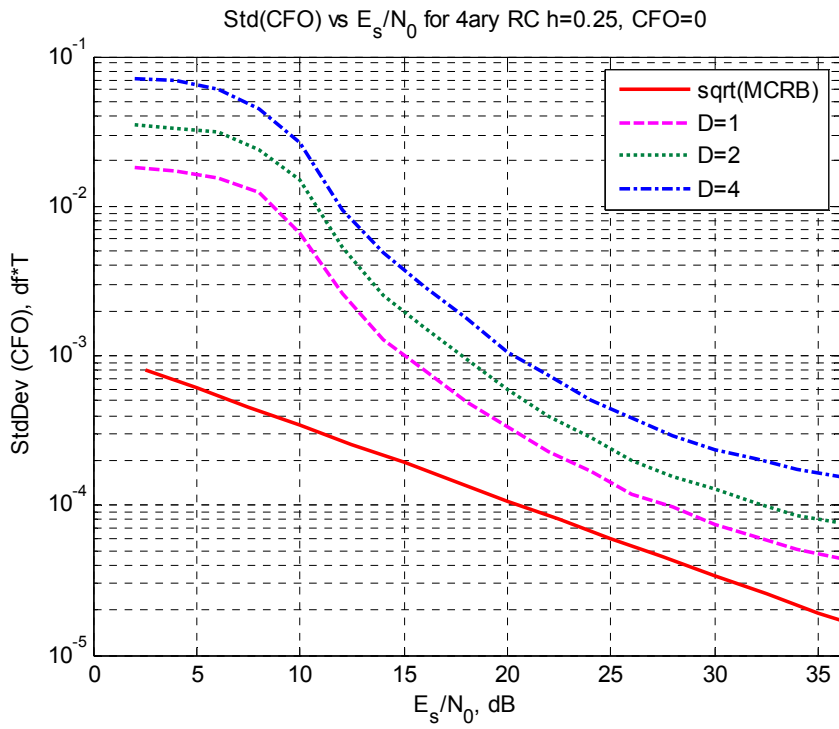


Figure 3-21 Standard deviation of CFO estimates versus E_s/N_0 for CFO=0.

curves start to saturate above 34dB SNR. That is, slopes of the curves gets lower as SNR increases in this region. This can be attributed to the IF filter since standard deviation is observed to be nonzero for very high SNR if IF filter is used, whereas almost zero standard deviation can be observed without using IF filter.

Mean and standard deviation of the CFO estimates are illustrated in Figure 3-22 – Figure 3-25 to investigate the performance of the modified MCM for different CFO values (5% and 10% of symbol frequency). For both 5% and 10% CFO values, the standard deviation of the estimates gets closer to the lower bound above 15dB SNR. The mean of the estimates approaches to the actual CFO values at E_s/N_0 values higher than 12dB. In addition, we note that the bias on the CFO estimates diminishes significantly by increasing D.

In Section 3.2.2, it was noted that we can estimate the CFO in the interval $(-\pi/4, \pi/4]$ using the modified MCM algorithm for quaternary signals with $h=0.25$. The interval $(-\pi/4, \pi/4]$ corresponds to $-0.125 < \Delta fT \leq 0.125$. In fact, we find that $\Delta fT + 0.25 * K$ where K is an integer, represents the ambiguity. In Figure 3-26, the mean of the CFO estimates versus SNR is plotted in the case $\Delta fT = 0.15$. We observe that, the mean of the CFO estimates approaches to -0.10 as SNR ascends. Hence, the experimental results support the anticipation that we find $\Delta fT + 0.25 * K$ in the interval $(-0.125, 0.125]$. We have CFO $\Delta fT = 0.15$, and we find $\Delta fT = -0.10$, with $K=-1$.

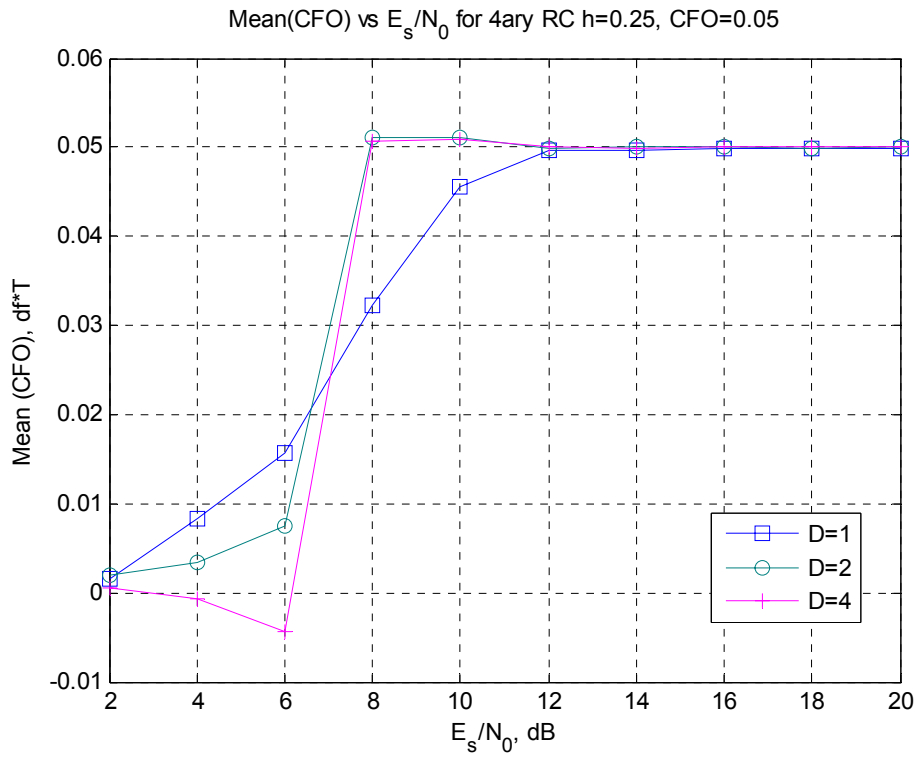


Figure 3-22 Mean of CFO estimates versus E_s/N_0 for CFO=0.05.

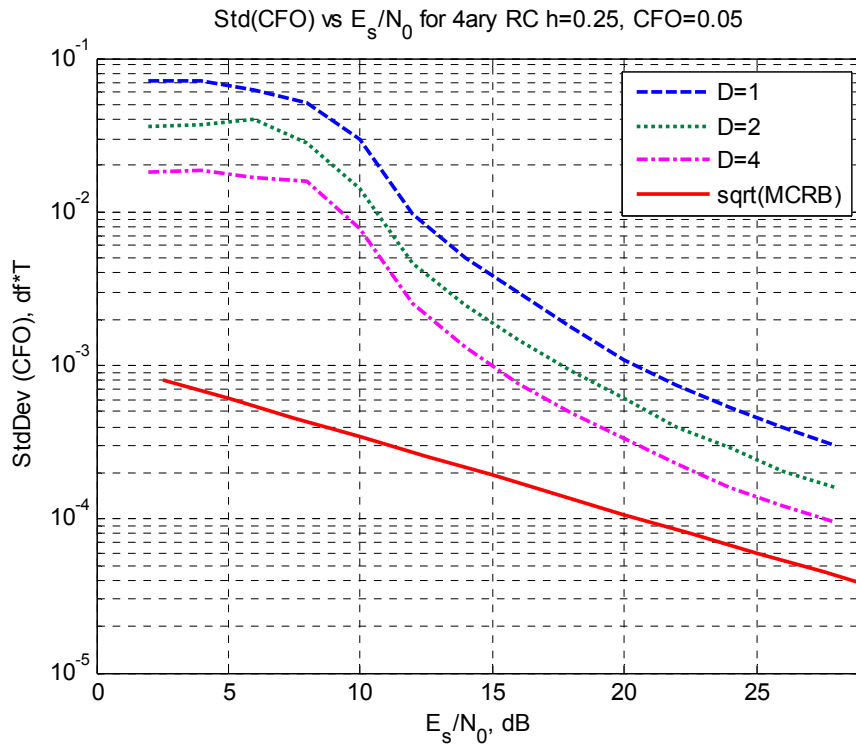


Figure 3-23 Standard deviation of CFO estimates versus E_s/N_0 for CFO=0.05.

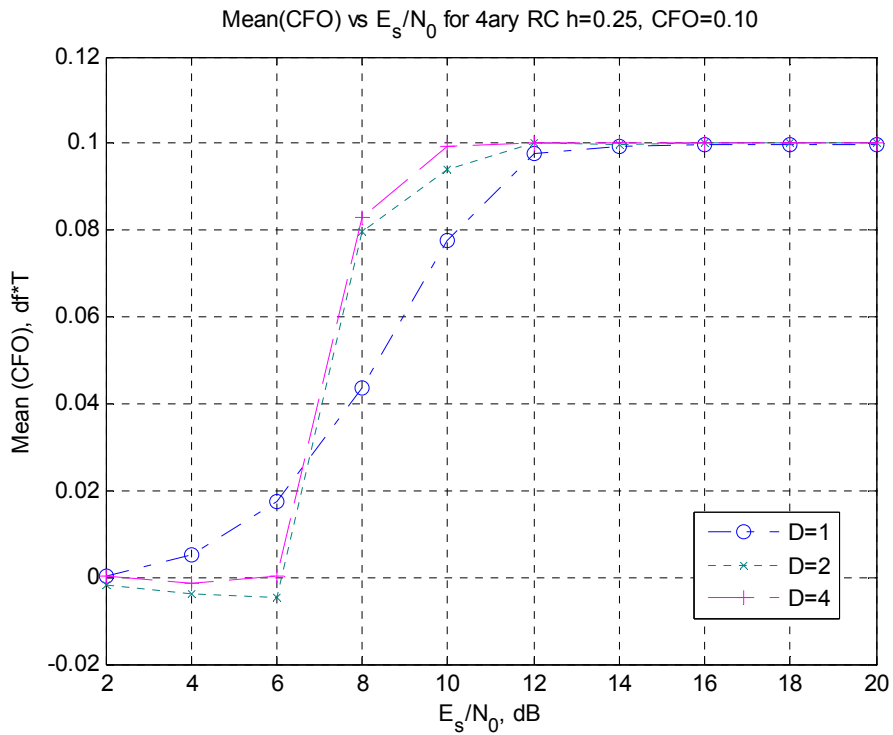


Figure 3-24 Mean of CFO estimates versus E_s/N_0 for CFO=0.10.

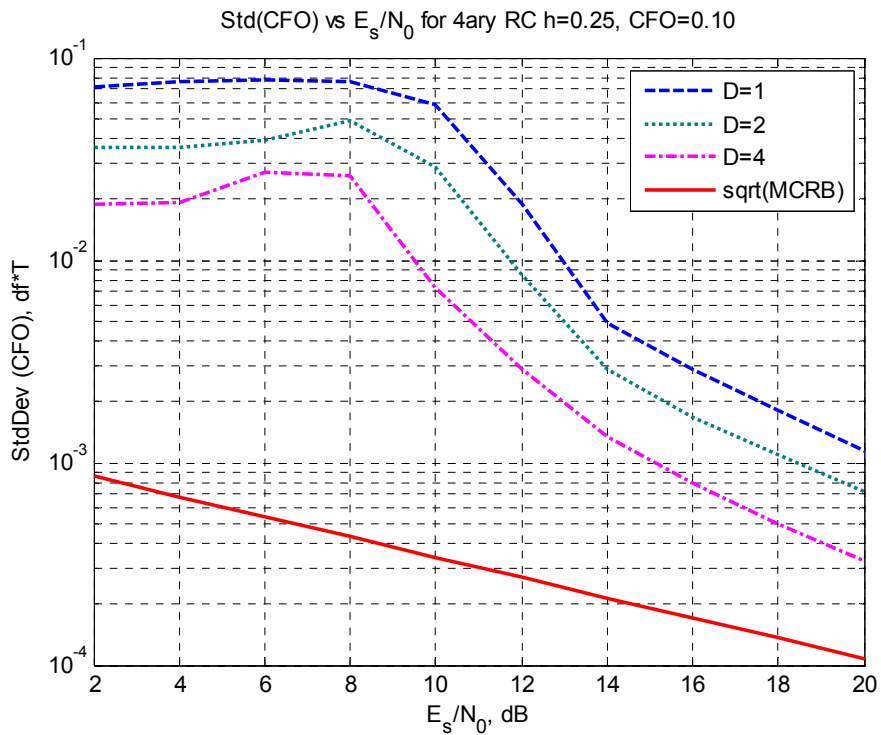


Figure 3-25 Standard deviation of CFO estimates versus E_s/N_0 for CFO=0.10.

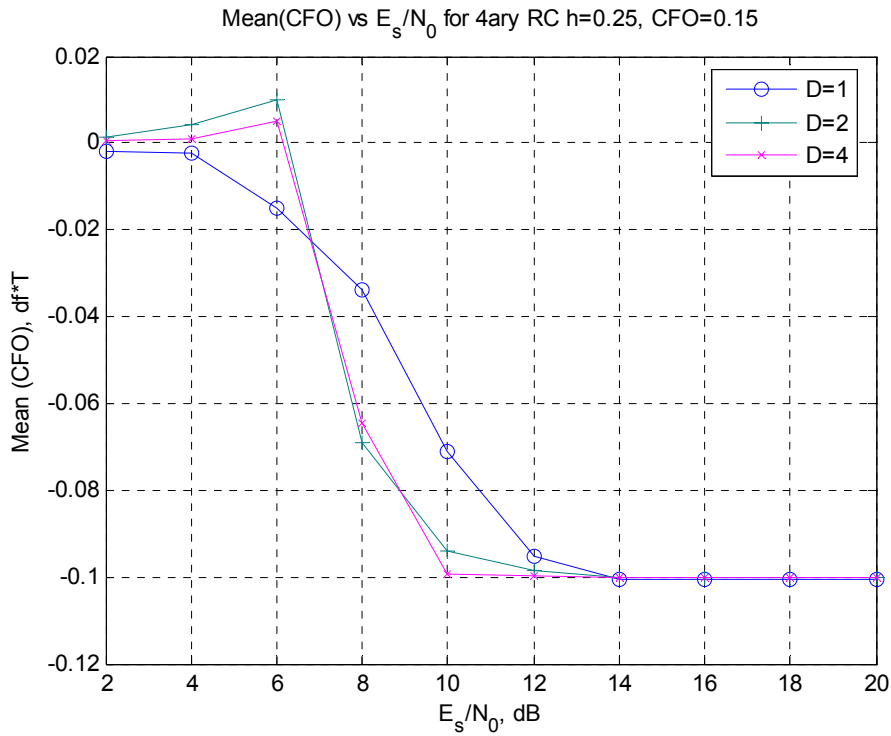


Figure 3-26 Mean of CFO estimates versus E_s/N_0 for CFO=0.15.

3.5.3.3 Modified MCM Estimation for Partial Response Binary CPM with $h=1/2$, $L=2$

In the simulations of this part, low-pass RC filter with a roll-off factor of $\beta=0.75$ and a bandwidth of $BT=1.61$ is used. These are the optimal values of the filter parameters determined by optimizing the filter for CFO MSE.

We have modified the MCM algorithm for partial response 2RC pulsed CPM signals with $h=0.5$.

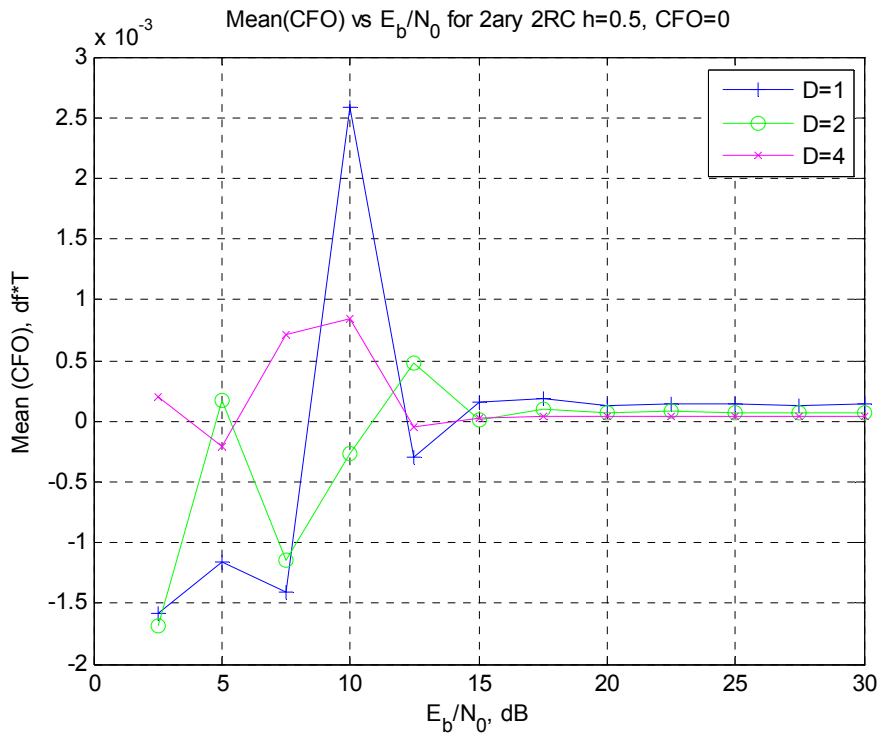


Figure 3-27 Mean of CFO estimates versus E_b/N_0 for CFO=0.

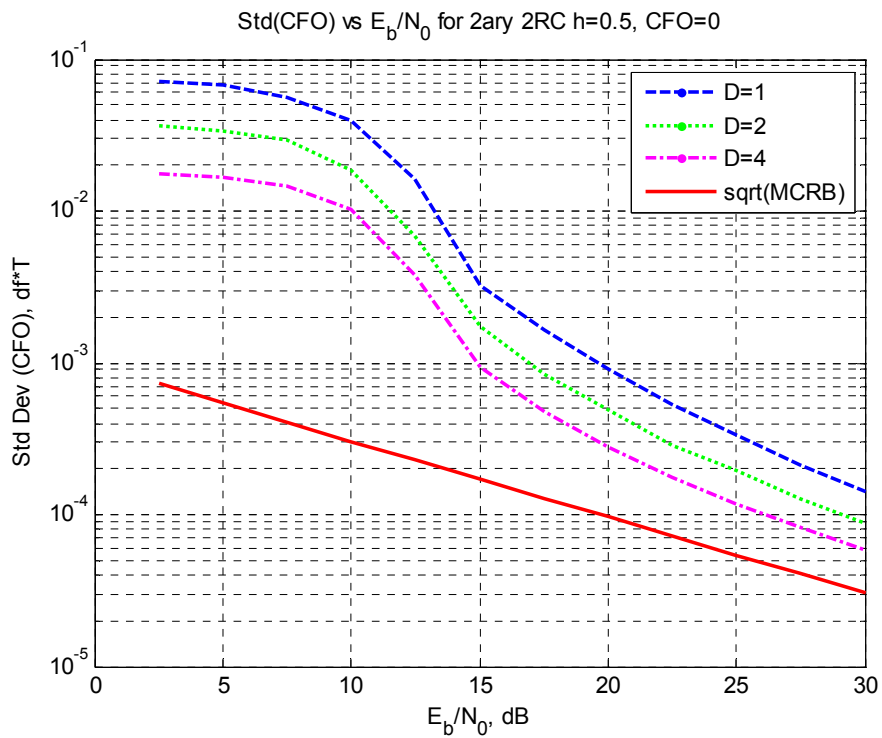


Figure 3-28 Standard deviation of CFO estimates versus E_b/N_0 for CFO=0.

In the case there is no CFO, mean of CFO estimates and standard deviation of estimates versus E_b/N_0 are plotted for $D=\{1, 2, 4\}$ in Figure 3-27 and Figure 3-28. Figure 3-27 illustrates that the bias on the estimates is quite low even at low SNR values. However, we do not have acceptable standard deviations of the estimates at low SNR. We note that standard deviation of the CFO estimates approaches to the lower bound, especially for $D=4$ above 15dB. Exploiting higher D values in the algorithm provides better performance of the estimator.

Mean and standard deviation of the estimates are illustrated in Figure 3-29 – Figure 3-32 in order to examine the performance of the modified MCM for different CFO values (5% and 10% of symbol frequency). The standard deviation of the estimates approaches to the lower bound above 15dB SNR for both 5%

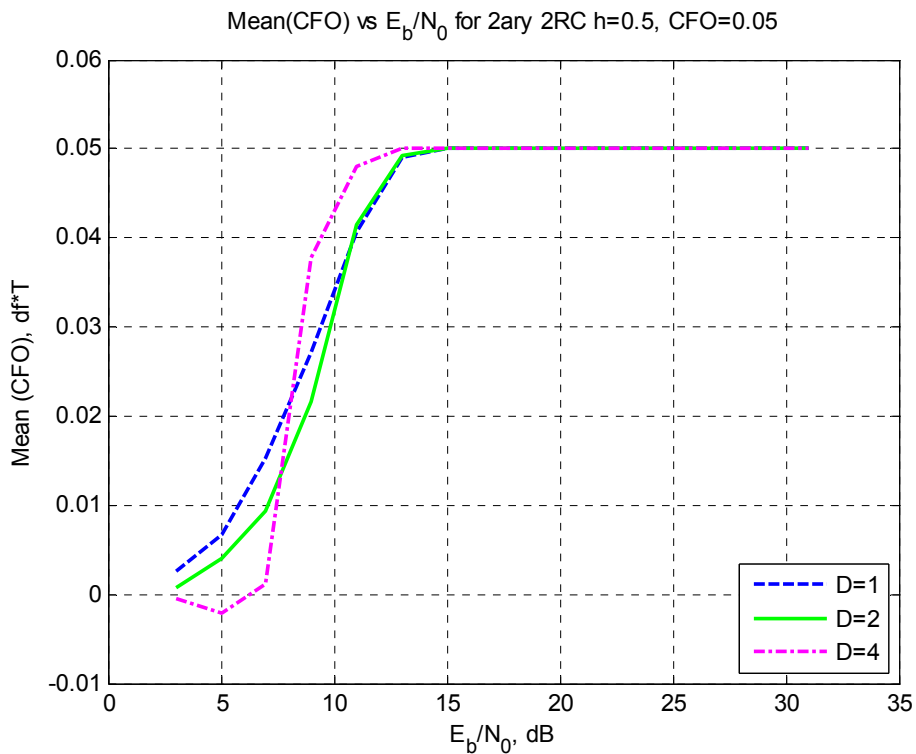


Figure 3-29 Mean of CFO estimates versus E_b/N_0 for CFO=0.05

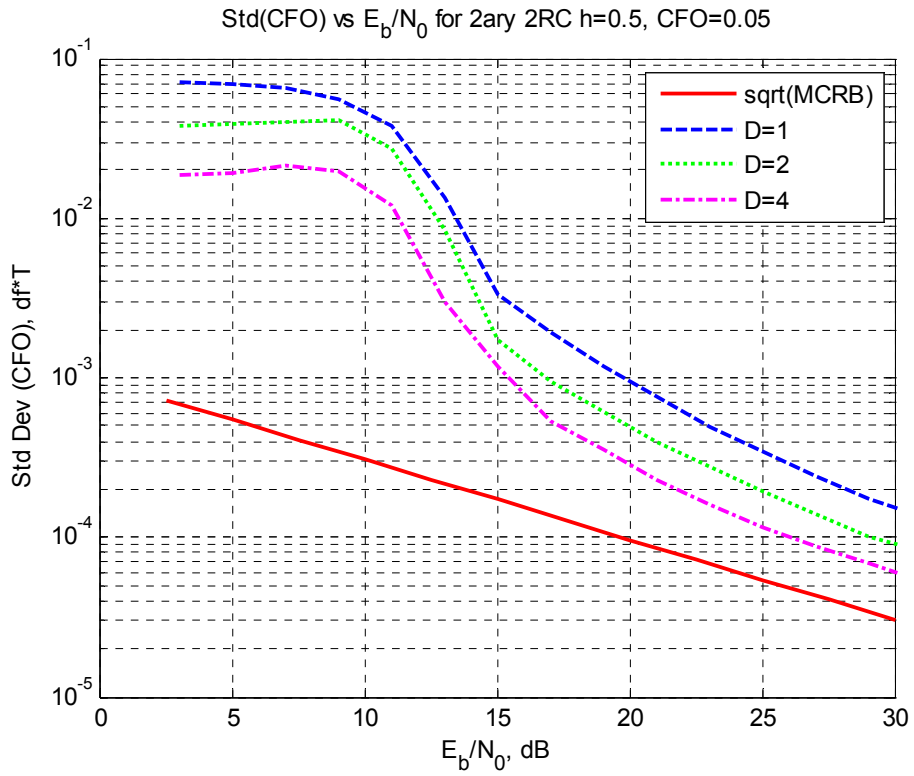


Figure 3-30 Standard deviation of CFO estimates versus E_b/N_0 for CFO=0.05.

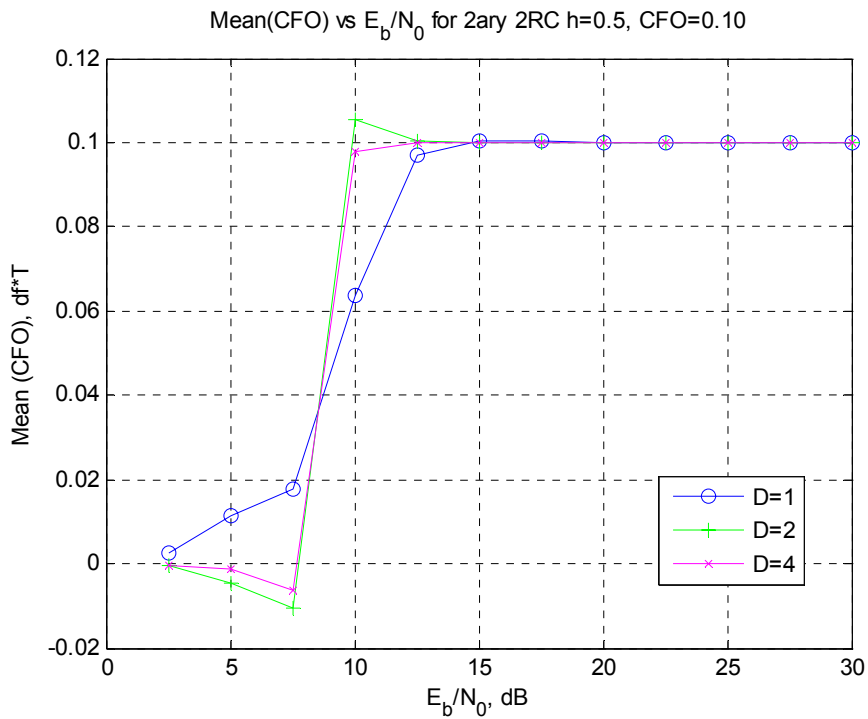


Figure 3-31 Mean of CFO estimates versus E_b/N_0 for CFO=0.10.

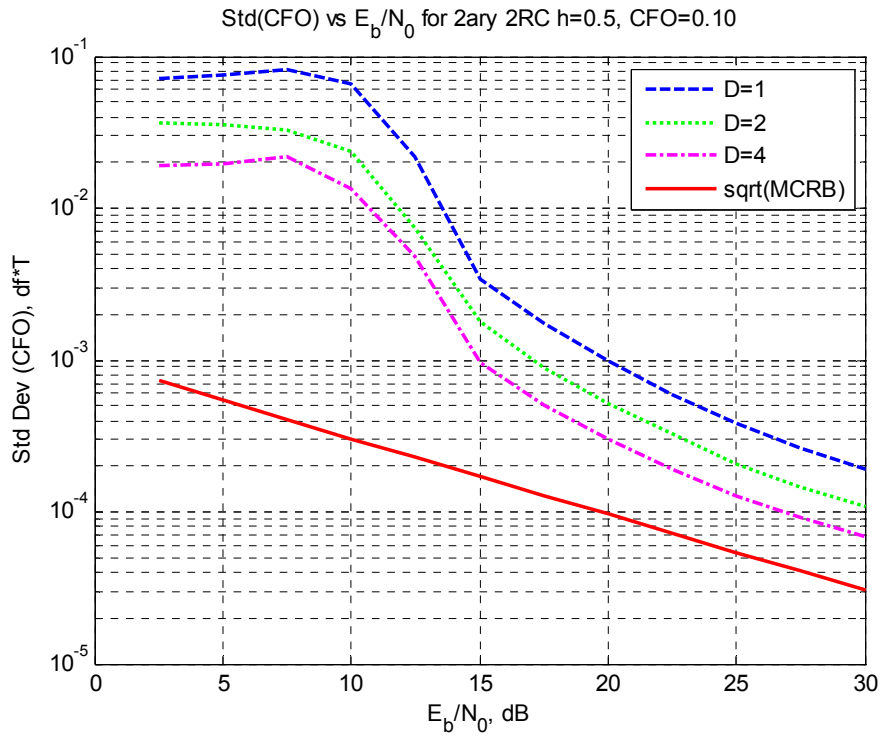


Figure 3-32 Standard deviation of CFO estimates versus E_b/N_0 for CFO=0.10.

and 10% CFO values. At values higher than $E_b/N_0 = 12\text{dB}$, the mean of the estimates comes nearer to the actual CFO values. In addition, we note that using $D=4$ in the algorithm reduces the bias on the CFO estimates significantly when E_b/N_0 is between 10dB-15dB.

In Section 3.2.3, it was stated that we can estimate the CFO in the interval $(-\pi/4, \pi/4]$ using the modified MCM algorithm for binary partial signals with pulse 2RC and $h=0.5$. The interval $(-\pi/4, \pi/4]$ corresponds to $-0.125 < \Delta fT \leq 0.125$. Actually, we see that $\Delta fT + 0.25 * K$ where K is an integer, presents the ambiguity. In Figure 3-33, mean of the CFO estimates versus SNR is plotted in the case $\Delta fT = 0.15$. It is observed that mean of the CFO estimates goes to -0.10 as SNR increases, which means the integer K equals to -1. Hence, the statement is supported with the experimental results.

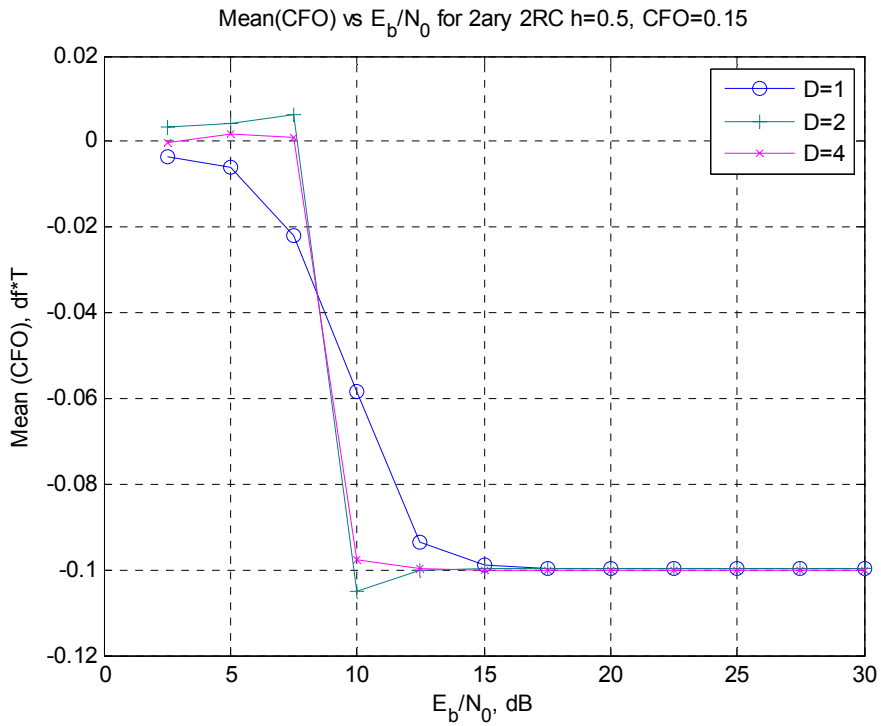


Figure 3-33 Mean of CFO estimates versus E_b/N_0 for CFO=0.15.

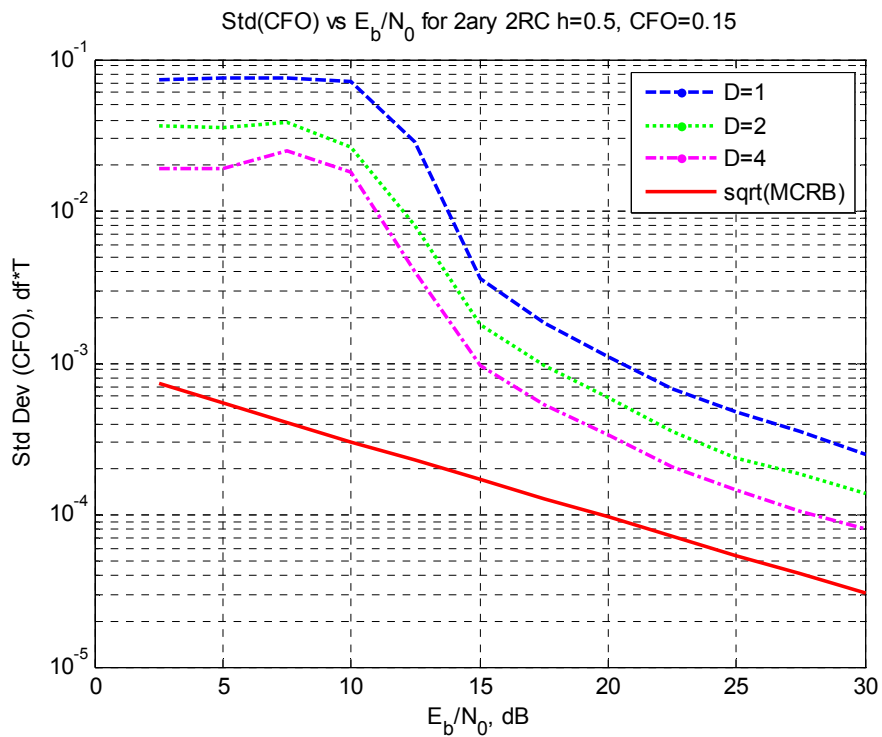


Figure 3-34 Standard deviation of CFO estimates versus E_b/N_0 for CFO=0.15.

In the absence of noise, symbol-phase differences can be represented as

$$\Delta\phi_k = \begin{cases} \frac{\pi}{2} + \Delta\omega T, & \text{if } (I_{k-1}, I_k) = (+1, +1) \\ -\frac{\pi}{2} + \Delta\omega T, & \text{if } (I_{k-1}, I_k) = (-1, -1) \\ 0, & \text{if } (I_{k-1}, I_k) = (+1, -1) \text{ or } (-1, +1) \end{cases} \quad (3.63)$$

where I_k is the k^{th} information symbol.

$$\frac{1}{L} \sum_{k=1}^L \Delta\phi_k = \Delta\omega T \quad (3.64)$$

If all consecutive symbols are distributed fairly, average value of the symbol phase differences equals to the CFO value.

Using this fact, CFO estimation of partial response signals can be carried out by using equations (3.24) - (3.27): namely, the 2-AC function is used. The standard deviation of the CFO estimates obtained in this way is compared in Figure 3-35 with the standard deviation of the CFO estimates obtained using the method described in section 3.2.3 (using the 4-AC function). Figure 3-35 shows that estimates obtained using the 2-AC function have lower standard deviation compared to the estimates obtained by using the 4-AC function when E_b/N_0 is less than 15dB. However, the standard deviation of the estimates obtained by using the 2-AC function does not get closer to the lower bound above 15dB SNR. This is due to the fact that fairly distribution of symbols is not achieved perfectly for finite values of L , while the estimation technique depends on the assumption of fairly distribution of consecutive symbols.

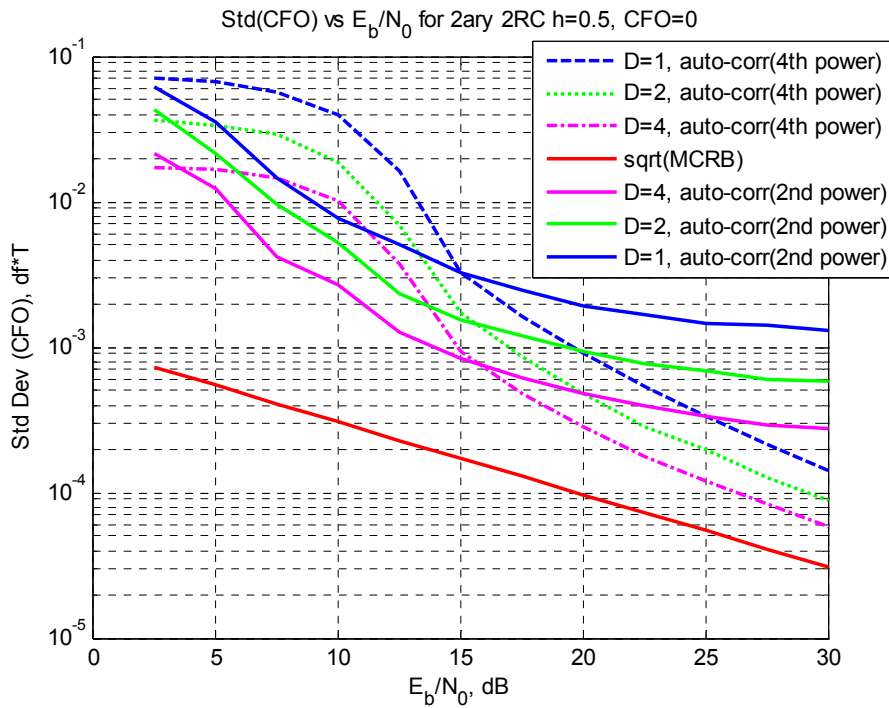


Figure 3-35 Standard deviation of CFO estimates versus E_b/N_0 for partial response CPM signals with CFO=0.

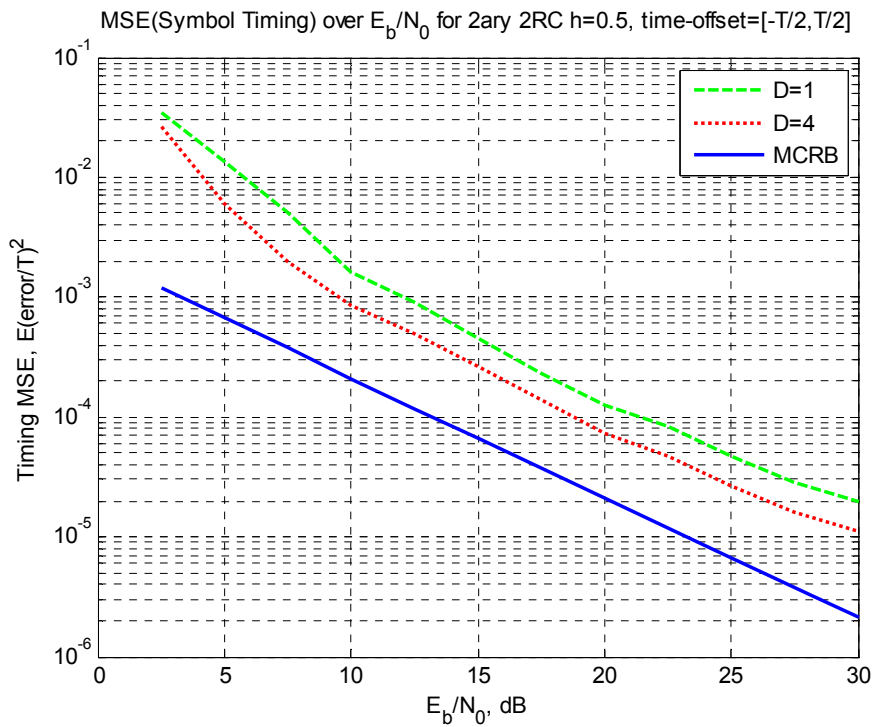


Figure 3-36 MSE of timing estimates for partial response binary CPM signals.

MSE of symbol timing-estimates are also shown in Figure 3-36, in the case symbol timing offset is randomly distributed in $[-T/2, T/2]$. Equation (3.24) is used in equation (3.36) to estimate the symbol timing offset. As the parameter D in the algorithm grows, MSE performance of the estimator approaches more to the MCRB.

3.5.3.4 M&M Estimation Method for Full Response Binary CPM

Mengali and Morelli (M&M) [13] proposed to use $\{1, 2, \dots, m\}$ -lag 2-AC functions in order to estimate CFO and symbol timing jointly for MSK-type signals. Estimation of 2-AC functions and CFO is given in equations (3.11) and (3.12), respectively.

We have investigated the M&M algorithm (see section 3.1.1.1) for binary 1RC pulsed MSK-type signals with $L=64$ and $N=16$ using an RC type IF filter with a roll-off factor $\beta=0.35$ and a bandwidth of $BT=1.62$. These are the optimal values of the filter parameters determined by optimizing the filter for CFO MSE. Mean of CFO estimates obtained by using the M&M estimator is illustrated in Figure 3-37 for $-0.25 < \Delta fT < 0.25$ and $E_b/N_0=10\text{dB}$. We observe that the estimator with $D=1$ (1-symbol phase differences are used) works properly in the interval $-0.25 < \Delta fT < 0.25$. For $D=4$, the interval in which the estimator works properly is narrower $-0.22 < \Delta fT < 0.22$.

In Figure 3-38, standard deviation of CFO estimates versus E_b/N_0 plot is shown for the M&M algorithm in the absence of CFO. Increasing D in the algorithm helps approach the lower bound.

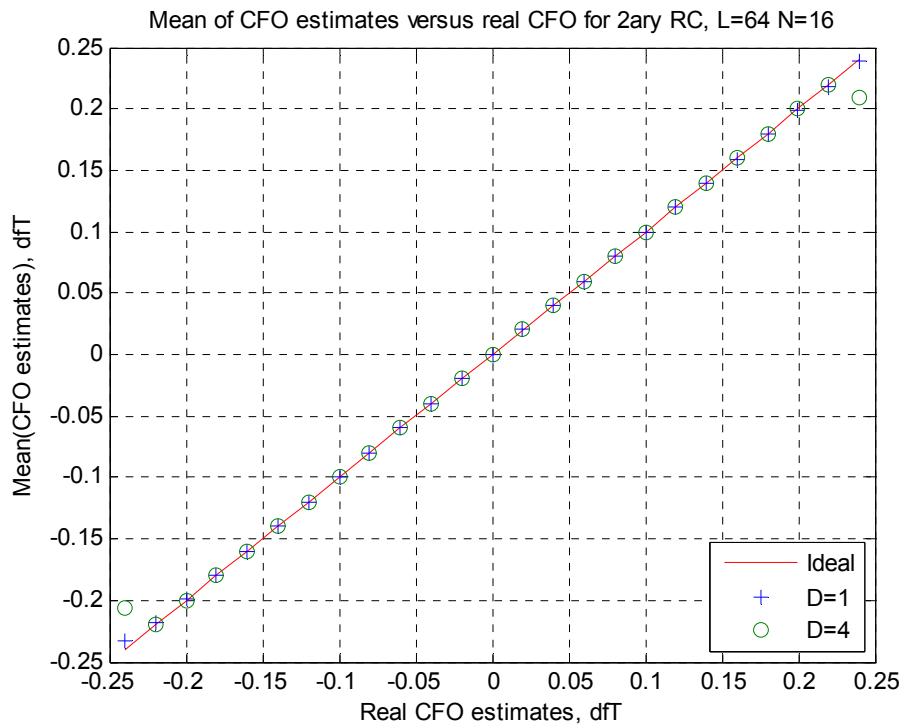


Figure 3-37 Mean of CFO estimates vs actual CFO for binary RC, h=0.5.

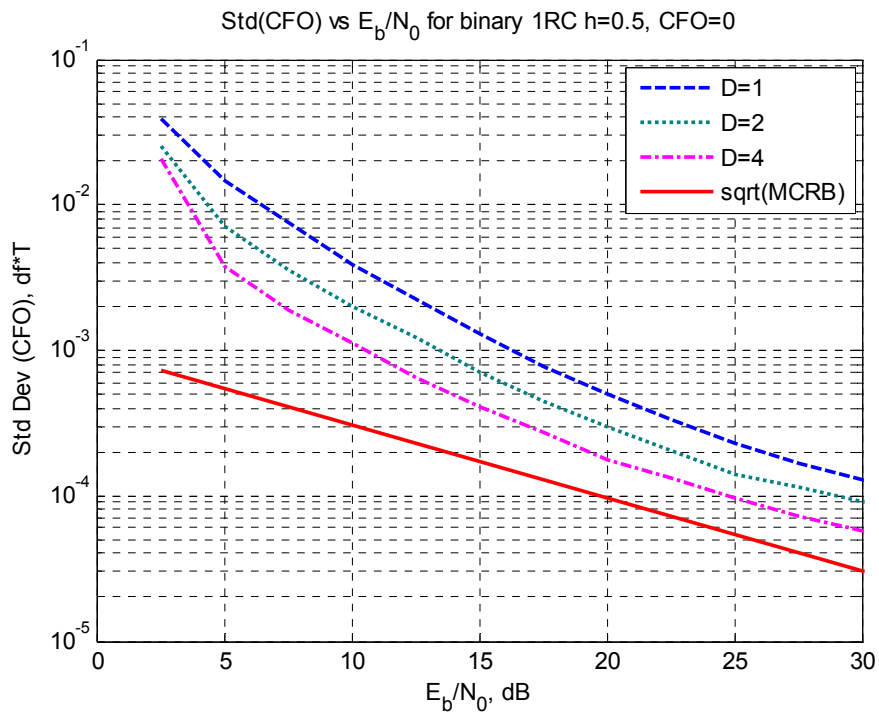


Figure 3-38 Standard deviation of CFO estimates versus E_b/N_0 for CFO=0.

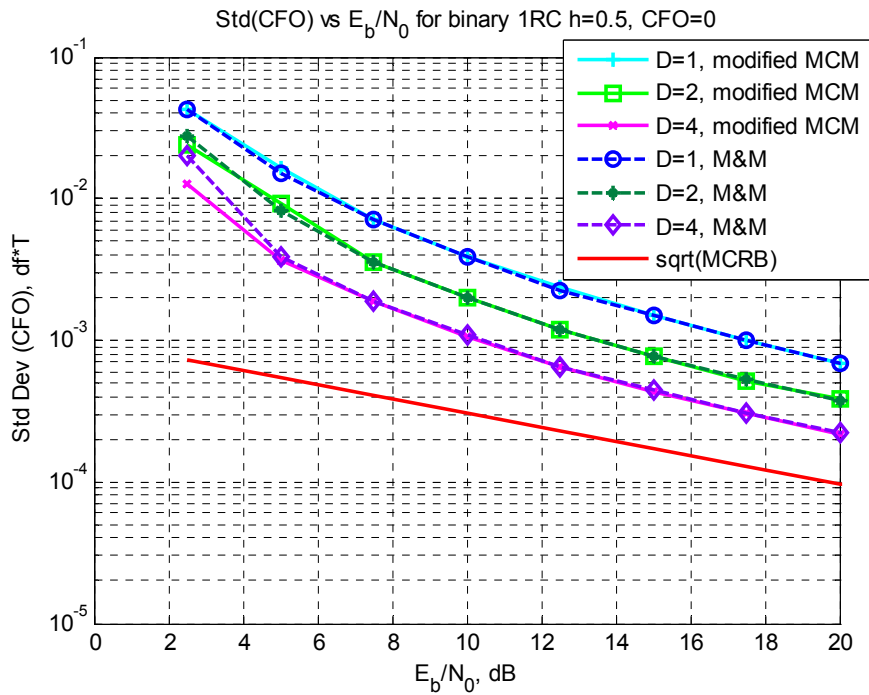


Figure 3-39 Comparison of the M&M and the modified MCM method for CFO=0.

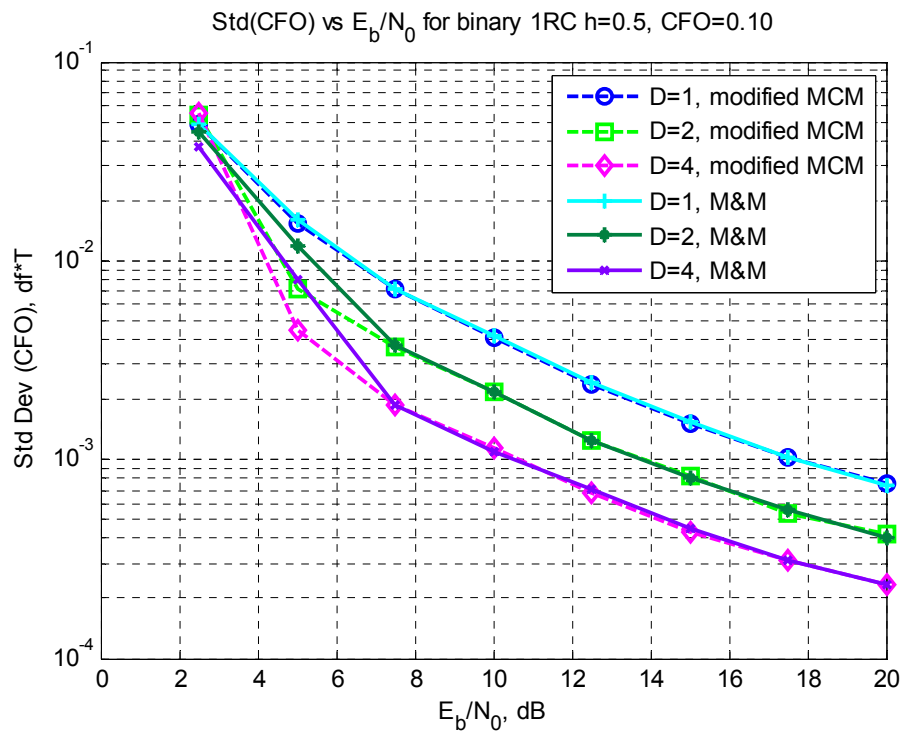


Figure 3-40 Comparison of the M&M and the modified MCM method for CFO=0.10.

The comparison of standard deviation of CFO estimates obtained by the M&M method versus the modified MCM method is shown in the absence of CFO in Figure 3-39. The figure shows that standard deviations of the CFO estimates obtained by both methods coincide for $E_b/N_0 \geq 5\text{dB}$. The difference at very low SNR region may be attributed to the different ambiguity elimination process of the estimation methods. In section 3.4, it has been shown that both methods would yield to the same result if there were no ambiguity. The figure verifies this statement, and shows that ambiguity elimination operation in the modified MCM method gives almost same results as the M&M estimation algorithm.

The comparison of both methods in the case when CFO is 10% is also shown in Figure 3-40. We observe that ambiguity elimination operation in the modified MCM method leads to lower standard deviation of CFO estimates at low SNR ($<7\text{dB}$) values.

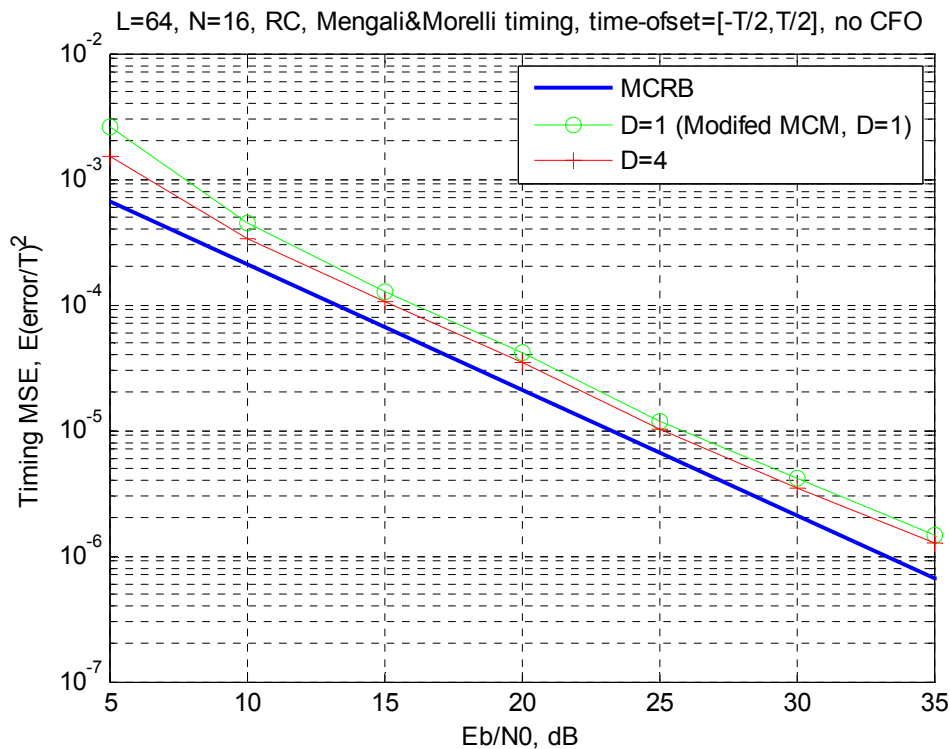


Figure 3-41 Mean square error of symbol timing estimates for binary RC signal.

Symbol timing estimation aspect of the M&M estimator has also been investigated for binary RC MSK-type signal with $L=64$, $N=16$, and with a low-pass filter optimized for minimum MSE (Mean square error) timing jitter. The filter has a bandwidth of $BT=1.61$ and a roll-off factor $\beta=0.30$. MSE of the symbol timing estimates versus E_b/N_0 is illustrated in Figure 3-41 while symbol timing offset is uniformly distributed in the interval $[-T/2, T/2]$. As the parameter D in the algorithm grows, MSE performance of the estimator moves nearer to the lower bound.

Moreover, the effect of the M&M symbol timing estimation method on BER performance of binary RC pulsed MSK-type signals is investigated. Symbol detection (conventional differential detection) is applied using the M&M estimation algorithm together with the decimation and frequency compensation process described in section 3.5.1. In the decimation process, estimated symbol timing offset is rounded to an integer multiple of sample time, and we assume ideal frame synchronization is provided. The difference between the symbol timing offsets estimated for $D=1$ and $D=4$ are negligible compared to the sampling period. Hence, the timing points selected for decimation are not expected to be much different for $D=1$ and $D=4$ after rounding timing-offset values.

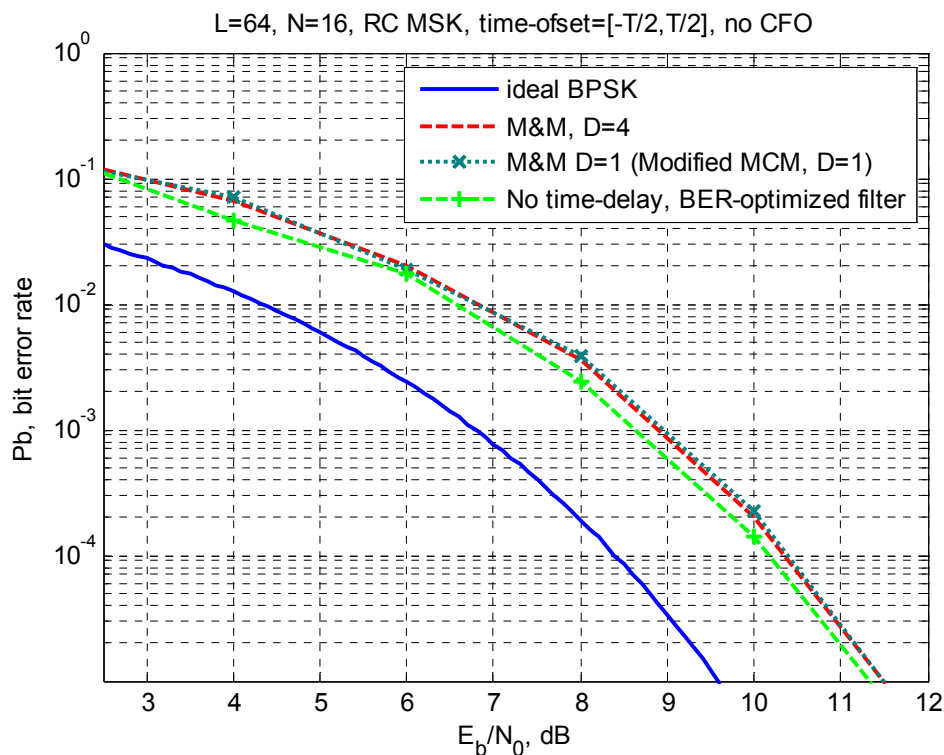


Figure 3-42 BER versus E_b/N_0 with uniformly distributed timing offset over $[-T/2, T/2]$.

Examining Figure 3-42, BER performances for $D=1$ and $D=4$ are almost the same in the case of uniformly distributed timing offset over $[-T/2, T/2]$ and zero CFO, as expected. In the figure, BER performance obtained in the absence of CFO using a low-pass filter optimized for BER performance is also displayed. There is about a 0.25dB difference between BER curves using a BER optimized filter and the timing MSE optimized filter.

3.5.3.5 Modified M&M Estimation Method for Quaternary CPM

In this part, we present simulations that are carried out with 4-ary RC signals with $h=0.25$ to investigate the performance of the modified M&M algorithm. The low-pass filter is an RC filter with a roll-off factor of $\beta=0.35$ and bandwidth of $BT=1.61$. These are the optimal values of the filter parameters determined by optimizing the filter for CFO MSE.

In Figure 3-43, mean of CFO estimates versus actual CFO values are plotted for symbol sequences with length $L=64$ and $L=128$ in the case $N=16$ and $E_s/N_0=10$ dB in order to see the effect of the observation length. It can be seen that the mean values of the estimates are very close to the actual values in the interval $\Delta fT < 0.075$ for $L=128$. The observation length is taken as $L=128$ in the simulations for quaternary signals. Mean values of the auto-correlation values are computed by using averaging filters with length equal to L , the whole block length. Averaging filters with higher length means average values can be computed more accurately. Figure 3-43 supports this statement.

Moreover, higher values of D causes poorer CFO estimates for $\Delta fT > 0.09$ as seen in the figure. Theoretically, we can estimate CFO values $-0.125 < \Delta fT < 0.125$ using the modified M&M method for quaternary CPM signals. Therefore, we expect that CFO estimates deviate from the actual value if $|\Delta fT|$ approaches to 0.125 because of the ambiguity problem. In addition, the

interval in which we can estimate CFO halves due to the ambiguity when we use $2K$ -symbol phase differences instead of K -symbol phase differences. These facts can explain why CFO estimates are poorer for higher values of D and closer values of $|\Delta f T|$ to 0.125 .

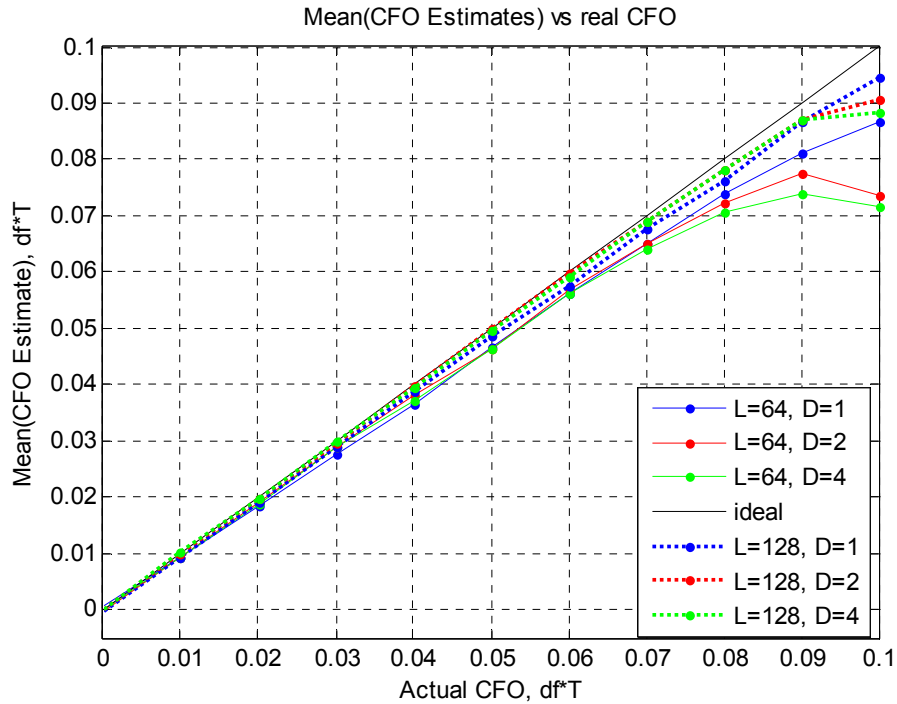


Figure 3-43 Mean value of CFO estimates for quaternary CPM signals.

In addition, standard deviations of CFO estimates versus SNR are plotted in Figure 3-44 for symbol sequences with length $L=64$ and $L=128$ in the case $N=16$ and zero CFO. We obtain lower standard deviation of estimates for larger lengths of L , as expected by lower bounds.

Standard deviation values of the estimates as a function of SNR are plotted in Figure 3-45 for $L=128$ and $N=16$. Above 15 dB SNR, standard deviation values closer to the lower limit can be obtained especially for $D=8$. Standard deviations can be lowered by increasing D in the modified M&M algorithm.

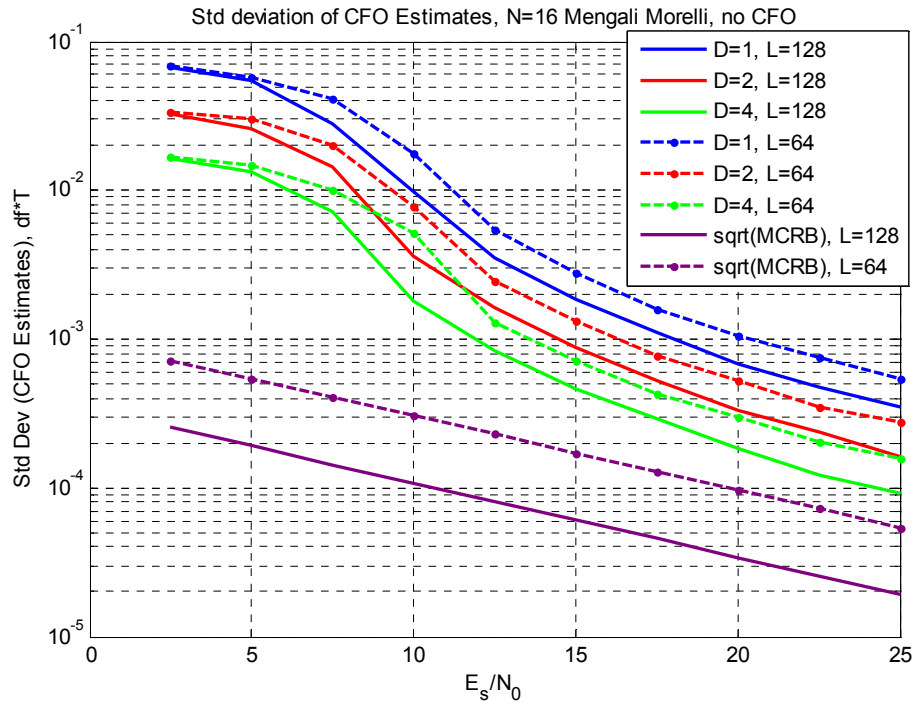


Figure 3-44 Standard deviation of CFO estimates for quaternary CPM signals.

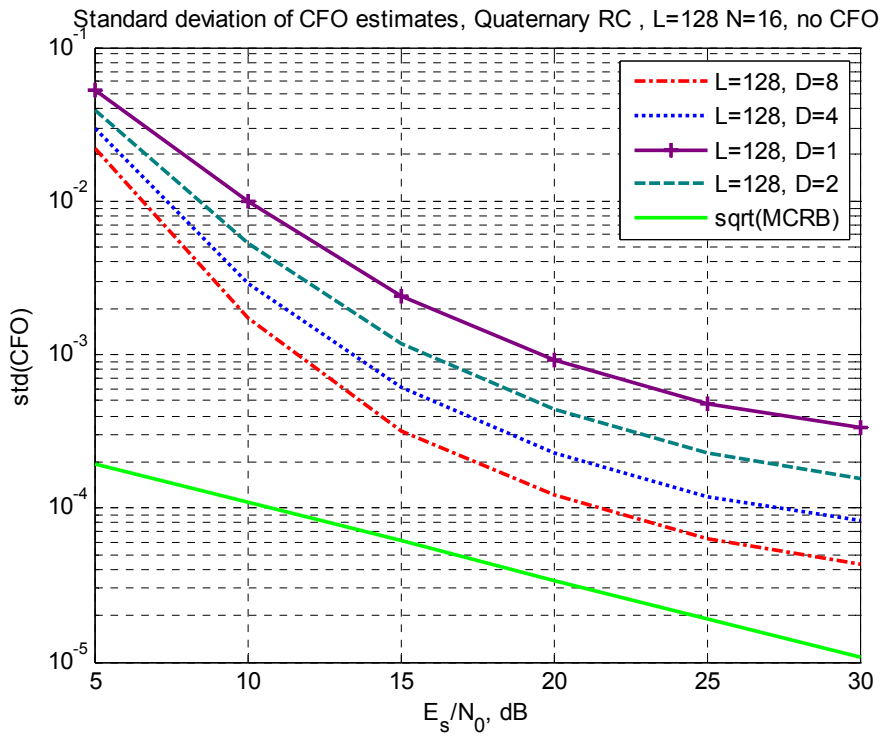


Figure 3-45 Standard deviation of CFO estimates versus E_s/N_0 for quaternary CPM signals with CFO=0.

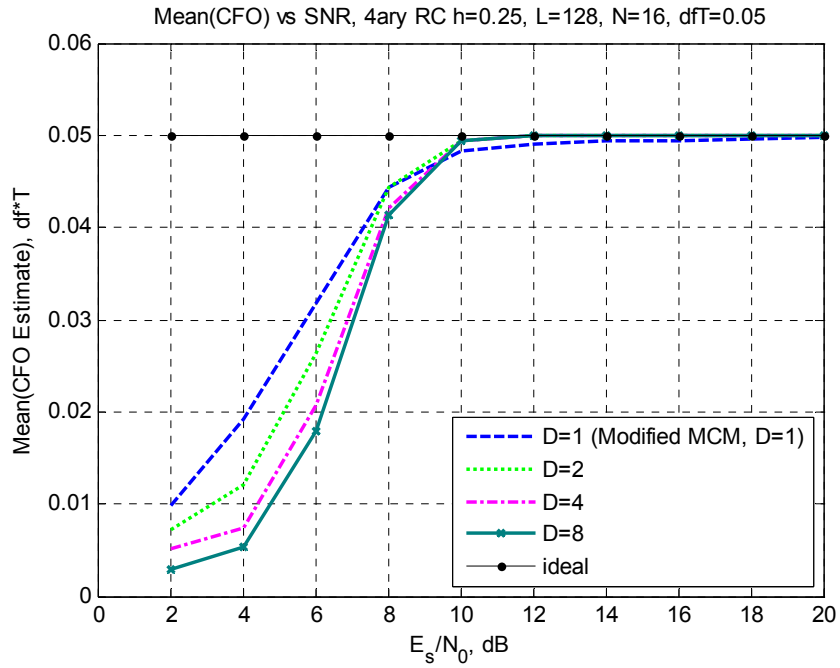


Figure 3-46 Mean value of CFO estimates versus E_s/N_0 for quaternary CPM signals with CFO=0.05.

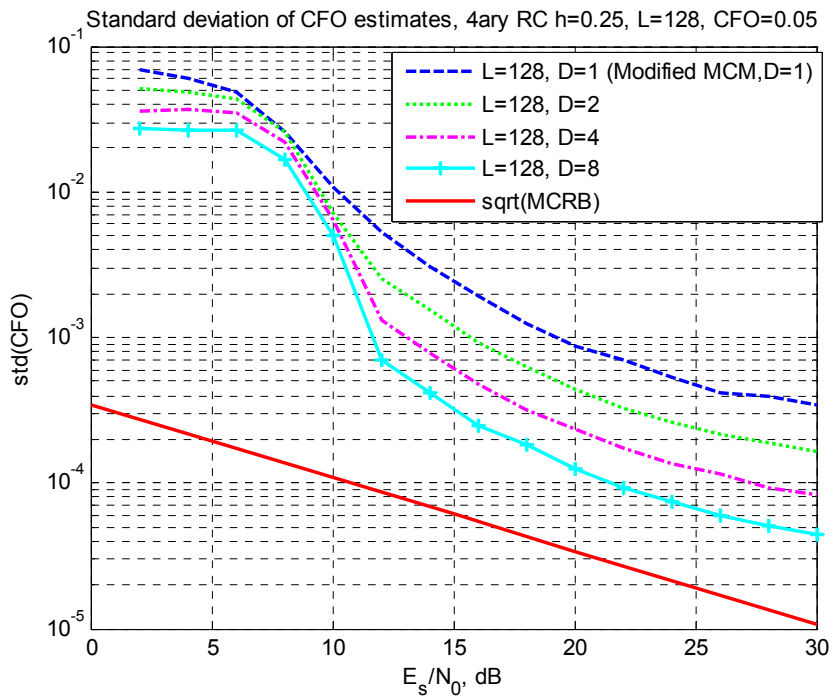


Figure 3-47 Standard deviation of CFO estimates versus E_s/N_0 for quaternary CPM signals with CFO=0.05.

Figure 3-46 shows the mean value of CFO estimates versus E_s/N_0 when the actual CFO is constant at $\Delta fT = 0.05$. It is seen that the mean value of the CFO estimates attains the actual CFO. Furthermore, we note that CFO estimates attain the actual value at lower SNR for higher values of D .

Standard deviation of the CFO estimates versus E_s/N_0 are plotted in Figure 3-47 in the case CFO is constant at $\Delta fT = 0.05$. The scenario is very similar to the case when there is no CFO, except at low SNR ($E_s/N_0 < 12\text{dB}$).

Symbol timing has been estimated by using the modified M&M estimator for 4-ary RC signal with modulation index of $h=0.25$. In this simulation, a block length of $L=64$ symbols and an oversampling ratio of $N=16$ have been used. An RC type IF filter with a bandwidth of $BT=1.61$ and a roll-off factor $\beta=0.35$ has been used to limit the noise bandwidth. These are the optimal values of the filter parameters determined by optimizing the filter for timing MSE. MSE of the symbol timing estimates versus E_s/N_0 is depicted in Figure 3-48 in the case symbol timing offset is uniformly distributed in the interval $[-T/2, T/2]$. When the parameter D in the algorithm increases, MSE of the estimates approaches to the MCRB.

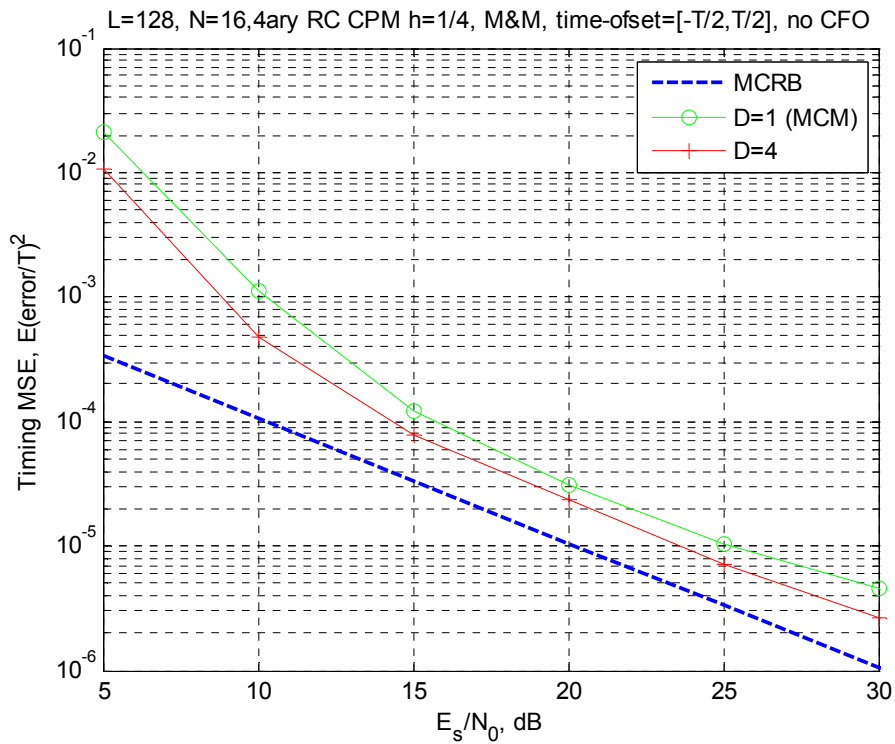


Figure 3-48 MSE of timing estimates versus E_s/N_0 for quaternary CPM signals with CFO=0.

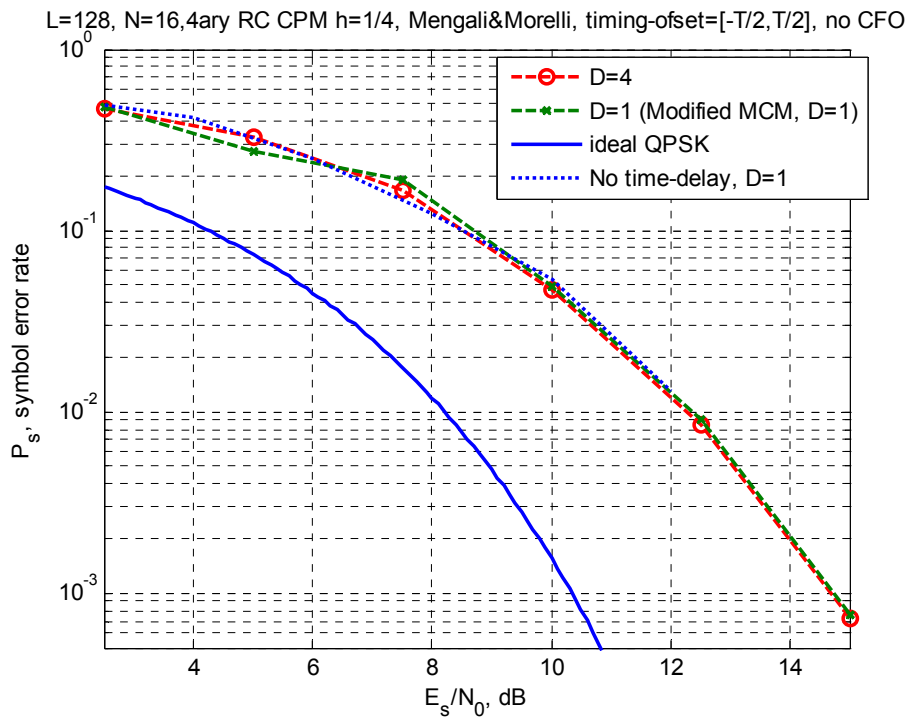


Figure 3-49 Symbol error rate versus SNR for quaternary CPM signals with $h=1/4$.

The effect of the modified M&M symbol timing estimation method on SER performance is shown in Figure 3-49. The difference between the symbol timing offsets estimated for $D=1$ and $D=4$ are negligible compared to the sampling period. Hence, the timing points selected for decimation are expected to be almost the same for $D=1$ and $D=4$, after rounding the timing-offset values. Indeed, SER performances for $D=1$ and $D=4$ are almost the same in both cases of uniformly distributed timing offset over $[-T/2, T/2]$ and zero CFO, as we expect. In the figure, SER performance obtained in the absence of CFO and symbol-timing delay is also displayed. We note that the SER performance of the demodulator virtually does not depend on whether there is a symbol-timing offset or not, because we can estimate and handle the symbol timing offset almost with the same accuracy in the cases when the timing-offset is zero or nonzero (assuming ideal frame synchronization). In addition, SER performance of ideal QPSK given in [4] as

$$P_4 = 2Q\left(\sqrt{\frac{E_s}{N_0}}\right)\left[1 - \frac{1}{2}Q\left(\sqrt{\frac{E_s}{N_0}}\right)\right] \quad (3.65)$$

is also in Figure 3-49 where $Q(x) = \int_x^\infty \frac{1}{\sqrt{2\pi}} e^{-t^2/2} dt$, as a reference.

3.5.3.6 Modified M&M Estimation Method for Octal CPM

The simulations, which are carried out employing 8-ary RC signals with $h=1/8$ to investigate the performance of the modified M&M algorithm, are presented in this section. The low-pass RC filter with a roll-off factor of $\beta=0.30$ and a bandwidth of $BT=1.93$ is used. These are the optimal values of the filter parameters determined by optimizing the filter for CFO MSE.

Figure 3-50 shows mean value of CFO estimates versus E_s/N_0 when the actual CFO is constant at $\Delta fT = 0.05$. It is seen that the mean value of the CFO estimates can reach the actual CFO above $E_s/N_0=20\text{dB}$.

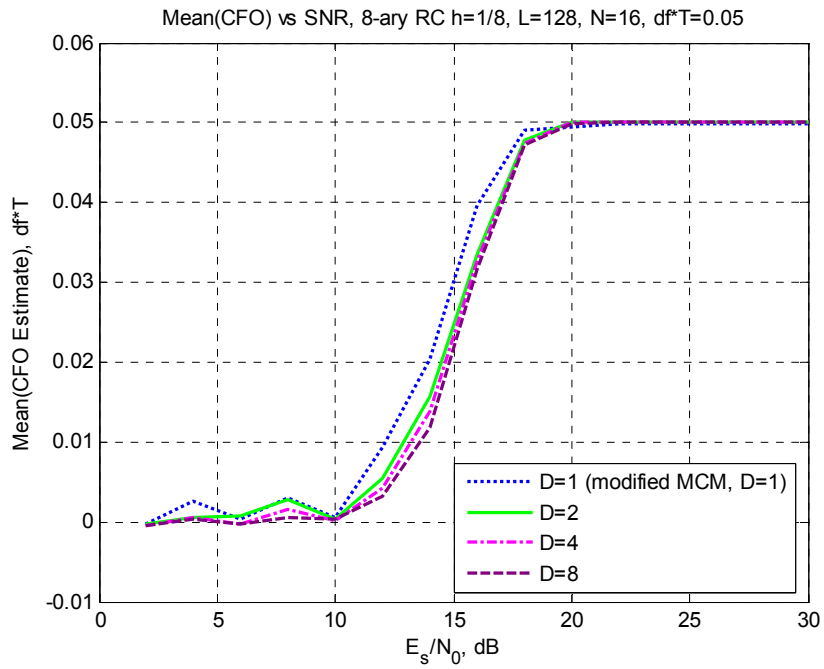


Figure 3-50 Mean value of CFO estimates versus E_s/N_0 for octal CPM signals with CFO=0.05.

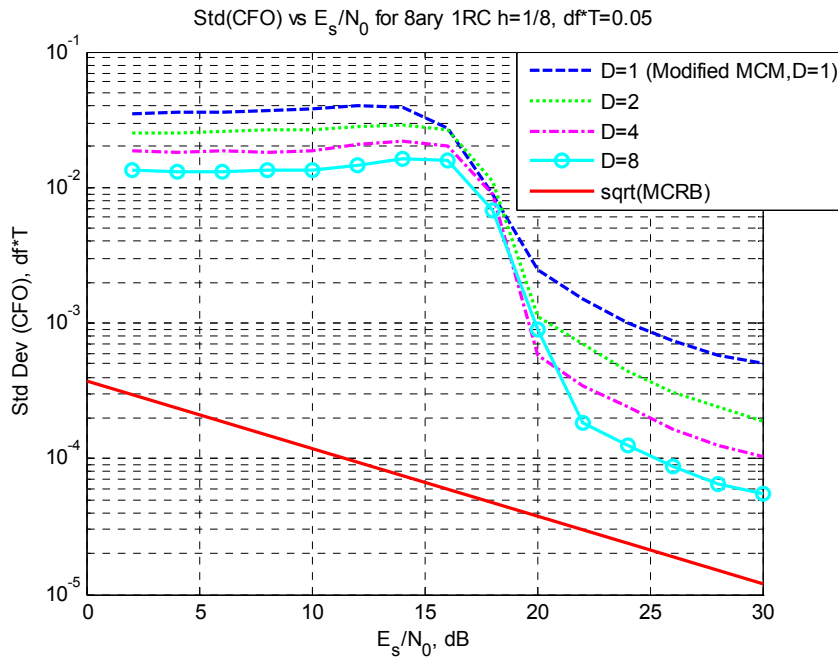


Figure 3-51 Standard deviation of CFO estimates versus E_s/N_0 for octal CPM signals with CFO=0.05.

Standard deviation of the CFO estimates versus E_s/N_0 are plotted in Figure 3-51 for the case CFO is constant at $\Delta fT = 0.05$. As D increases, the standard deviation gets closer to the lower bound at high SNR values.

Symbol timing estimation aspect of the modified M&M estimator was investigated for an 8-ary RC signal with $h=1/8$, $L=128$ and $N=16$, and with a low-pass filter optimized for minimum MSE (Mean square error) timing jitter. This filter has a bandwidth of $BT=1.93$ and a roll-off factor of $\beta=0.30$. The MSE of the symbol timing estimates versus E_s/N_0 is illustrated in Figure 3-52, in the case symbol timing offset is uniformly distributed in the interval $[-T/2, T/2]$. Again, increasing the parameter D in the algorithm, causes the MSE of the estimates to approach more to the MCRB.

Figure 3-53 shows SER performance for $L=128$ and $N=16$. A decimation process is utilized to handle the symbol timing offset which is estimated using the M&M estimator, where the timing offset is uniformly distributed over $[-T/2, T/2]$ and CFO is zero. The SER performance the demodulator is compared to the ideal SER performance of 8PSK (8-ary PSK) signals. The ideal SER for M-ary PSK is given in [4] as

$$P_M \cong 2Q\left(\sqrt{\frac{2E_s}{N_0}} \sin\left(\frac{\pi}{M}\right)\right) \quad (3.66)$$

for high SNR and large M. There is about a 6dB difference between the E_s/N_0 required to obtain a BER of 10^{-3} for 8PSK and 8-ary CPM.

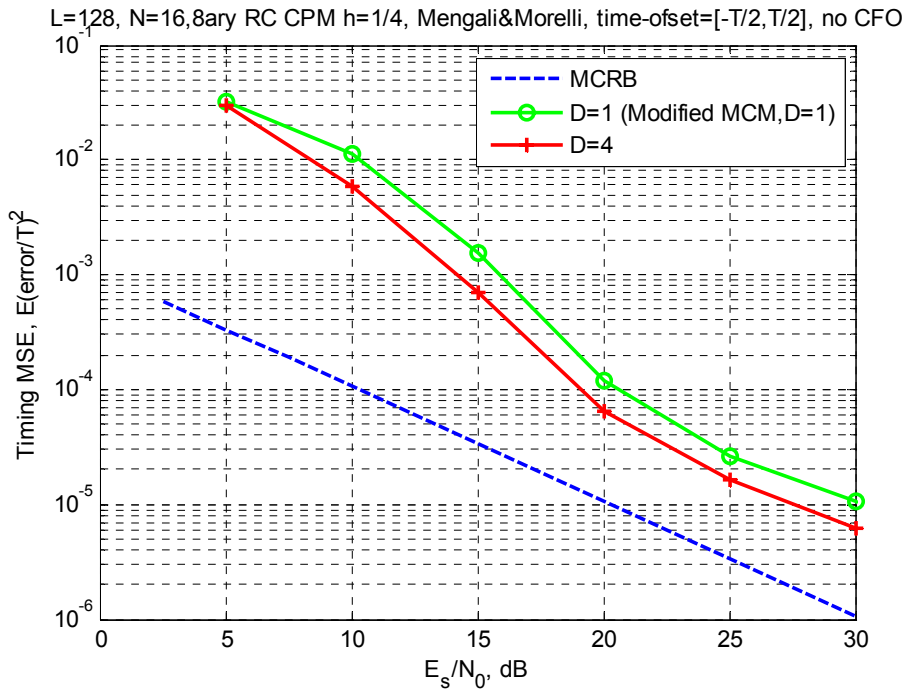


Figure 3-52 MSE of symbol-timing estimates versus E_s/N_0 for octal CPM signals with CFO=0.

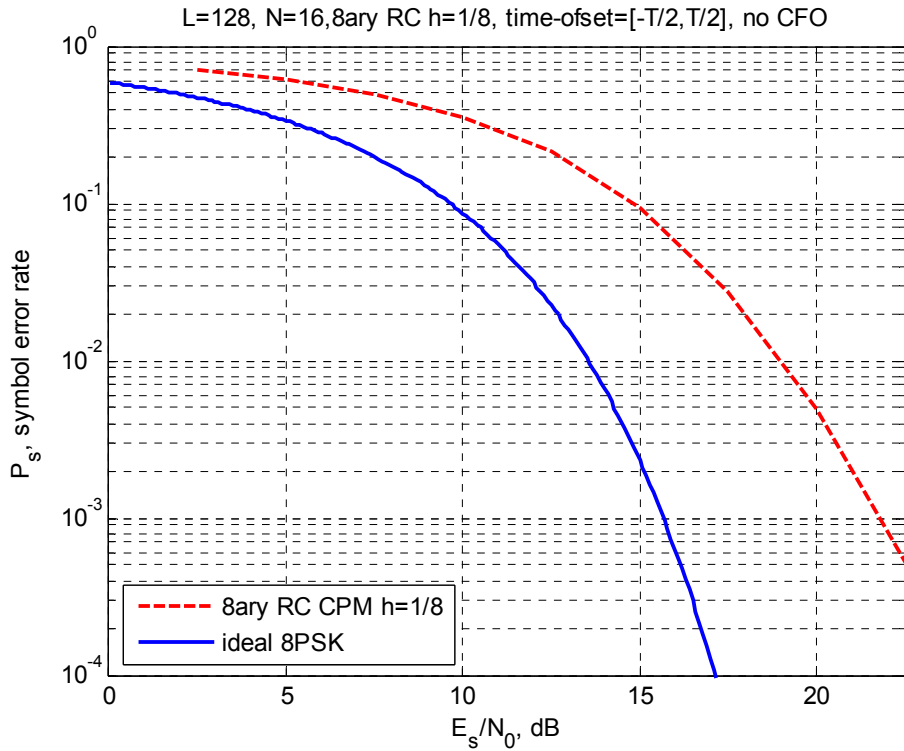


Figure 3-53 Symbol error rate versus E_s/N_0 for 8-ary CPM signals.

CHAPTER 4

SYMBOL DETECTION

In this chapter, we review some major symbol detection methods relevant to our work found in the literature, and examine the combination of the Reduced State Viterbi Differential Detection (RSV DD) algorithm with the joint CFO and symbol timing estimation methods investigated in previous chapters. At the end of the chapter, simulation results on the AWGN channel are presented.

4.1 Literature Survey

We are interested in non-coherent symbol detection methods applicable to CPM signals, because no matter how precise CFO can be estimated, there is always the risk of having phase jumps that can cause block errors.

Coherent maximum likelihood sequence detection (MLSD) is an optimum demodulation method of CPM under AWGN channel [4] when there is no channel imperfection such as CFO, ISI. In contrast, noncoherent schemes do not have the problems of coherent detection, such as hang-ups, acquisition problems, sensitivity to phase jitter, cycle slips, false locks, losses of lock due to severe fading or oscillator frequency instabilities, etc. [30], [32], [33]. In addition, noncoherent schemes seem very attractive for burst-mode transmission, since they do not need a phase acquisition period.

Differential detection is one of the simplest noncoherent reception technique for CPM [2] [34]; nevertheless, their performances are far from that of a coherent receiver. In conventional differential detection, symbol-by-symbol maximum likelihood detection is employed. To approach the performance of ideal coherent

detection, more complex noncoherent receivers based on multiple-symbol differential detection have been proposed [35]- [36]. Multiple-symbol differential receivers are based on maximum-likelihood detection of a block of information symbols on a finite-duration signal observation with no information on the initial carrier phase. In [37], very long observations and high complexity receiver have been used in order to approach the coherent performance, since ML detection of non-overlapped (independent) blocks of information symbols is used. In [38], the differential detection algorithm proposed in [35] is applied to the demodulation of a GMSK signal.

In [36], a method, that uses overlapped observations, is applied so that the observations are not independent any more. This method makes use of the Viterbi Algorithm to implement noncoherent maximum likelihood sequence estimator (MLSE) and takes the fact that the carrier phase can be assumed constant for any observation length using maximally overlapped observations into account.

The maximum likelihood sequence detector (MLSD) for CPM schemes on an AWGN channel is composed of a number of matched filters followed by a Viterbi detector [2] [4]. The large number of states is necessary to describe the CPM signal, so implementation of this MLSD is quite complex [2]. Techniques to reduce the complexity of the optimum Viterbi detector have been studied in [5]- [11] [39] [40]. These techniques are summarized in next paragraphs in more detail.

Svensson's approach of RSSD combined with decision feedback:

Svensson [6], [7], and Nan et al. [40], proposed an approach of RSSD combined with decision feedback applied to CPM. [39] makes use of the reduced state trellis based on RSSD and performs one-symbol differential Viterbi detection.

The transmitted signal for CPM systems can be described by equation (2.5). We shall call $\phi(t; \mathbf{I})$ and $\psi(t; \mathbf{I})$ the *traditional phase* and the *tilted-phase*, respectively, for CPM.

$$\psi(t, \mathbf{I}) = \phi(t; \mathbf{I}) + \pi ht / T \quad (4.1)$$

Rational modulation indexes have the form $h = K / P$ where K and P are relatively prime positive integers. When K is odd, the trellis of CPM is time-varying with period $2T$. The trellis of CPM can be changed to an invariant structure by introducing *the physical tilted phase* $\bar{\psi}(t, \mathbf{U})$

$$\bar{\psi}(t, \mathbf{U}) = \phi(t; \mathbf{I}) \Big|_{\mathbf{I}=2\mathbf{U}-(M-1)} + \frac{\pi ht}{T}(M-1), \quad nT \leq t \leq (n+1)T. \quad (4.2)$$

The modified data sequence $\mathbf{U} = (\dots, U_{n-1}, U_n, \dots)$ can be defined by $U_i = (I_i + (M-1)) / 2$ for M -ary CPM signals. Note that $U_i \in \{0, 1, \dots, M-1\}$.

The state description of CPM signals is

$$\sigma_n = \left[\underbrace{U_n, \dots, U_{n-L}}_{\text{correlative states}}, \underbrace{V_n}_{\text{phase state}} \right] \quad (4.3)$$

where $V_n = R_P \left[\sum_{i=0}^{n-L} U_i \right]$ is the phase state and first $L+1$ states are correlative

states. $R_P[\cdot]$ is the “modulo P operator”. Totally, there are $M^{L-1}P$ states, P is the number of phase states, and M^{L-1} is the number of correlative states. The trellis based on this state definition is called ML trellis.

The main idea of RSSD is to construct a trellis with a reduced number of states compared to ML trellis, and to use this trellis (called the RS trellis) in Viterbi detection. The modified state (state of the RS trellis) is

$$\sigma'_n = [R_{M'}(U_{n-1}), \dots, R_{M'}(U_{n-L+1}), V'_n(P', L')] \quad (4.4)$$

where $V_n'(P', L') = R_{P'} [V_n'(P, L')]$, $1 \leq M_i' \leq M$ for $1 \leq i \leq L-1$, $1 \leq L' \leq L$ and $1 \leq P' \leq P$, also M_i' is a power of 2 and P' is a divisor of P . The vector consisting of the first $L - 1$ terms in the state of the RS trellis is called the correlative superstate, where the superstate is formed by fusing several ML correlative states into a superstate. The total number of modified states is

$$S_{RS} = P' \prod_{i=1}^{L-1} M_i', \quad (4.5)$$

whereas the total number of ML states is $S_{ML} = M^{L-1}P$. The RS trellis can be created by fusing S_{ML} / S_{RS} states in the ML trellis into one super state. The information in the state vector σ_n , can be decomposed into two superstate vectors such that $\sigma_n = \sigma_n' \times \sigma_n''$. The two vectors can specify the state of the CPM signal uniquely. In [5] an expression for σ_n'' is obtained

$$\sigma_n'' = \left[\left[\frac{U_{n-1}}{M_1'} \right], \dots, \left[\frac{U_{n-L+1}}{M_{L-1}'} \right], \left[\frac{V_n'(P, L')}{P'} \right] \right]. \quad (4.6)$$

Each transition in the ML trellis can be expressed as

$$\sigma_n' \times \sigma_n'' : U_n' \rightarrow \sigma_{n+1}' \times \sigma_{n+1}''. \quad (4.7)$$

The RS trellis is based on σ_n' , so a transition in the RS trellis is given by

$\sigma_n' : U_n' \rightarrow \sigma_{n+1}'$ and each possible value of σ_n'' means a parallel transition. We should note that all possible paths in the RS trellis describe both the path in the ML trellis and the path that does not exist in the ML trellis. Only the transitions in the RS trellis that correspond to a valid path in the ML trellis are selected. In the algorithm proposed by [5], only the branch metrics required by the VA are computed and compared.

The superstate σ_n'' at each superstate σ_n' is not known in practice. σ_n'' can be estimated by

$$\hat{\sigma}_n''(\sigma_n') = \left[\left[\frac{\tilde{U}_{n-1}}{M_1'} \right], \dots, \left[\frac{\tilde{U}_{n-L+1}}{M_{L-1}'} \right], \left[\frac{R_p \left[\sum_{i=0}^{n-L'} \tilde{U}_i \right]}{P'} \right] \right] \quad (4.8)$$

where \tilde{U}_i for $i < n$ are the survivor symbols to state σ_n' .

The ML estimate is given by

$$\hat{\sigma}_n(\sigma_n') = \left[\tilde{U}_{n-1}, \dots, \tilde{U}_{n-L+1}, R_p \left[\sum_{i=0}^{n-L} \tilde{U}_i \right] \right]. \quad (4.9)$$

Using this ML state estimate, the branch metric can be found by

$$Z\{\sigma_n' : U_n' \rightarrow \sigma_{n+1}'\} = \int_{nT}^{(n+1)T} r(t) s\{t, U_n', \hat{\sigma}_n(\sigma_n')\} dt. \quad (4.10)$$

These works [6], [7], [39], [40] have been carried out on a reduced number of states which can be used with Viterbi detection combined with decision feedback with a small penalty in performance.

Noncoherent Sequence Detection Method Based on Laurent Decomposition:

[8], [9], [34] use the fact that a CPM signal can be described mathematically as a sum of linearly modulated components affected by ISI.

Based on Laurent decomposition, the complex envelope of M-ary CPM signals may be exactly expressed as

$$s(t, I) = \sum_{k=0}^{K-1} \sum_n a_{k,n} h_k(t - nT). \quad (4.11)$$

The number K of linearly modulated components, the expressions of the pulses $\{h_k(t)\}$, and the symbols $\{a_{k,n}\}$ as a function of the information symbol sequence $\{I_n\}$, may be found in [41]. Most of the signal power is contained in the first $M-1$ components, in the case M is a power of two. Consequently, $K = M-1$ may lead to a good trade-off between quality of approximation and number of components.

Using Laurent decomposition approach new matched filters are obtained. Correlating matched filter outputs with hypothetical symbol sequence, branch metrics are found. Viterbi algorithm is used with branch metrics. The noncoherent sequence detection scheme proposed in [9] is based on the concept of estimating the phase θ using the sampled output of a few matched filters. The phase is estimated by PSP approach (per-survivor-processing). In PSP, per-survivor estimates (based on the best survivor) are used in branch metric computation. Intuitively, a better phase estimate is obtained using a larger value of N (implicit phase memory), and at the limit where $N \rightarrow \infty$ coherent detection performance is obtained.

Reduced State Sequence Estimation (RSSE) with Set Partitioning and Decision Feedback

In [10], a reduced-state sequence estimator for linear ISI channels is described. The estimator uses a conventional Viterbi algorithm (VA) with decision feedback to search a reduced-state “subset trellis” which is constructed using set partitioning principles. Ungerboeck’s set partitioning principles are used to form trellises with a reduced number of states.

In the case M -ary symbol sequence $\{x_n\}$ is transmitted, the received sequence $\{r_n\}$ can be written in the form $r_n = x_n + \langle p_n, f \rangle + w_n$, where $\{w_n\}$ represents a complex white Gaussian noise sequence with zero mean. The expression $\langle p_n, f \rangle$ is an inner product between the state vector

$p_n = [x_{n-1}, x_{n-2}, \dots, x_{n-K}]$ consisting of the K most recent transmitted symbols, and the vector f denoting the complex post-cursor ISI coefficients associated with the overall channel impulse response, i.e., $f = [f_1, f_2, \dots, f_K]$.

In MLSE, the trellis states are defined as $p_n = [x_{n-1}, x_{n-2}, \dots, x_{n-K}]$. The ML trellis has M^K states, because each element of the state vector may take one of M values, and there are M transitions to and from each state.

A two-dimensional set partitioning denoted as $\Omega(k)$ is defined for each element x_{n-k} in the vector p_n to reduce the number of states. [10] proposes to categorize the signal set to J_k subsets for $k=1, \dots, K$. Consequently, the subsets to which K most recent symbols belong specify states of the trellis instead of these symbols.

The set partitionings are restricted so that

- i) the numbers J_k are nonincreasing (i.e., $J_1 \geq J_2 \geq \dots \geq J_K$), and
- ii) the partitioning $\Omega(k)$ is a further partition of the subsets of $\Omega(k+1)$ for each k between 1 and $K-1$.

By these constraints, the *subset state* of a sequence at time n is defined as $t_n = [a_{n-1}(1), a_{n-2}(2), \dots, a_{n-K}(K)]$ where $a_{n-i}(i)$ represents the subset of the i^{th} recent symbol.

For transitions from a state t_n , the branch metrics is

$$b[r_n; t_n, x_n] = |r_n - (\hat{p}_n(t_n), f) - x_n|^2 \quad (4.12)$$

where $\hat{p}_n(t_n)$ represents the K most recent symbols stored in the “*path history*” associated with the state t_n . When $J_1 < M$, the actual surviving symbols are stored in RSSE because the correspondence between state and symbol sequences is not one-to-one.

In the case there are parallel transitions in the subset trellis (i.e., $J_1 < M$), the VA can first select the symbols with the minimum branch metric for each subset

transition; actually for each state, the VA makes delay-free decisions between symbols within the subsets of $\Omega(1)$ using past decisions obtained from path histories as feedback. It is not necessary to compute the branch metric explicitly for every symbol (i.e. only J_1 explicit branch metrics are necessary), if the partitioning $\Omega(1)$ has enough symmetry.

This step reduces the number of possible extensions of the N path histories from NM to NJ_1 . Selecting the paths with minimum accumulated metric for each possible next state t_{n+1} reduces this number to N (i.e., the RSSE stores one "survivor" path for each possible combination of the K most recent subsets). By choosing $J_k = M$ for $1 < k < K'$ and $J_k = 1$ for $K'+1 < k < K$, decision feedback sequence estimator (DFSE, a special case of the RSSE) is obtained. In this case, the received sequence $\{r_n\}$ can be written as

$$r_n = x_n + (p'_n, f') + (p''_n, f'') + w_n \quad (4.13)$$

where the vectors f' and f'' are defined according to

$$f = [f' | f''] = [f_1, f_2, \dots, f_{K'} | f_{K'+1}, \dots, f_K] \quad (4.14)$$

$$p_n = [p'_n | p''_n] = [x_{n-1}, x_{n-2}, \dots, x_{n-K'} | x_{n-K'+1}, \dots, x_{n-K}] \quad (4.15)$$

The branch metric is given by

$$b[r_n; p'_n, x_n] = \left| r_n - (\hat{p}''_n(p'_n), f'') - (p'_n, f') - x_n \right|^2 \quad (4.16)$$

where $(\hat{p}''_n(p'_n), f'')$ denotes an estimate of the residual ISI for the state p'_n . The feedback decisions $\hat{p}''_n(p'_n)$ are obtained from the path histories. It is guaranteed that the branch metric of the correct path is the ML metric, unless it is eliminated in favor of some incorrect path. The main difference between *MLSE* and *DFSE* is that two paths merge earlier (when they agree in K' rather than K most recent symbols) in the (reduced) trellis used by the *DFSE*.

The RSSE becomes a zero-forcing decision-feedback equalizer (DFE) when $J_k = 1$ for all k . When $J_k = M$ for all k , the RSSE turns into an *MLSE*. A tradeoff between performance and complexity of the estimator can be obtained, by choice of the J_k .

Adachi's Reduced-state Viterbi differential detection using a recursively estimated phase reference for M-ary DPSK

The reduced-state Viterbi algorithm (VA), with feedback combined with the structure of path metric computations is presented in the work by Adachi [11] for the differential detection of M-ary DPSK signals. The number of states in the trellis of the VA is reduced to M, and the phase reference used for differential detection is estimated recursively for each state in the trellis, along the surviving path ending in each state. The proposed differential detection is called reduced-state Viterbi differential detection (RSV DD). The simplest form of RSV DD, decision feedback DD (DF DD), has also been derived. It allows only a single path to survive, so that a symbol-by-symbol decision is made.

For the optimal detection, the branch metric is given by

$$\lambda_n = \text{Re} \left[r_n \left(\sum_{l=1}^n r_{n-l} \exp j \sum_{k=1}^{l-1} \Delta \phi_{n-k} \right)^* \exp -j \Delta \phi_n \right] \quad (4.17)$$

where r_n is the complex baseband representation of the received signal taken at $t=nT$, $\Delta \phi_n$ is the phase difference between consecutive transmitted symbols.

The estimate of the term inside the round brackets of equation (4.17) is given recursively by

$$\eta_{n-1}(\Delta \phi_{n-1}) = r_{n-1} + \mu \eta_{n-2}(\Delta \phi_{n-2}) \exp j \Delta \phi_{n-1} \quad (4.18)$$

where μ is the forgetting factor. The branch metric for the transition from the state $\Delta \phi_{n-1}$ to $\Delta \phi_n$ can be calculated from

$$\lambda_n(\Delta \phi_{n-1} \rightarrow \Delta \phi_n) = \text{Re} [r_n (\eta_{n-1}^*(\Delta \phi_{n-1}) \exp -j \Delta \phi_n)]. \quad (4.19)$$

The block diagram of RSV DD is shown in Figure 4-1. The RSV DD includes branch metric computation, Viterbi decoding and phase reference estimation blocks.

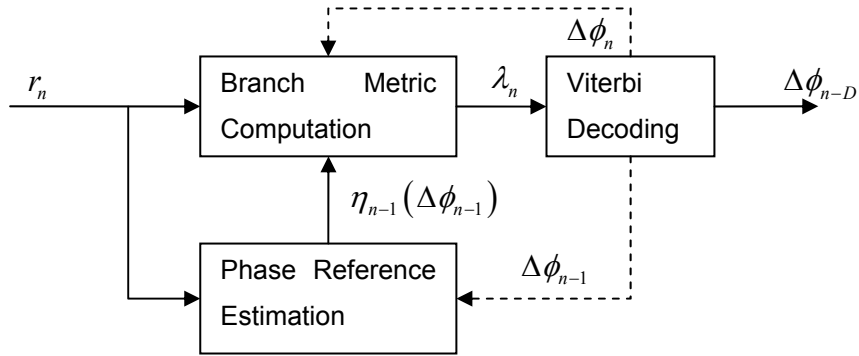


Figure 4-1 Block diagram of Adachi's RSV DD Algorithm.

The steps of the algorithm are as follows:

- (i) Using the phase reference $\eta_{n-1}(\Delta\phi_{n-1})$, compute branch metric $\lambda_n(\Delta\phi_{n-1} \rightarrow \Delta\phi_n)$ at time n .
- (ii) Add $\lambda_n(\Delta\phi_{n-1} \rightarrow \Delta\phi_n)$ to the path metric to obtain the conditional path metric at state $\Delta\phi_n$.
- (iii) Repeat steps (i) to (ii) for all M states to compare M conditional path metrics, select the state of $\Delta\phi_{n-1}$ that has the maximum conditional metric (this determines the surviving path ending in state $\Delta\phi_n$), determine the path metric and compute the phase reference $\eta_n(\Delta\phi_n)$
- (iv) Repeat steps (i) to (iii) for all M states of $\Delta\phi_n$.
- (v) Find state $\Delta\phi_n$ that gives the maximum value of the path metric, trace the selected path D steps back, and output $\Delta\phi_{n-D}$

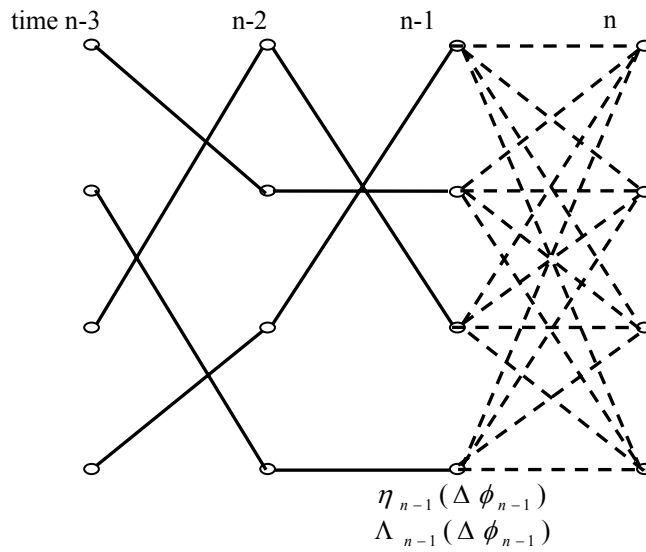


Figure 4-2 Trellis diagram for 4DPSK (solid lines show surviving paths).

RSV DD allows a total of M paths to survive. There is a D -symbol decision delay. If only a single path is allowed to survive so that a symbol-by-symbol decision is made, then we obtain DF DD. Its decision rule is

$$\Delta\bar{\phi}_n = \max_{\text{over } \Delta\phi_n} \text{Re} \left[r_n \eta_{n-1,DF}^* \exp -j\Delta\phi_n \right] \quad (4.20)$$

where $\eta_{n-1,DF} = r_{n-1} + \mu \eta_{n-2,DF} \exp j\Delta\bar{\phi}_{n-1}$. (4.21)

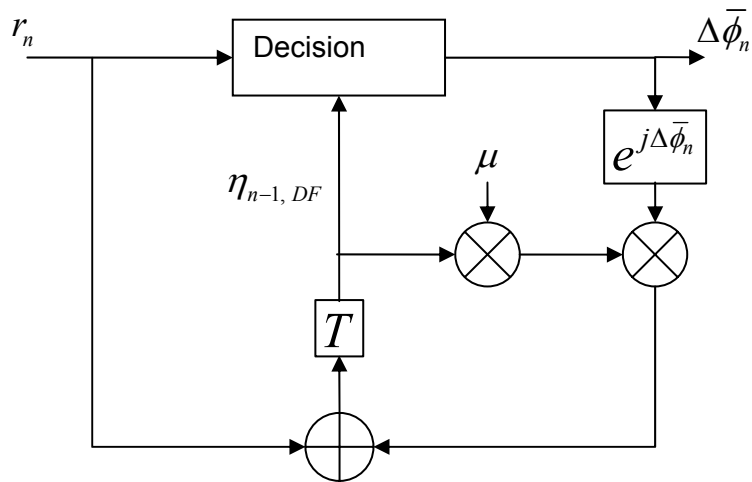


Figure 4-3 Block diagram of Adachi's DF DD Algorithm.

Viterbi DD requires an M^{L-1} state Viterbi decoder, and a total of M^L branch-metric computations is required to determine M surviving paths at each time. On the other hand, RSV DD requires only M^2 branch metric computations at each time.

By increasing the forgetting factor μ , the BER performance improves in an AWGN channel when there is no CFO. However, increasing the forgetting factor μ causes the receiver to be affected by the CFO more.

4.2 Reduced State Viterbi Differential Detection (Adachi's Detection Method) with Joint CFO and Symbol Timing Estimation

In chapter 3, we have examined the demodulator structure, which uses the conventional differential detection algorithm and one of the modified MCM or the modified M&M estimation method. In order to enhance error performance of the detector in this demodulator structure, we have reviewed some symbol detection methods relevant to our work in previous sections. In conjunction with our work on

synchronization, we preferred to examine Adachi's symbol detection method in more detail.

In the modified MCM and the M&M estimation methods, multiple symbol phase differences are used in order to estimate CFO and symbol timing. Therefore, a differential detector seems to be convenient for integration to the demodulator structure described in chapter 3. Since both Adachi's detection method and the estimation methods (MCM and M&M) employ phase differences between symbols, we can easily combine Adachi's detector and the estimation procedure without requiring additional complexity such as using matched filters.

We know that Viterbi DD requires M^L branch-metric computations to determine M surviving paths at each time, whereas Adachi's RSV DD requires only M^2 branch metric computations. Namely, Adachi's detector has M^{L-2} times less computational complexity. We also note that the computational complexity of Adachi's detector does not depend on the observation length L .

In Adachi's detection algorithm, some important properties of the detector can be adjusted by only varying the forgetting factor μ . The BER performance can approach to that of coherent detection without increasing the computational complexity, by simply increasing μ [11]. The tracking ability against fading can be easily controlled by varying μ [11].

We would like to combine the detector with the CFO and symbol timing estimator, which may not provide very good estimates in some cases. Therefore, the detector is preferred to work properly even if CFO estimations are not so good. In Adachi's detection algorithm, we can adjust the sensitivity to the quality of the CFO estimates by changing μ .

Although Adachi's symbol detection method is proposed for the detection of M-ary DPSK signals, the method can also be applied for the detection of CPM signals, because it is based on differential detection.

The trellis diagram of the binary CPM is shown in Figure 4-4. There are two possible states for the symbol phase difference $\Delta\phi_n \in \{+\pi/2, -\pi/2\}$.

In order to apply RSV DD to the CPM signals with CFO and symbol timing-offset, CFO and symbol-timing offset should be estimated. Then, the CFO estimate $\Delta\hat{\omega}$ is inserted to equations (4.18) - (4.21) by using $\Delta\phi_n + \Delta\hat{\omega}$ instead of $\Delta\phi_n$. To handle the symbol-timing offset, the decimation procedure explained in section 3.5.1 is used. In Figure 4-5, the block diagram of RSV DD algorithm coupled with the estimation block is shown. In the figure, $r_{i,n}$ denotes the low-pass filtered received signal with sampling frequency $1/T_s$, r_n denotes the decimated samples of the filtered received signals with sampling frequency $1/(NT_s)$.

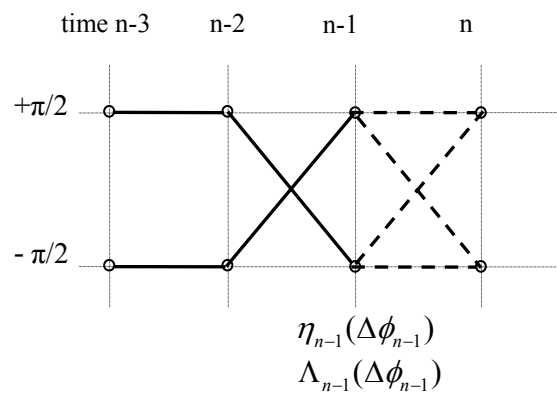


Figure 4-4 Trellis diagram for binary CPM (solid lines show surviving paths).

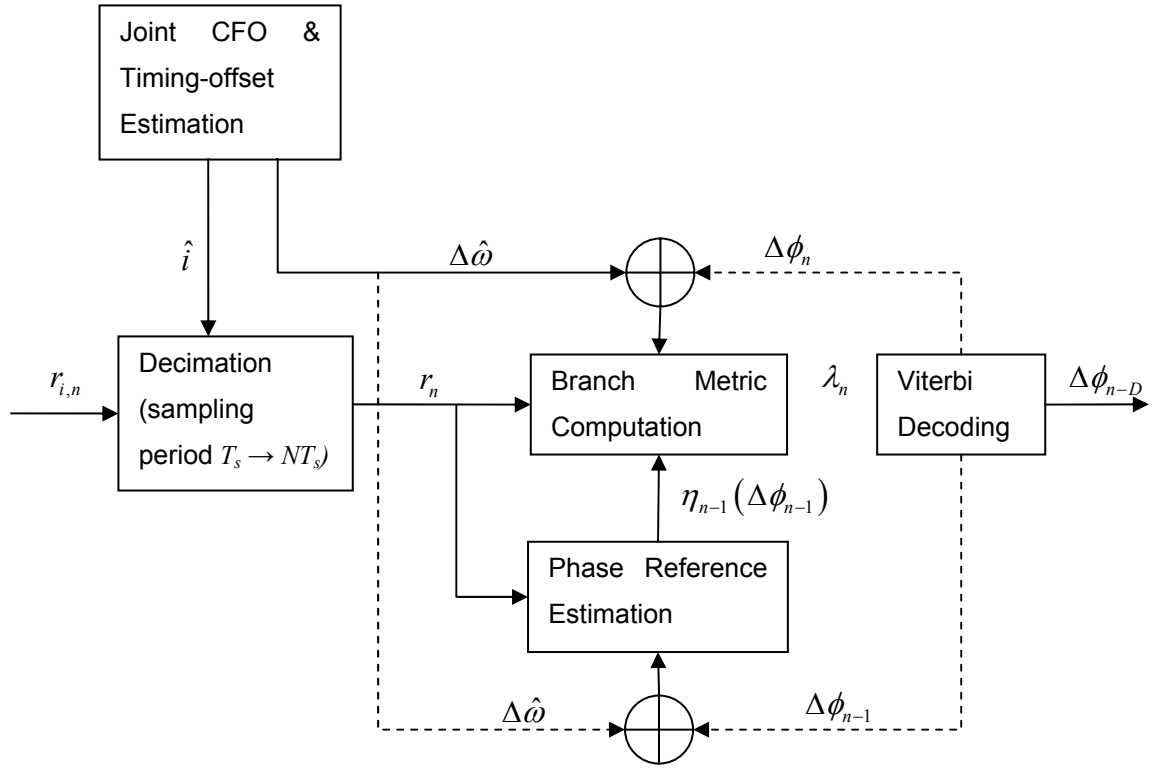


Figure 4-5 Block diagram of RSV DD algorithm coupled with estimation block.

As an example, we examine equations of RSV DD algorithm for binary CPM signals in more detail. Firstly, initial assignments are carried out. The branch metrics for state transitions are:

$$\lambda_0(-1 \rightarrow +1) = \text{Re} \left\{ r_2 r_1^* e^{-j(-\pi/2 + \Delta\hat{\omega})} + \mu r_1 r_0^* e^{-j(\pi/2 + \Delta\hat{\omega})} + \mu r_2 r_0^* e^{-j(\Delta\hat{\omega})} \right\}, \quad (4.22)$$

$$\lambda_0(-1 \rightarrow -1) = \text{Re} \left\{ r_2 r_1^* e^{-j(-\pi/2 + \Delta\hat{\omega})} + \mu r_1 r_0^* e^{-j(-\pi/2 + \Delta\hat{\omega})} + \mu r_2 r_0^* e^{-j(-\pi + \Delta\hat{\omega})} \right\}, \quad (4.23)$$

$$\lambda_0(+1 \rightarrow +1) = \text{Re} \left\{ r_2 r_1^* e^{-j(\pi/2 + \Delta\hat{\omega})} + \mu r_1 r_0^* e^{-j(\pi/2 + \Delta\hat{\omega})} + \mu r_2 r_0^* e^{-j(\pi + \Delta\hat{\omega})} \right\}, \quad (4.24)$$

$$\lambda_0(+1 \rightarrow -1) = \text{Re} \left\{ r_2 r_1^* e^{-j(\pi/2 + \Delta\hat{\omega})} + \mu r_1 r_0^* e^{-j(-\pi/2 + \Delta\hat{\omega})} + \mu r_2 r_0^* e^{-j(\Delta\hat{\omega})} \right\}. \quad (4.25)$$

The phase reference estimates:

$$\eta_0(-1) = r_1 + \mu r_0 e^{j(-\pi/2 + \Delta\hat{\omega})}, \quad (4.26)$$

$$\eta_0(+1) = r_1 + \mu r_0 e^{j(\pi/2 + \Delta\hat{\omega})}. \quad (4.27)$$

The path metrics at states +1 and -1 are:

$$\Lambda_0(+1) = 0, \quad (4.28)$$

$$\Lambda_0(-1) = 0. \quad (4.29)$$

Then, the branch metrics for state transitions are computed for all indices i :

$$\lambda_i(-1 \rightarrow -1) = \text{Re} \left\{ r_{i+1} \eta_i^*(-1) e^{-j(-\pi/2 + \Delta\hat{\omega})} \right\}, \quad (4.30)$$

$$\lambda_i(-1 \rightarrow +1) = \text{Re} \left\{ r_{i+1} \eta_i^*(-1) e^{-j(\pi/2 + \Delta\hat{\omega})} \right\}, \quad (4.31)$$

$$\lambda_i(+1 \rightarrow +1) = \text{Re} \left\{ r_{i+1} \eta_i^*(+1) e^{-j(\pi/2 + \Delta\hat{\omega})} \right\}, \quad (4.32)$$

$$\lambda_i(+1 \rightarrow -1) = \text{Re} \left\{ r_{i+1} \eta_i^*(+1) e^{-j(-\pi/2 + \Delta\hat{\omega})} \right\}. \quad (4.33)$$

In addition, the conditional path metrics $\Lambda_i'(\Delta\phi_{i-1} \rightarrow \Delta\phi_i)$ are obtained where

$\Delta\phi_{i-1} \rightarrow \Delta\phi_i$ indicates the last state transition:

$$\Lambda_i'(-1 \rightarrow -1) = \Lambda_i(-1) + \lambda_i(-1 \rightarrow -1), \quad (4.34)$$

$$\Lambda_i'(-1 \rightarrow +1) = \Lambda_i(-1) + \lambda_i(-1 \rightarrow +1), \quad (4.35)$$

$$\Lambda_i'(+1 \rightarrow +1) = \Lambda_i(+1) + \lambda_i(+1 \rightarrow +1), \quad (4.36)$$

$$\Lambda_i'(+1 \rightarrow -1) = \Lambda_i(+1) + \lambda_i(+1 \rightarrow -1). \quad (4.37)$$

Comparing conditional path metrics, the maximum conditional metric is selected. Thus, we determine the surviving paths ending in each state and the path metric as the maximum conditional path metric. Moreover, we compute the next phase reference corresponding to the last state of the surviving path. A pseudo-code to explain the procedure is given below:

If $\Lambda'_i(-1 \rightarrow -1) > \Lambda'_i(+1 \rightarrow -1)$, then

$$\begin{aligned}\eta_{i+1}(-1) &= r_{i+1} + \mu\eta_i(-1)e^{j(-\pi/2+\Delta\hat{\omega})} \\ \Lambda_{i+1}(-1) &= \Lambda'_i(-1 \rightarrow -1) \\ path_i(-1) &= [path_{i-1}(-1) -1]\end{aligned}\tag{4.38}$$

Else

$$\begin{aligned}\eta_{i+1}(-1) &= r_{i+1} + \mu\eta_i(+1)e^{j(-\pi/2+\Delta\hat{\omega})} \\ \Lambda_{i+1}(-1) &= \Lambda'_i(+1 \rightarrow -1) \\ path_i(-1) &= [path_{i-1}(+1) -1]\end{aligned}\tag{4.39}$$

If $\Lambda'_i(-1 \rightarrow +1) > \Lambda'_i(+1 \rightarrow +1)$, then

$$\begin{aligned}\eta_{i+1}(-1) &= r_{i+1} + \mu\eta_i(-1)e^{j(\pi/2+\Delta\hat{\omega})} \\ \Lambda_{i+1}(-1) &= \Lambda'_i(-1 \rightarrow +1) \\ path_i(-1) &= [path_{i-1}(-1) +1]\end{aligned}\tag{4.40}$$

Else

$$\begin{aligned}\eta_{i+1}(+1) &= r_{i+1} + \mu\eta_i(+1)e^{j(\pi/2+\Delta\hat{\omega})} \\ \Lambda_{i+1}(+1) &= \Lambda'_i(+1 \rightarrow +1) \\ path_i(+1) &= [path_{i-1}(+1) +1]\end{aligned}\tag{4.41}$$

Here $path_i$ represents the surviving path for index i . The steps represented in equations (4.30)-(4.41) are computed recursively for index i . Note that there is a D-symbol decision delay. That is, the selected path is traced D step back and then determined.

The same algorithm can be applied to the quaternary CPM signals as well. In that case, there will be four states for the symbol phase difference

$\Delta\phi_n \in \{-3\pi/2, -\pi/2, 3\pi/2, \pi/2\}$. The trellis diagram for quaternary CPM signals is illustrated in Figure 4-6. The same procedure described for binary CPM signals can be followed noting that number of states are 4 and there are 16 possible state transitions at time nT . Hence, there are 16 branch metric computations and a comparison of path metrics for each state, i.e. 4 path metric comparisons.

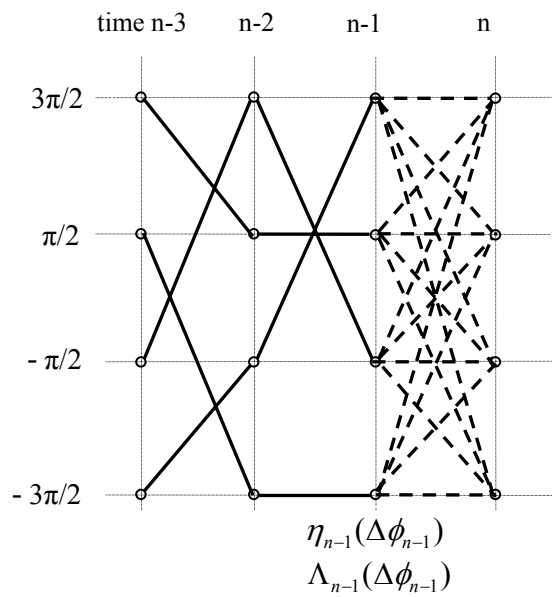


Figure 4-6 Trellis diagram for quaternary CPM (solid lines show surviving paths).

4.3 Simulation Results

The general simulation model is as illustrated in Figure 3-8. The criterion to evaluate performance of the demodulator is BER versus E_b/N_0 .

In this section, BER performances of the demodulator using RSV DD method described in previous section combined with estimation methods described in

sections 3.2 and 3.3 are examined under AWGN channel. Unless otherwise specified, performances of RC frequency pulsed CPM signals are investigated.

RSV DD and conventional differential detection (CDD) have been investigated for full response binary CPM signals with $h=0.5$.

In order to test Adachi's detector, BER performance of the detector for binary MSK is examined under AWGN assuming ideal CFO and symbol timing synchronization without using an IF filter. As seen in Figure 4-7, BER performance of the Adachi detector can almost attain the ideal BPSK performance for the forgetting factor $\mu=1$. As the forgetting factor μ approaches to zero, BER performance of the detector gets closer to the performance of CDD.

BER performances of RSV DD and CDD are compared for binary CPM signals with 1REC pulse, $h=0.5$, $N=16$, $L=64$ zero CFO and symbol-timing delay in Figure 4-8. In this simulation, perfect CFO estimation is assumed in order to see the performance in the case of perfect CFO estimation. In RSV DD, forgetting factor is taken as $\mu=1$. It seems using RSV DD instead of CDD improves BER performance of 1REC pulsed binary CPM signals. The difference between E_b/N_0 required to obtain a BER of 10^{-3} with CDD and RSV DD is about 0.9 dB.

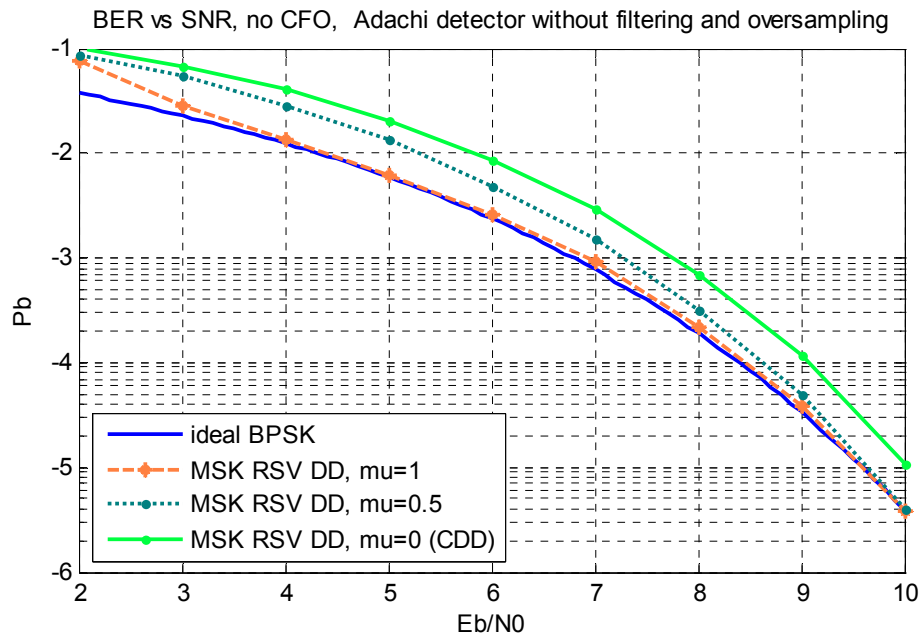


Figure 4-7 BER vs SNR for RSV DD of binary CPM signals

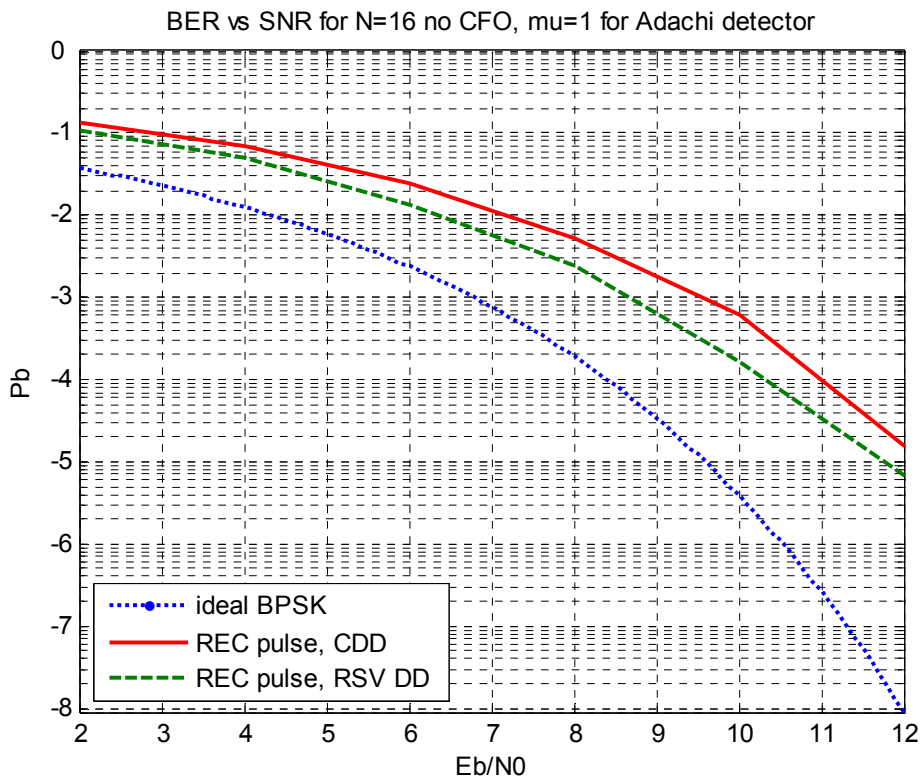


Figure 4-8 BER vs SNR for CDD and RSV DD of binary CPM signals.

BER performances of RSV DD with $\mu=1$ and CDD are compared for binary CPM signals with 1RC pulse, $h=0.5$, $N=16$, $L=64$; zero CFO and no symbol-timing delay in Figure 4-9. In this simulation, perfect CFO estimation and compensation is performed for zero CFO, while no CFO compensation has been carried out for $\Delta fT=0.005$ in order to see the effect of imperfect CFO estimation and compensation. BER performance of 1RC pulsed binary CPM signals can be improved by using RSV DD instead of CDD. The improvement between the E_b/N_0 required to obtain a BER of 10^{-3} with CDD and RSV DD is about 1 dB. BER performance of RSV DD is about 0.5 dB poorer than ideal BPSK performance, this degradation may be attributed to the IF filter. When CFO ($\Delta fT=0.005$) is not compensated, the BER performance is degraded much (more than ten times for 10 dB).

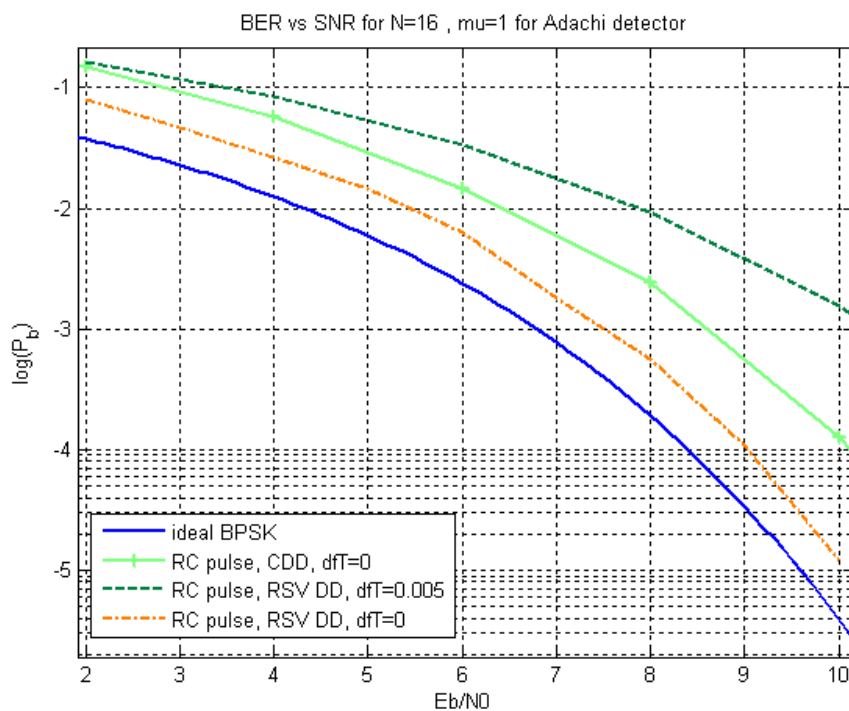


Figure 4-9 BER vs SNR for CDD and RSV DD of binary CPM signals.

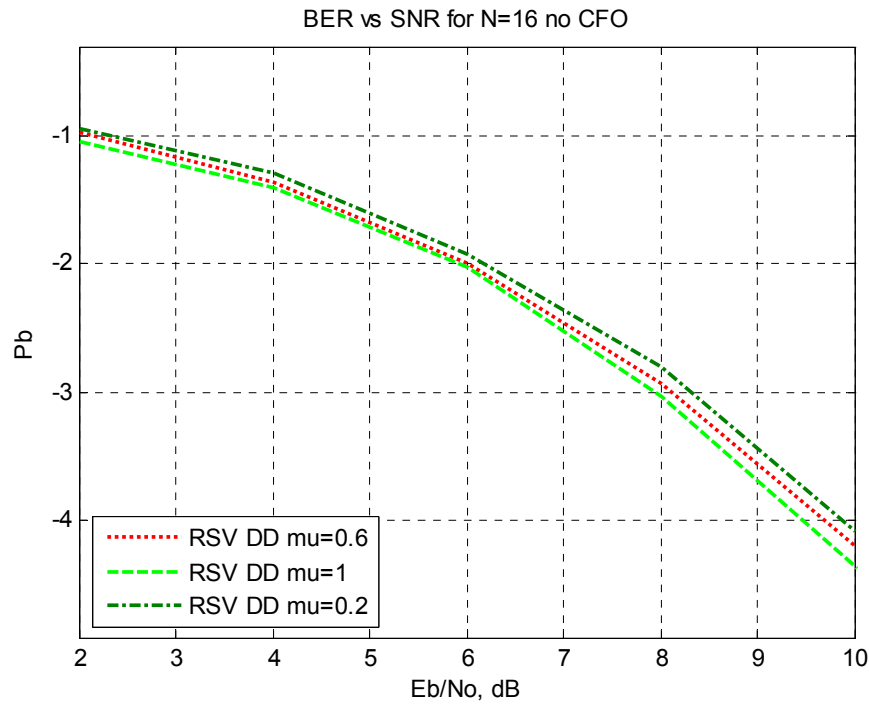


Figure 4-10 BER vs SNR for RSV DD of binary CPM signals.

Figure 4-10 is the BER vs E_b/N_0 plot obtained applying by RSV DD to RC pulsed MSK-type signal with no CFO and no symbol-timing delay for different values of forgetting factor μ . By reducing the forgetting factor μ , BER performance somewhat degrades unless CFO is compensated perfectly.

The BER performance is illustrated in Figure 4-11 and Figure 4-12, in the case RC pulsed MSK-type signal with CFO ($\Delta fT=\{0.01, 0.05\}$) and zero symbol-timing delay is demodulated using different values of forgetting factor μ without CFO compensation. We cannot always improve BER performance by increasing the forgetting factor μ if CFO estimation and compensation is imperfect. In the case uncompensated CFO is $\Delta fT=0.01$, choosing forgetting factor $\mu=0.6$ gives the best BER vs E_b/N_0 plot, while the best BER vs E_b/N_0 plot can be obtained by using forgetting factor $\mu=0.2$ for $\Delta fT=0.05$.

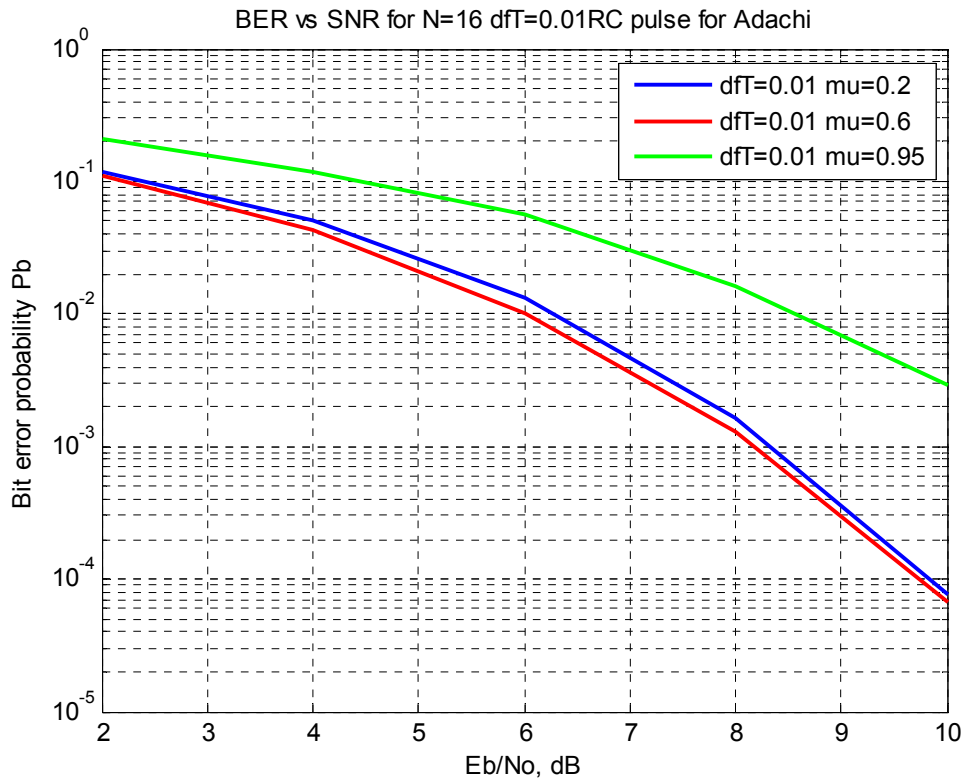


Figure 4-11 BER vs SNR for RSV DD of binary CPM signals with $\Delta fT=0.01$.

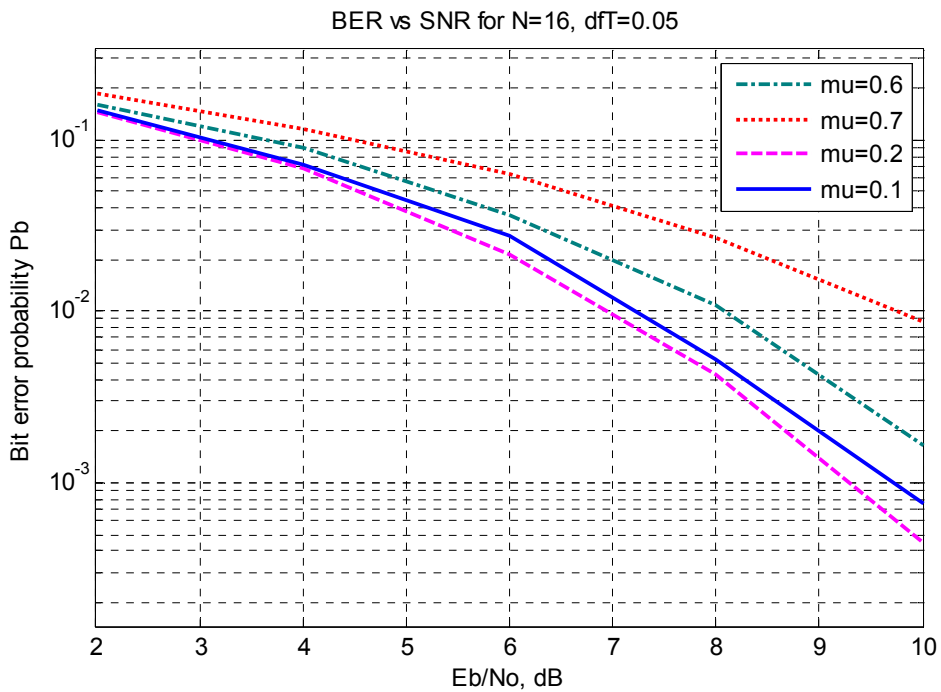


Figure 4-12 BER vs SNR for RSV DD of binary CPM signals with $\Delta fT=0.05$.

When frequency is compensated using CFO estimates obtained by the modified MCM estimation algorithm, we obtain BER performance for binary RC pulsed CPM signal shown in Figure 4-13. In the estimation algorithm, 1-symbol phase differences are used for $\Delta fT=0.10$. BER vs SNR graph shows that there is an improvement of 0.8 dB SNR with respect to conventional differential detection method. The BER performance improves most when the forgetting factor is $\mu=0.4$.

For $\Delta fT=0.1875$, the best BER vs SNR performance is obtained adjusting the forgetting factor μ . Frequency compensation is made by the CFO estimates which are obtained by the modified MCM estimation algorithm (using 1-symbol phase differences). Choosing the forgetting factor $\mu=0.7$, the closest BER performance to the ideal BPSK is obtained. The E_b/N_0 required to obtain a BER of 10^{-3} is 1.8dB higher than the ideal BPSK.

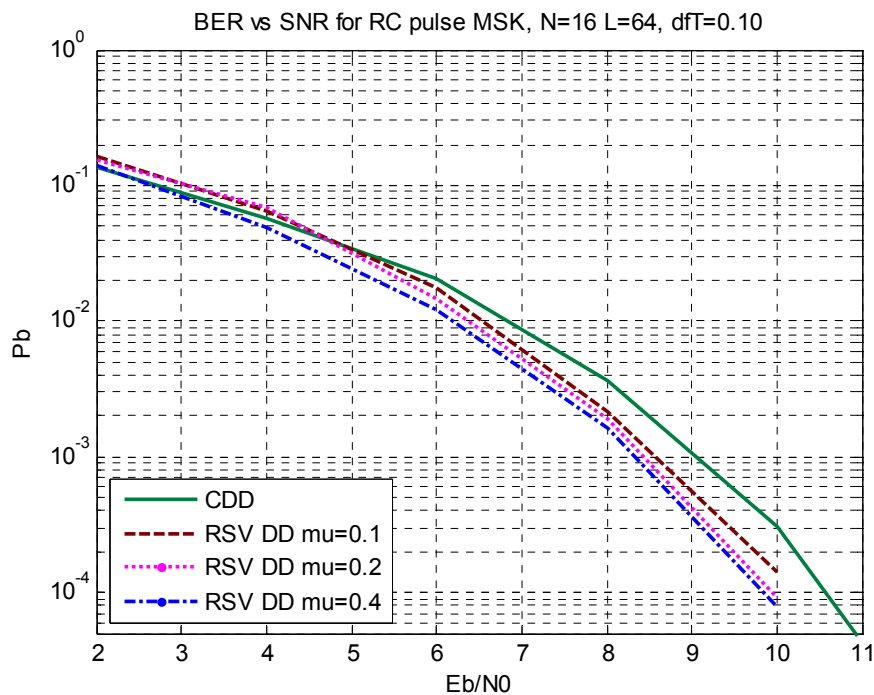


Figure 4-13 BER vs SNR for RSV DD of binary CPM signals with $\Delta fT=0.10$.

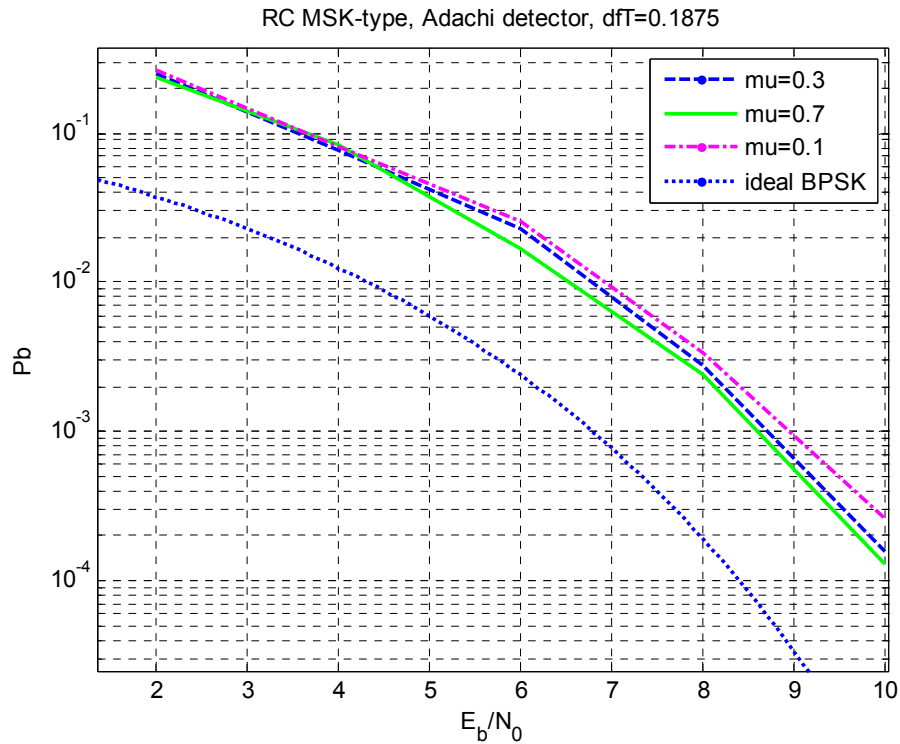


Figure 4-14 BER vs SNR for RSV DD of binary CPM signals with $\Delta fT=0.1875$.

CDD and RSV DD combined with MCM have been investigated for quaternary CPM signals with $h=0.25$. SER performances are compared with ideal QPSK SER performance under AWGN in Figure 4-15. Symbol detection via RSV DD with $\mu=1$ improves SER performance compared to the performance of CDD. There is about a 2.5dB symbol SNR difference between SER performance of ideal QPSK and that of quaternary CPM signals via RSV DD.

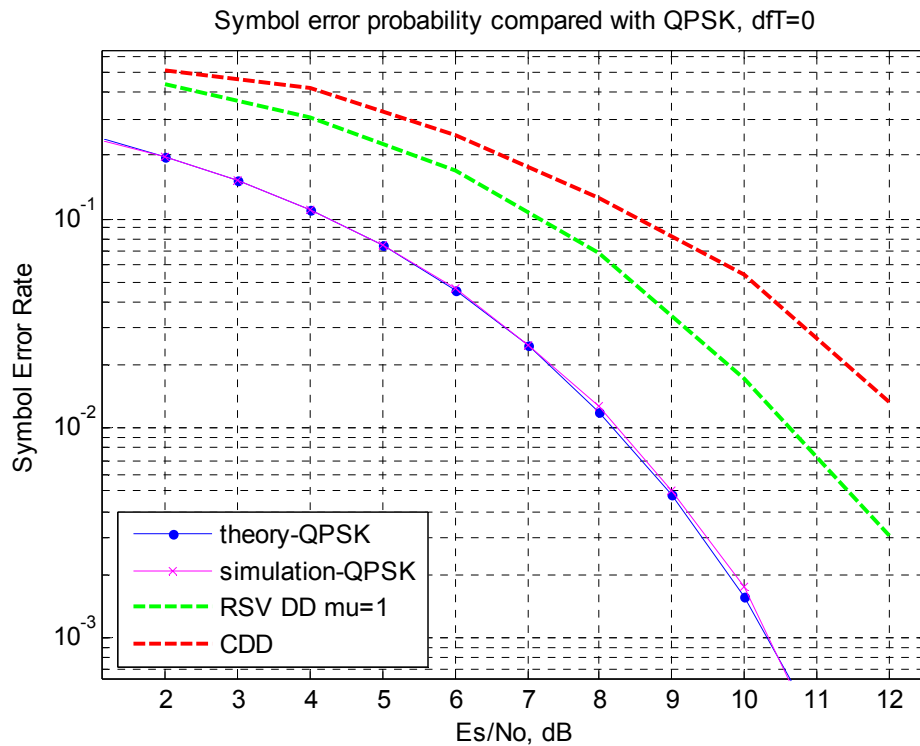


Figure 4-15 SER vs SNR for RSV DD of quaternary CPM signals with $\Delta fT=0$.

BER performance of partial response ($L=2$) binary CPM signals has also been investigated in the absence of CFO. Since MSE of CFO estimates obtained by the modified MCM estimation method is quite high compared to the lower bound for $E_b/N_0 < 12\text{dB}$ (see section 3.5.3.3), it is clear that BER performance obtained by using these CFO estimates will be very poor. Thus, simulations to get BER performances of partial response signals have been done assuming perfect CFO estimation. BER performance of partial response signals has been obtained via RSV DD with $\mu=1$. This performance is compared with ideal BPSK BER performance and BER vs E_b/N_0 plot obtained via RSV DD ($\mu=1$) combined with the modified MCM estimation for full response binary CPM signals. Additionally, we have compared BER performance of RSV DD method ($\mu=0.7$) combined with the modified MCM estimation algorithm for partial response CPM signals (symbol block length is 128). All of these comparisons can be seen in Figure 4-16. The BER curve for perfect frequency compensation degrades about 0.5 dB compared to the BER curve of full response binary CPM signal. RSV DD ($\mu=0.7$) combined

with the modified MCM for partial response binary CPM signal has about 0.4 dB improved BER performance with respect to the RSV DD with perfect frequency synchronization.

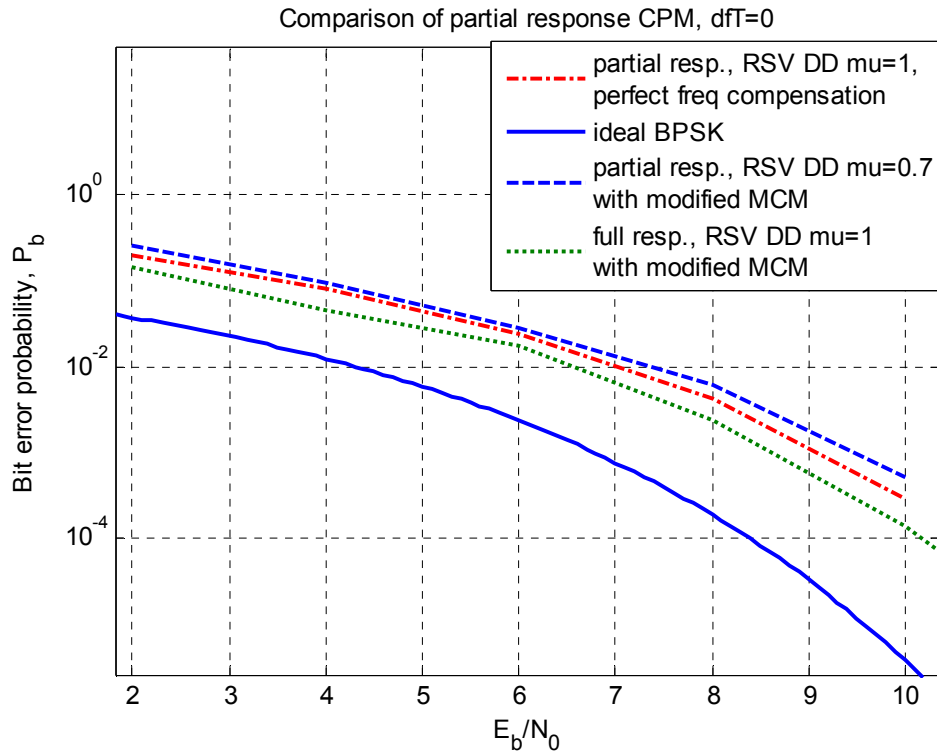


Figure 4-16 BER vs SNR for RSV DD of partial response CPM signals with $\Delta fT=0$.

CHAPTER 5

CONCLUSION AND FUTURE WORKS

In this thesis, a feedforward noncoherent differential CPM demodulation combined with joint estimation of CFO and symbol timing has been developed. A reduced state Viterbi differential detection algorithm is used in order to detect symbols. The joint CFO and symbol timing estimation has been carried out without using training sequences.

Firstly, most of the frequency offset estimation techniques, and joint CFO and symbol timing estimation methods found in the literature have been surveyed, then the selected estimation techniques [12] [13] have been examined for CPM signals combining with symbol-by-symbol conventional differential detection. Among these estimation methods, the MCM algorithm in [12] has been modified for raised cosine frequency pulsed signals. It has been shown that this modification improves BER performance 0.8dB. The MCM algorithm in [12] has also been improved using multiple symbol phase differences. In this way, frequency offsets up to 25% with respect to the data rate can be compensated for binary signals. Simulations show that standard deviation of CFO errors is halved while doubling the number of symbols for phase difference. It is also shown that MSE of symbol timing errors can approach to the lower bound with 2dB of SNR difference.

Moreover, Mengali & Morelli's estimation technique [13], which is applicable to the entire class of MSK-type signals has been implemented. Both algorithms described in [12] [13] have been extended to operate for quaternary and octal signaling with modulation indices $h=0.25$ and $h=0.125$ respectively. Frequency offsets up to 12.5% with respect to the symbol rate can be managed for

quaternary signals, while frequency offsets up to 6.25% can be managed for octal signals. MSE of estimates approach to the lower bound for quaternary signals above $E_b/N_0=15\text{dB}$, and for octal signals above $E_b/N_0=20\text{dB}$. When phase differences between more symbols are used in the estimation algorithm, symbol timing errors moves nearer to the lower bound.

The MCM algorithm [12] and Mengali & Morelli's estimation technique [13] have been modified for partial response signaling too. By these modified algorithms for partial response signals, we can compensate for CFO up to 12.5% of the symbol rate. For 2RC pulsed binary CPM signal, satisfactory standard deviation of CFO errors can be obtained above $E_b/N_0=15\text{dB}$. MSE of symbol timing can get closer to the lower bound as D increases when D-symbol phase differences are used in the modified Mengali & Morelli's estimation algorithm.

In general, instead of symbol-by-symbol conventional differential detection, using optimum Viterbi detector allows to approach the performance of ideal coherent detection. Hence, Viterbi symbol detection algorithms with reduced complexity found in the literature have been surveyed. Among these algorithms, Reduced-state Viterbi differential detection algorithm using a recursively estimated phase reference, which was proposed by Adachi in [11] for M-ary DPSK signals, is selected for examination. In Adachi's detection algorithm, we can adjust the sensitivity to the quality of the CFO estimates by changing the forgetting factor μ .

The examined demodulator has been composed of Reduced state Viterbi differential symbol detection algorithm and one of the joint CFO and symbol timing estimation methods (the modified M&M or the modified MCM). BER (or SER for quaternary and octal signals) performances of the demodulator have been examined under AWGN channel.

Finally, the BER performances of these demodulators are enhanced by reduced state Viterbi differential detection. The improvement between the E_b/N_0 required to obtain a BER of 10^{-3} with CDD and RSV DD is about 1 dB for full response binary MSK-type signals in AWGN channel. There is about a 2dB symbol SNR

improvement to obtain a SER of 10^{-2} with RSV DD with respect to CDD for quaternary CPM signals in AWGN channel.

As a future work, different channel models can be employed in order to see the performance of the demodulator in channels different from AWGN. Additionally, the estimation algorithms can be modified using training sequences. Thus, we may improve the performance in the applications when training sequences can be used.

REFERENCES

1. **Karl, Holger.** *An overview of energy-efficiency techniques for mobile communication.* Berlin : Telecommunication Networks Group, Technical University Berlin, 2003. TKN-03-017.
2. **Anderson, John B., Aulin, Tor and Sundberg, Carl-Erik.** *Digital Phase Modulation.* New York and London : Plenum Press, 1986. ISBN 0-306-42195-X.
3. *Differential detection of MSK with nonredundant error correction.* **Masamura, T., et al.** 6, s.l. : IEEE Trans. Commun., June 1979, Vol. 27.
4. **Proakis, John G.** *Digital Communications.* Singapore : McGraw-Hill Higher Education, 2001. ISBN 0-07-232111-3.
5. *Reduced state sequence detection of partial response continuous phase modulation.* **Svensson, A.** s.l. : IEE Proceedings-I, 1991, Vol. 138.
6. *Reduced complexity detection of bandwidth efficient partial response CPM.* **Svensson, T. and Svensson, A.** s.l. : Vehicular Technology Conference, 1999 IEEE 49th, 1999.
7. *Reduced state sequence detection of full response continuous phase modulation .* **Svensson, A.** 10, s.l. : IEEE Electronic Letters, May 1990, Vol. 26.
8. *Optimum and suboptimum receivers for M-ary CPM signals based upon the Laurent representation.* **Figuera, M. and Krogmeier, J.V.** s.l. : Vehicular Technology Conference, 2002. Proceedings. VTC 2002-Fall. 2002 IEEE 56th, 2002. Vol. 4.
9. *Reduced-complexity detection and phase synchronization of CPM signals .* **Colavolpe, G. and Raheli, R.** 9, s.l. : IEEE Transactions on Communications, 1997, Vol. 45.
10. *Reduced-state sequence estimation with set partitioning and decision feedback.* **Eyuboglu, M.V. and Qureshi, S.U.H.** 1, s.l. : IEEE Transactions on Communications, 1988, Vol. 36.
11. *Reduced-state Viterbi differential detection using a recursively estimated phase reference for M-ary DPSK .* **Adachi, F.** 4, s.l. : IEE Proceedings-Communications, 1995, Vol. 142.
12. *A fully digital feedforward MSK demodulator with joint frequency offset and symbol timing estimation for burst mode mobile radio .* **Mehlan, R., Chen, Yong-**

- En and Meyr, H.** 4, s.l. : IEEE Transactions on Vehicular Technology, 1993, Vol. 42.
13. *Joint frequency and timing recovery for MSK-type modulation* . **Morelli, M. and Mengali, U.** 6, s.l. : IEEE Transactions on Communications, 1999, Vol. 47.
14. **Xiong, Fuqin.** *Digital modulation techniques*. s.l. : ARTECH HOUSE, INC., 2000. ISBN 0-89006-970-0.
15. *Feed-forward Carrier Frequency and Timing Synchronization for MSK Modulation*. **Yao, Yao and Ng, Tung-Sang.** Singapore : International Conference on Information, Communications and Signal Processing - Pacific Rim Conference on Multimedia, 2003.
16. *A fully digital noncoherent and coherent GMSK receiver architecture with joint symbol timing error and frequency offset estimation*. **Y.-L.Huang and K.-D.Fan.** 3, s.l. : IEEE Transactions on Vehicular Technology, 2000, Vol. 49.
17. *A low IF GMSK modem architecture with joint symbol timing recovery and frequency offset compensation* . **Huang, Y.-L. and Huang, C.-C.** s.l. : IEEE International Symposium on Personal, Indoor and Mobile Radio Communications, 1996.
18. *Single tone parameter estimation from discrete-time observations*. **Rife, D.C. and Boorstyn, R.R.** s.l. : IEEE Transactions on Information Theory, 1974, Vol. 20.
19. *Feedforward carrier frequency estimation with MSK-type signals*. **Morelli, M. and Mengali, U.** 8, s.l. : IEEE Communication Letters, 1998, Vol. 2.
20. *A fast and accurate single frequency estimator*. **Kay, S.** 12, s.l. : IEEE Transactions on Acoustics, Speech and Signal Processing, 1989, Vol. 37.
21. *Estimating the frequency of a noisy sinusoid by linear regression*. **Tretter, S.** 6, s.l. : IEEE Transactions on Information Theory, 1985, Vol. 31.
22. *Feedforward frequency estimation for PSK: A tutorial review*. **Morelli, M. and Mengali, U.** 2, s.l. : European Transactions on Telecommunications, 1998, Vol. 9.
23. *Digital carrier frequency estimation for multilevel CPM signals* . **D'Andrea, A.N., Ginesi, A. and Mengali, U.** Seattle : IEEE International Conference on Communications, 1995.
24. *An illustration of the MAP estimation method for deriving closed-loop phase tracking topologies: the MSK signal structure*. **Booth, R.** 8, s.l. : IEEE Transactions on Communications, 1980, Vol. 28.

25. *Continuous Phase Modulation - Part I: Full Response Signaling*. **Aulin, T. and Sundberg, C.-E. W.** s.l. : IEEE Transactions on Communications, 1981, Vol. 29.
26. *Continuous Phase Modulation - Part II: Partial Response Signaling*. **Aulin, T., Rydbeck, N. and Sundberg, C.-E. W.** s.l. : IEEE Transactions on Communications, 1981, Vol. 29.
27. **Bateman, A.** *Digital Communications: Design for the real world*. New York : Addison-Wesley Longman Limited, 1999. ISBN 0-201-34301-0.
28. **Trees, H. L. Van.** *Detection, Estimation, and Modulation Theory*. New York : John Wiley & Sons., 1968.
29. *The modified Cramer-Rao bound and its application to synchronization problems*. **D'Andrea, A. N., Mengali, U. and Reggiannini, R.** s.l. : IEEE Transactions on Communications, 1994, Vol. 42.
30. **Mengali, U. and D'Andrea, A. N.** *Synchronization Techniques for Digital Receivers*. New York : Plenum Press, 1997.
31. **Meyr, H., Moeneclaey, M. and Fechtel, S. A.** *Digital Communication Receivers: Synchronization, Channel Estimation, and Signal Processing*. New York : John Wiley & Sons Inc., 1998.
32. *Jitter optimization based on phase-locked loop design parameters*. **Mansuri, M. and Yang, C.-K. K.** s.l. : IEEE JOURNAL OF SOLID-STATE CIRCUITS, 2002, Vol. 37.
33. *Hangup in phase lock loops*. **Gardner, F.M.** s.l. : IEEE Transactions on Communications, 1977, Vol. 25.
34. *Noncoherent sequence detection of continuous phase modulations* . **Colavolpe, G. and Raheli, R.** 9, s.l. : IEEE Transactions on Communications, 1999, Vol. 47.
35. *Multiple-symbol differential detection of MPSK*. **Divsalar, D. and Simon, M.K.** s.l. : IEEE Transactions on Communications, 1990, Vol. 38.
36. *Noncoherent detection of continuous phase modulation using overlapped observations*. **Raphaeli, D. and Divsalar, D.** San Francisco : IEEE Communication Theory Mini-Conference, GLOBECOM'94, 1994.
37. *Maximum-likelihood block detection of noncoherent continuous phase modulation*. **Simon, M.K. and D.Divsalar.** s.l. : IEEE Transactions on Communications, 1993, Vol. 41.

38. *Multiple-symbols differential detection of GMSK.* **Abrardo, A., Benelli, G. and Cau, G.** s.l. : IEEE Electronics Letters, 1993, Vol. 29.
39. *Noncoherent reduced state differential sequence detection of continuous phase modulation.* **Sun, J., et al.** s.l. : IEEE International Symposium on PIMRC, 2004. Vol. 2 .
40. *Reduced-State detection for continuous phase modulation (CPM) Signals.* **Nan, Z. and Ping, Y.** s.l. : International Conference on Intelligent Information Hiding and Multimedia Signal Processing, 2008.
41. *Decomposition of M-ary CPM signals into PAM waveforms.* **Mengali, U. and Morelli, M.** s.l. : IEEE Transactions on Information Theory, 1995, Vol. 41.